Design, Fabrication, and Characterization of Novel Multi-Channel Photodetectors Using Post-Growth Approaches in the Near Infrared and Short-Wavelength Infrared Regimes

---

Dissertation

Presented to

the faculty of the School of Engineering and Applied Science

University of Virginia

In Partial Fulfillment

of the requirements for the Degree

Doctor of Philosophy

Electrical Engineering

by

Jinrong Yuan

August 2014

APPROVAL SHEET

The dissertation

is submitted in partial fulfillment of the requirements

for the degree of

Doctor of Philosophy in Electrical Engineering

_____

Jinrong Yuan

The dissertation has been read and approved by the examining Committee:

_____

Dr. Archie L. Holmes Jr. (Advisor)

_____

Dr. Arthur W. Lichtenberger (Committee chair)

_____

Dr. Joe C. Campbell

_____

Dr. Lloyd R. Harriott

_____

Dr. James M. Howe

Accepted for the School of Engineering and Applied Science:

_____

Dr. James H. Aylor, Dean,
School of Engineering and Applied Science

August 2014

Abstract

Advances in light related technology have greatly changed the way we visualize the world and share information. In the past a few decades, a significant amount of effort in research has been devoted into utilization of light in different spectrum regimes to benefit human activities. As a result of these efforts, it is possible to gather information from objects that cannot be seen directly by human eyes by analyzing the light reflected/emitted from these objects, and provide diagnosis of the environment/surroundings. This function enables us to detect threats or harmful substances more efficiently in various military, civil, and medical sensing applications.

The technology used in many of the sensing applications is spectroscopy. When light interacts with matter, the interaction can change the electrons in atoms and molecules and hence exchange energy between them. By collecting and analyzing the emission spectrum as a function of wavelength (λ), some intrinsic properties of the matter can be revealed and therefore used for further studies. Particularly, some of the spectrum regimes of great interest are within the infrared regime (700 nm – 1mm). Wavelengths in this regime are harmless to human tissues, and they include characteristics of a broad range of activities such as thermal emissions, gas molecule rotations/vibrations, chemical absorptions, and free-space communication. By detecting the proper wavelengths of the objects' unique features, system dynamics can be determined and used for identifying substances located beyond human vision or presence. In some special applications, detecting different wavelengths at the same time is preferred for reducing the system parameters on a real-time basis.

With this motivation, a novel method for filtering light of interest in the near-infrared (NIR, 0.75 – 1.4 μm) and short wavelength infrared (SWIR, 1.4 – 3 μm) wavelength regimes for simultaneous multiple light detection is studied and presented. I use the InP-based photodetectors with a type-II multiple quantum well active region as my light absorption component, and integrate it with Fabry-Perot optical filters to achieve the purpose of simultaneously detecting wavelengths of interest in the NIR/SWIR regimes. The InP-based photodetectors has an active region comprises InGaAs/GaAsSb type-II multiple quantum wells lattice-matched to InP, with high photoresponse in the NIR regime and reasonable photoresponse from 1.8 μm to 2.5 μm, so it has the capability of providing distinguishable photoresponse after light filtering from 1.1-1.8 μm. The filters used are based on Fabry-Perot resonant cavities, and the materials to form the cavities are SiO_2 (silicon dioxide) and a-Si (amorphous silicon). By integrating the two key parts, only the spectrum of interest can be picked out from the incident light that contains a broad range of wavelengths. The filtered portion of light transmits through the filter structure, and eventually gets absorbed and converted into electrical current for detection. By using multiple filters each integrated with a photodetector, an arbitrary number of different wavelengths can be detected at the same time with each of them capable of selecting a single wavelength. This dissertation has proved that by using inexpensive amorphous materials in the post-growth filters, the integrated devices are capable of detecting multiple wavelengths simultaneously in the NIR/SWIR regimes (below 1.8 μm) with competitive performances: sharp photoresponses (Full Width at Half Maximum < 50 nm), high quantum efficiencies (up to 37.4%), and close-to-zero low sideband interference. Additionally, the multiple wavelengths of detection can be tuned flexibly without adding difficulty to the existing fabrication process. These promising results offer the opportunity of more precise sensing/detection at a lower cost and higher flexibility. Compared to

prior art by Emadi, *etc.*, who proposed the theoretical basis of the Fabry-Perot filters' design and fabrication for imaging applications, my study has realized not only the physical implementation of the filters and extended the application to the NIR regime, but also successfully integrated the filters with high-performance photodetectors to realize simultaneous multispectral wavelength detection.

Contents

Table of Figures

List of Tables

Chapter 1 Introduction

Multi-channel photo-detection in the infrared regime has been extensively used in applications such as multi-spectral imaging and hyper-spectral imaging [1]–[5], which have been serving sensing systems such as night vision, thermal surveillance, missile tracking, mineral detection, food quality monitoring, chemical imaging, and astronomical imaging [6]–[14]. In these applications, the detectors can sense the "finger-print" absorption characteristics of the object, making it possible to determine its temperature and composition on a real-time basis so as to collect information of the system dynamics [15], [16]. For example, a multi-channel photodetector array that detects the thermal emission of the human body can be used in a night vision/surveillance camera, which depicts the activities of target(s) aside from the surroundings. A similar thermal imaging principle is used for missile tracking. The thermal emission regime of the target, for instance, the plume at 550K, differs from the surrounding temperature at 240K [17], [18], and therefore using a sensor system capable of detecting both regimes can provide information on the target's surface temperature(s) and materials, and thus locate its coordinates [19]. In food quality monitoring, since the object's absorption characteristics vary with its compound compositions, it's convenient to use this infrared technology to distinguish different food types or degraded parts [10], [20]. In chemical forensics and gas monitoring, a multi-spectral detector can provide clues on the existing gases of interest in the testing environment, based on the rotational-vibrational frequencies of the objects [21]–[23]. Therefore, it is a convenient way to identify the surrounding ambient and harmful gases.
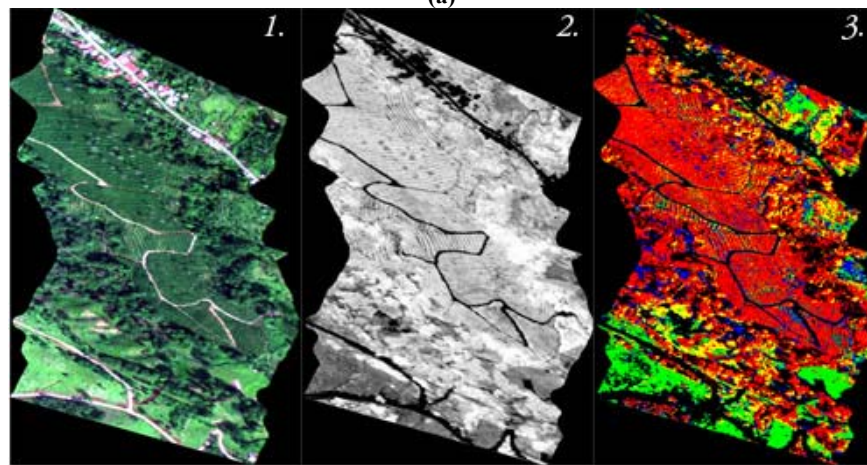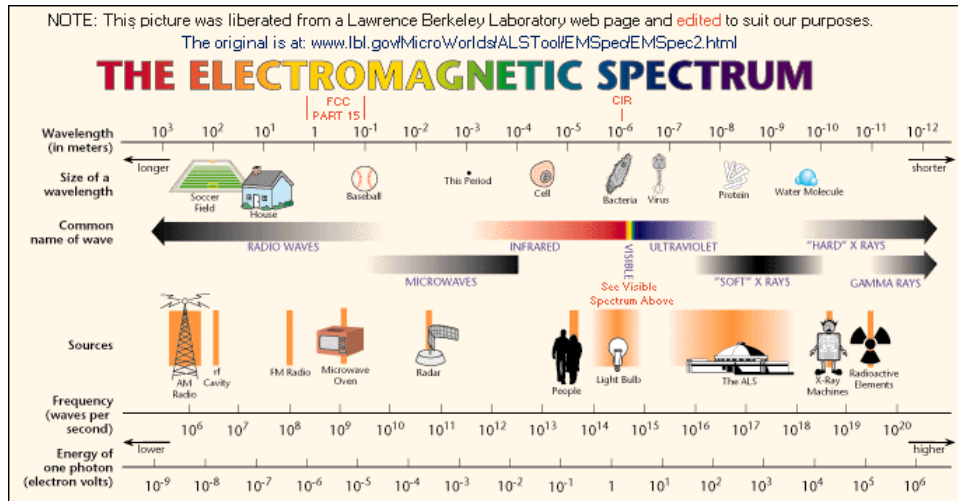
Fig. 1. 1 (a) The electromagnetic spectrum (b) An example of images taken at three different wavelengths and synthesized in hyperspectral imaging for identifying plant species from the air in Costa Rica. The pictures are taken from Reference [24] and [25], respectively.

Particularly, for imaging applications, combining multiple input images into one output image requires the technology of image fusion/registration [26], [27], in which the data processing allows the integration of different information sources from multiple sensors. For minimum distortion of the fused images, for synthetic images it is preferred to have high spectral and spatial resolutions, meaning the images are either taken from the same exact coordinate, or at least from pixels as close as possible. Therefore, having the detectors on the same chip offers the

opportunity of less synthesis distortion because the devices can be designed to be only microns from one another. Meanwhile, monolithic integration is desired for readout circuit and further compatibility with more complex in-plane designs [28].

Moreover, for applications such as remote sensing, having the ability to detect multiple wavelengths can be critical for determining the composition accuracy of the target. For example, a photodetector array capable of detecting multiple signature wavelengths of an object (e.g. a broad area on earth) can be integrated on an instrument (e.g. a satellite) far away from the object, and thus the photodetector array can be used for imaging/sensing the broad area from the distance at different wavelengths to better identify the physical/chemical properties of the area and provide more accurate information about the target than the detection of at a single wavelength[29], [30]. Furthermore, the long distance makes the differences in the light incident angle so small that the error caused by the slight shift in the object's relative coordinate can be negligible. Therefore, this greatly benefits the post-calculation for image synthesis and analysis.

In currently existing imaging technologies, there are mainly two popular approaches to detect multiple wavelengths by using photodetectors. One approach is to integrate optical lens with a photodetector array [1], [31], to filter different colors/wavelengths; the other approach is to grow multiple absorption layer on one substrate, while each absorption layer is capable of absorbing light of a distinct wavelength, to detect distinct wavelengths by biasing different absorption layers [32][33]. The first approach has been implemented in industrial/military use for many of the existing multispectral imaging cameras for wavelength detection from UV to NIR regimes, and research has shown that the second approach can detect wavelengths from MWIR to LWIR regimes at low temperatures. However, the first approach usually takes more volume than an ordinary chip due to lens integration, and therefore might not be suitable for some

applications that require a more compact detector package; the second approach can only sense object(s) in a sequential, which makes it not suitable for imaging/sensing object(s) moving at a high relative speed due to higher error in post calculation. Meanwhile, the second approach is highly demanding on the material properties of the absorption layers such as lattice constant for material growth requirement, and this limits the types of materials that can be used as the absorption layers, and as a result, the wavelengths that can be detected by using this approach is limited.

To improve the limitations mentioned above, specifically urges of improvement in volume, wavelength detection flexibility, and calculation error in currently existing multispectral technologies, the goal of this study is to develop post-growth wavelength filters integrated with photodetectors on the same chip for simultaneous detection of multiple wavelengths. The wavelengths for detection are in this study are chosen to be in the NIR (Near Infrared, 0.75 – 1.4 μm)/SWIR (Short-Wavelength Infrared, 1.4 – 3 μm) regimes for the important practical values of these regimes [34]. The filters are chosen to be Fabry-Perot optical filters, integrated with InP-based photodetectors to detect wavelengths of interest simultaneously without taking extra space on the chip. To cover the wavelength regimes, InGaAs/GaAsSb type-II multiple quantum well photodetectors are selected as the light absorption region for their broad high response below 1.8 μm [13], [14]. Simulations using InP substrate and InP-based InGaAs/GaAsSb type-II multiple quantum well photodetectors integrated with two potential filtering methods are combined to study the transmission and absorption characteristics from 1.1 μm to 2.5 μm. Advantages and disadvantages of each method for NIR and SWIR detection will then be compared and the Fabry-Perot filter will be selected for implementation. Table 1.1 illustrates the advantages and disadvantages of the methods discussed above.

Table 1.1 A comparison between the traditional multispectral sensing methods and the proposed novel multispectral sensing method

Imaging Method	Advantages	Disadvantages
Photodetector array with compact lens	• Simultaneous wavelength detection • Flexibility to change wavelength of detection after material growth	• Bulky
Photodetectors with multiple absorption regions	• No extra space needed the chip • Capable of wavelength detection in the MWIR and LWIR regimes	• Change of wavelengths of detection is limited after material growth • Limited to sequential wavelength detection
Photodetectors with Fabry-Perot integrated filters	• Simultaneous detection • Flexibility in change wavelength of detection after material growth • No extra space needed on the chip	• Lengthy filter deposition step • Wavelength tuning susceptible to material deposition and fabrication

This demonstration will mostly focus on the NIR/SWIR regime from 1.1 μm to 1.8 μm to take advantage of the high quantum efficiency in this regime and relatively simpler fabrication and characterization methods. Four filtered wavelengths at 1.35, 1.45, 1.5, and 1.69 μm will be realized by integrating the photodetectors with the Fabry-Perot filters to study the transmission, absorption, and FWHM (Full Width Half Maxim). However, this dissertation will be extended to explore the potential of wavelength detection beyond 1.8 μm using the same filtering approach and photodetector, based on the theoretical prediction. The wavelengths chosen for future study are 2, 2.1, 2.2 and 2.31 μm, for a more comprehensive understanding of the challenges in fabrication and characterization at longer wavelengths using the Fabry-Perot filtering method. Limitations of current fabrication and characterization methods encountered in the initial work are pointed out and analyzed. Last but not least, improvements and alternative approaches for longer wavelength detection will be proposed.
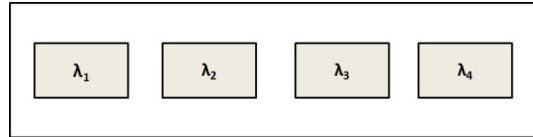
Fig. 1. 2 Schematic of a four-color photodetector array

My dissertation is organized as follows: Chapter 2 starts with an overview of the existing wavelength tuning technologies and the associated key components, e.g. the filtering mechanisms and the light absorption in these approaches. I will then discuss the device physics of the two methods we chose to study: Fabry-Perot filters and guided-mode resonance filters. The materials that comprise the integrated devices will be introduced. Chapter 3 presents the typical fabrication and characterization process of the InP-based MQW photodetectors used for filter implementation and the basic properties e.g. dark current-voltage characteristics and external quantum efficiency characteristics of the devices, proving good potential in NIR and SWIR wavelength detection. Chapter 4 compares the RSoft simulation results of wavelength selection using Fabry-Perot filters and guided-mode resonance filters in the NIR and SWIR regimes, and a thorough sensitivity analysis is provided to investigate the impact of parameter variations on the wavelength detection precision, variables including deposition/fabrication variation, temperature change, and light incident angle variation. Later in this chapter, the comparison between the simulation results of the FP filter and the guided-mode resonance filter suggests better filtering/detecting performance can be obtained by using the FP filter for the wavelength regime given, especially between 1.1 and 1.8 μm in order to achieve high quantum efficiency. In Chapter 5, the sputter deposition condition for the SiO_2/a-Si FP filter will be characterized and the fabrication process will be described. Also, the fabrication and characterization of the integrated multispectral photodetectors for wavelength detection below

1.8 μm and correlation between the parameter variation and the detection precision by analyzing the layer thicknesses, I-Vs, external quantum efficiencies, and FWHMs. In Chapter 6, a conclusion of the present work is made and the results are benchmarked with peers. Multispectral photodetectors for detection of wavelengths longer than 1.8 μm are then discussed in terms of I-V measurement, SEM imaging and photoresponse measurement using Fourier Transform Infrared Spectroscopy (FTIR), and the results will be used to understand the challenges and limitations in the fabrication and characterization processes for longer wavelength detection using the Fabry-Perot filters. This will provide guidelines for improvements. In the last part of this chapter, potential solutions for the problems in the current design, fabrication and characterization will be proposed for better simultaneous wavelength detection options in different wavelength regimes.

Chapter 2 Device Structures and Physics of Wavelength Selection Methods and Materials

2.1 An Overview

In this chapter, I will briefly review and compare the advantages and disadvantages of the existing wavelength tuning methods, and select the Fabry-Perot filter and the guided-mode resonance filter for in-depth analysis based on their post-growth tuning flexibility over many other filtering methods. The materials requirements, filter structure, and working mechanism of each filter will be demonstrated in detail. Later in this chapter, the absorption characteristics of the broadband InP-based photodetectors for this study will be presented.

2.1.1 Filters

As commonly known, the function of a filter is to transmit a range of wavelengths of light, so as to effectively select the spectrum of interest from the background[35], [36]. In many sensing applications, in order to detect the absorption spectrum of the target, the detectors (sensors) need to signal accurate positives on the wavelengths that reflect the properties of that target, and a proper filtering mechanism is essential for the successive light absorption and signal processing. To maximize the detection precision while eliminating the side-band noise, several mechanisms of wavelength selection have been studied by. The commonly used filtering mechanisms generally fall into two categories: pre-growth and post-growth.

Pre-growth Wavelength Detection. Wavelength detection pre-determined in material growth has been studied by many researchers. For a narrow spectrum, a resonant cavity with a single absorption region has been used for precise wavelength selection [37]–[39]. In such

structures, the active layer aligns within the cavity for the absorption of this particular spectrum region. The cavity and the highly reflective mirrors serve as the filter that only allows one standing wave to form, and the selected spectrum is determined by the wavelength of the standing wave (length of the cavity before material growth). The tuning range of this type of photodetector is very limited [40]. For multiple wavelength selection, multiple absorption regions [32], [33], [41]–[43] and inter-subband transitions [44], [45] are two important techniques. By applying voltages on the active regions separately (for multi-absorption-region structures), or tuning the operation bias (for quantum structures with inter-subbands), the corresponding optical transition can be excited and different spectral regions can be detected in a sequential manner. These structures are demanding on the material growth, which also limits the wavelength tuning range. Additionally, simultaneous detection cannot be obtained in the sequential structures discussed above. Cryogenic operations is always needed for satisfactory performances for longer wavelengths due to high dark current inherent from the narrow-bandgap transitions [2], [46].

Post-growth Wavelength Detection. Wavelength detection by post-growth methods greatly improves the design flexibility and the ability to sense different frequencies on the same chip. Numerous approaches have been developed and several have been realized. Recess etching of the cavity layer grown on the substrate is an easy approach and a tuning range of less than 50 nm was achieved [47], [48], but required a large number (>20) of DBR pairs lattice-matched to the substrate in order for the resonant cavities to function well. Tuning utilizing the Stark effect was reported by many researchers owing to the convenience of changing the wavelengths of interest after device fabrication, but the range is limited to ~80 nm [38][49]. Thermal tuning is a low-cost method but the reported tuning range is only ~15 nm [50]. Theoretical calculations on

changing the refractive index profile of 1D grating mirrors were reported by applying pressure on the grating, but the tuning range was only ~32 nm [51]. Integration of optical lenses can effectively select the wavelengths with low side-band transmittance but this increases the volume [52]. Conductive material (esp. metal) patches and gratings with and without dielectric layers have been studied as selective reflection/transmission filters thanks to the plasmonic activity when reacting with photons [53], [54]. The experimental results reported have shown promising selectivity spanning from visible to microwave spectrum range. However, e-beam lithography is required for feature patterning, which significantly increases cost and fabrication complexity.

2.1.2   Absorption region

High photo-response in the target spectrum regime is desired for the active layer in order to increase signal-to-noise ratio. Various absorption regions have been developed in the NIR/SWIR regime for different applications. HgCdTe photodetectors are traditionally competitive in civil/military applications thanks to their broad photo-response range (0.7~25 μm) and high quantum efficiency (QE) [55]. However, low yield and high dark current increase the operation cost [19], [56]. On GaSb substrates, bulk InAsSb detectors have photo-response covering the spectral range 1.7-4.2 μm, but need cryogenic operation due to high dark current [57]. More attention in industry and research has shifted to InP-based detectors for their mature fabrication process and high yield [13], [14]. Photodetectors based on InGaAs/InP absorption regions are typically used for wavelength below 1.65 μm due to their high QE and low dark current. Extending the wavelength beyond 1.65 μm requires a different absorption region. On InP substrates, approaches include strain compensated $In_{1-x}Ga_xAs$ (x<0.47) quantum well (QW) photodiodes which have achieved a cutoff wavelength of 2.15 μm [58], or relaxed $In_{1-x}Ga_xAs$

grown on InP photodetectors which has demonstrated an operation wavelength beyond 2 µm [59]–[61].

In the past few years, photodetectors based on InGaAs/GaAsSb type-II quantum wells on InP substrate have shown great potential in SWIR/MWIR detection [13], [39], [62]. In these structures, electrons and holes are confined in adjacent layers, and optical transitions occur over a smaller effective bandgap, which enables longer wavelength operation. In addition, type-I transitions in InGaAs and GaAsSb layers enable NIR response. Our preliminary results have shown photo-response from 0.85 µm to beyond 3.4 µm from our strained compensated InGaAs/GaAsSb type-II photodetectors [13], [14], [56]. More information on the experimental results will be provided later in this chapter.

2.2   Fabry-Perot Filter

Since post-growth wavelength detection methods provide more flexibility in varying the detection frequencies on the same chip, which can be a necessary feature in some applications [4], [63], it is advantageous to develop/optimize post-growth wavelength detection methods that are capable of providing highly distinguishable positives at the wavelengths of interest in order to select/filter spectrum of interest and convert the wavelengths to electrical signal. One of the promising post-growth filtering mechanisms of high transmission and selectivity is a dielectric Fabry-Perot (FP) filter. A Fabry-Perot filter is a resonant cavity that includes a medium sandwiched by two parallel reflecting mirrors. A standing wave forms between the reflectors. The effective distance between the mirrors is called the cavity length. Only cavity lengths that allow wavelengths that are an integer multiple of half the standing wave will give rise to sharp peaks in the transmission spectrum [64]–[66]. By using recess etching on the cavity regions,

Fabry-Perot filters for different wavelengths of interest can be fabricated on the same chip. Arvin Emadi *et al*. have predicted the theoretical transmission of linear variable optical filters by utilizing Fabry-Perot filters with Distributed Bragg Reflectors (DBRs) as high reflectivity mirrors [66]–[68]. Compared to other existing wavelength selection methods, a Fabry-Perot filter provides sharp transmission lines at wavelengths of interest, much broader wavelength tuning range, and most importantly, it imposes no requirement on the detector's epi-layer lattice constants. However, the inevitable thickness deviation introduced by film growth/etch is the main challenge to precise wavelength selection.

(a)	**(b)**	**(c)**
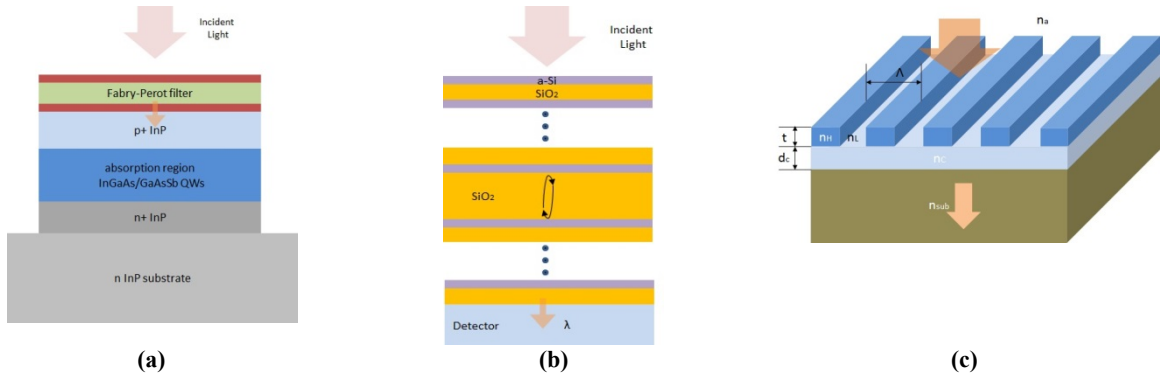
Fig. 2. 1 Schematics of (a) Wavelength selection through a Fabry-Perot filter on a InGaAs/GaAsSb QW PIN photodetector (b) Layer sequence of a SiO$_2$/a-Si FP filter (c) 1D guided-mode resonance gratings on a substrate with grating period (Λ), thickness (t), and refractive indices (n$_H$/n$_L$).

The key components of a Fabry-Perot optical filter and its detailed working mechanisms are discussed below.

2.2.1   Distributed Bragg Reflector

A Distributed Bragg Reflector (DBR) [69] is composed of N pairs of high-n/low-n layers of quarter-wavelength optical thickness: QWOT=$\frac{\lambda_0}{4n}$, in which λ_0 is the reference wavelength at the center of the filter spectrum, n is refractive index of the cavity medium at this reference wavelength [65], [66]. Fig. 2 (a) shows a typical structure of a DBR structure (N is the number of

pairs, $n_1 > n_2$) with normal light incidence, and Fig. 2 (b) is the corresponding simulation results using the stated structure but with increasing N values, $\Delta\lambda$ is the width of the stop-band centered at λ_0.

(a)   (b)
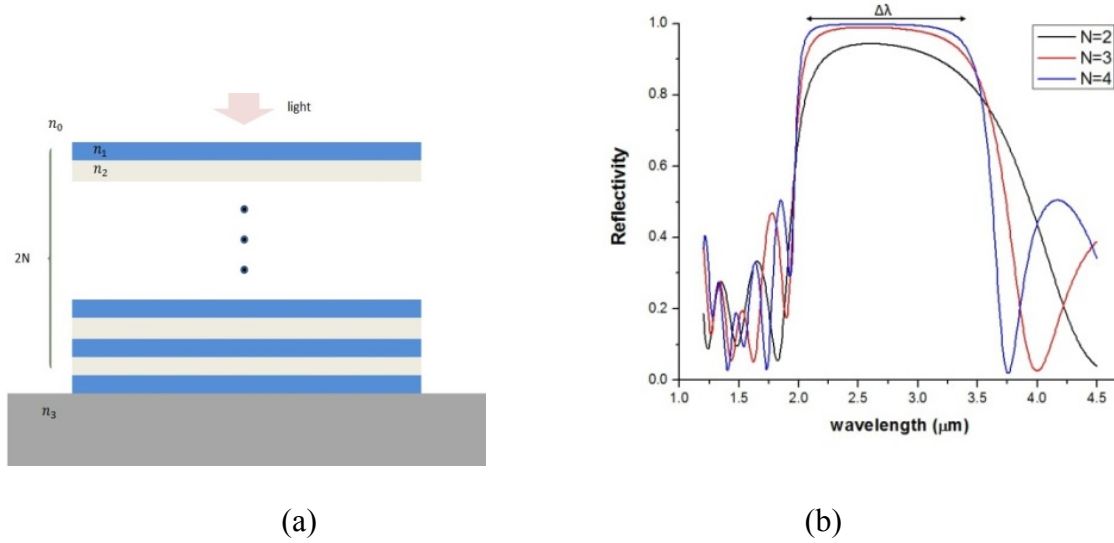
Fig. 2. 2 (a) Structure of a typical DBR stack (b) Simulated reflectivities of DBRs center at λ_0=2.5 μm (n_1(a-Si)=3.278, n_2(SiO$_2$)=1.430 on InP substrate) with different N values [65]

A high-n layer is usually added between the substrate and the last low-n layer to improve reflectivity. The typical DBR structural profile is n_0/ $(n_1n_2)^N n_1$ /substrate, in which n_0 is the refractive index of the ambient medium, and n_1/n_2 is the refractive index of high-n/low-n layer ($\Delta n = n_1 - n_2$). $\Delta\lambda$ is the bandwidth of the stopband. The reflectivity at a particular wavelength and $\Delta\lambda$ are calculated using the following equations [69]:

$$r = \frac{n_0 n_2^{2N} - n_3 n_1^{2N}}{n_0 n_2^{2N} + n_3 n_1^{2N}} \tag{2.2.1}$$

$$\frac{\Delta\lambda}{\lambda_0} = \frac{4}{\pi} arcsin(\frac{n_2 - n_1}{n_2 + n_1}) \tag{2.2.2}$$

As can be seen from the equations above, the reflectivity of the stopband of DBRs can be increased by adding more pairs of dielectrics (larger N) or choosing dielectrics with larger Δn.

2.2.2 Fabry-Perot resonant cavity

A Fabry-Perot resonator [64], [65] is a resonant cavity made of a transparent medium sandwiched by two parallel highly reflecting mirrors. A standing wave will form by the constructive and destructive interference of light waves between the two reflectors when they are aligned perfectly parallel. Any wavelengths not equal to an integer multiple of half the wavelength of the standing wave will interfere destructively. Whether the multiply reflected beams are in phase or not depends on the wavelength (λ) of the light (in vacuum), the incident angle of the light (θ), the distance between the reflectors (l), and the refractive index of the material between the reflecting surfaces (n). An ideal Fabry-Perot is assumed in this design.
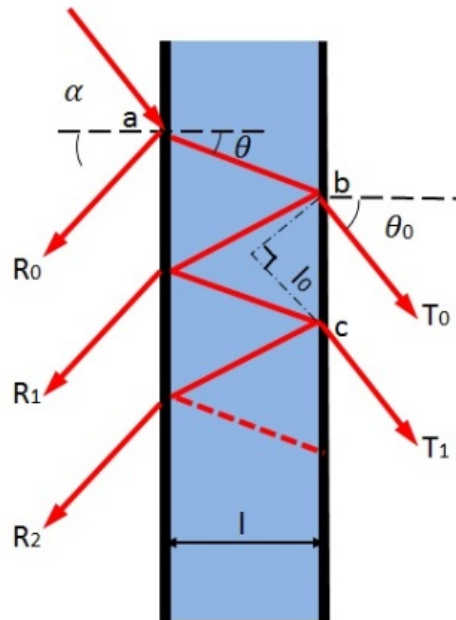
Fig. 2. 3 A Fabry-Perot filter/interferometer [64]

As illustrated in Fig. 2.3, T_0 is transmitted through the cavity, and T_1 is reflected twice before transmission. At each reflection, the amplitude is reduced by $\sqrt{R}$ and the phase is shifted

14

by π, which at each transmission through an interface the amplitude is reduced by $\sqrt{T}$. Assuming no absorption, conservation of energy requires $T + R = 1$. In the derivation below [64], [66], n is the refractive index of the medium between the mirrors, and n_0 is the reflective index of the outside medium. The incident amplitude at point a is assumed to be 1, and phasors are used to represent the amplitudes of the radiation. The transmitted amplitude at point b will then be

$$t_0 = Te^{ikl/\cos\theta} \tag{2.2.3}$$

where $k = 2\pi n/\lambda$ is the wavenumber between the mirrors. At point c the transmitted amplitude will be

$$TRe^{2\pi i + 3ikl/\cos\theta} \tag{2.2.4}$$

The total amplitude of both beams will be the sum of the amplitudes of the two beams measured along a line perpendicular to the direction of the beam. The amplitude at point b can therefore be added to an amplitude t_1, which is the magnitude of the amplitude at point c, but retarded in phase by an amount $k_0 l_0$, where $k_0 = 2\pi n_0/\lambda$ is the wavenumber outside of the cavity. Thus

$$t_1 = RTe^{2\pi i + \frac{3ikl}{\cos\theta} - ik_0 l_0} \tag{2.2.5}$$

where l_0 is

$$l_0 = 2lt an\theta \sin\theta_0 \tag{2.2.6}$$

Neglecting the 2π phase change due to the two reflections, the phase difference between the two beams (t_0 verses t_1) is

$$\delta = \frac{2kl}{\cos\theta} - k_0 l_0 \tag{2.2.7}$$

15

The relationship between θ and θ_0 is given by Snell's law:

$$nsin\theta = n_0 sin\theta_0 \qquad (2.2.8)$$

The phase difference may be written as

$$\delta = 2klcos\theta \qquad (2.2.9)$$

To include a constant multiplicative phase factor, the amplitude of the mth transmitted beam can be written as

$$t_m = TR^m e^{im\delta} \qquad (2.2.10)$$

The total transmitted amplitude is the sum of all individual beam amplitudes

$$t = \sum_{m=0}^{\infty} t_m = T \sum_{m=0}^{\infty} R^m e^{im\delta} \qquad (2.2.11)$$

The series is a geometric series of which the sum can be expressed analytically. The amplitude can be rewritten as

$$t = \frac{T}{1 - Re^{i\delta}} \qquad (2.2.12)$$

The intensity of the beam will be just t times its complex conjugate. Since the incident beam was assumed to have an intensity of 1, this will also give the transmission function

$$T_e = tt^* = \frac{T^2}{1 + R^2 - 2Rcos\delta} = \frac{1}{1 + Fsin^2(\frac{\delta}{2})} \qquad (2.2.13)$$

where $F = \frac{4R}{(1-R)^2}$ is the coefficient of finesse.
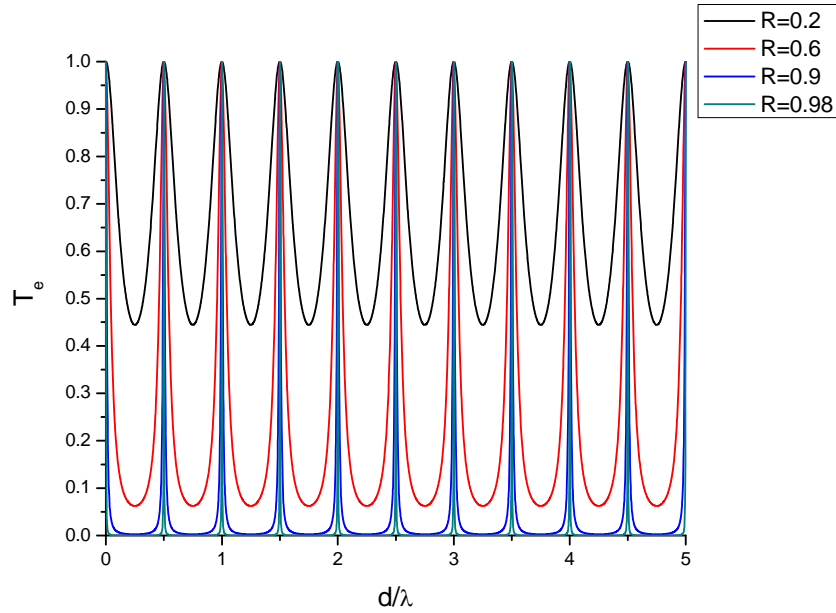
Fig. 2. 4 Transmission of FP with varying mirror reflectivity. All parameters are dimensionless [66]**.**

The relationship of the operating order N and the cavity thickness *l* can be expressed as N=2n*l* /λ. As can be seen in Fig. 2.4, higher resonance orders result in a smaller FWHM, but a reduced operation bandwidth, which is also known as the wavelength separation between adjacent peaks. The calculation of Free Spectral Range (FSR) originates from:

$$\frac{2\pi dcos\theta}{\lambda_1} - \frac{2\pi dcos\theta}{\lambda_2} = \pi \rightarrow \frac{\lambda_2 - \lambda_1}{\lambda_2\lambda_1}$$

(2.2.14)

and is given by:

$$FSR=\lambda_2 - \lambda_1 = \frac{\lambda_2^2}{\lambda_2+2ndcos\theta}$$

(2.2.15)

17
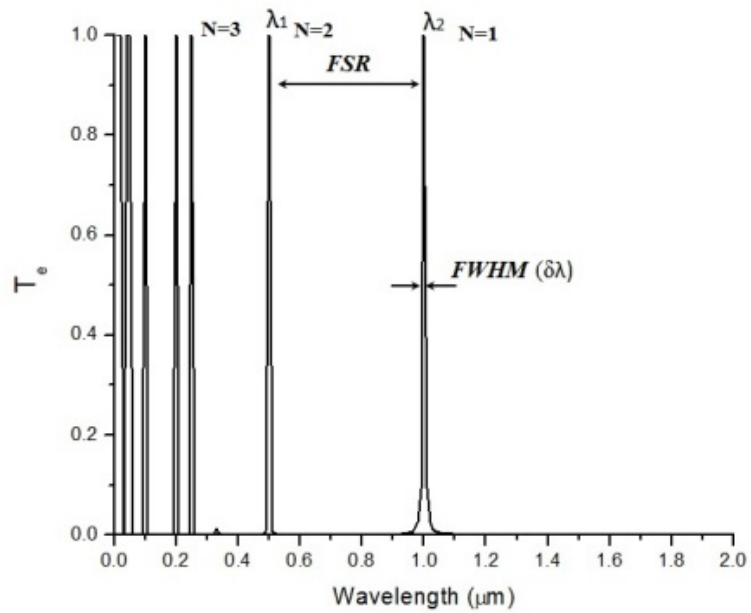
Fig. 2. 5 Transmission of a FP cavity (l=0.5µm, R=0.98, n=1) [65]

2.3   Guided-Mode Resonance Filters

Another promising post-growth wavelength selection mechanism utilizes the guided-mode resonance properties of dielectric waveguide gratings [70]–[73]. As one kind of the Wood's anomalies, the resonance type receives less attention than the classical Rayleigh type [73]–[75]. However, the guided-mode resonance waveguide grating has drawn the attention of researchers since the early 1990s for its diffractive and waveguide characteristics. Sharp resonance corresponding to almost 100% energy transition arises when the externally propagating waves are coupled to adjacent leaky waveguide modes associated with higher-order diffracted waves [76]. When an external wave is phase matched to a waveguide mode supportable by the structure, the periodic grating element can provide the necessary phase matching even at normal incidence [42], [75]–[79]. One can use the guided-mode resonance

18

effect to design transmission band-pass filters by combining the resonance effect of a waveguide grating with the high reflectivity (HR) property of a high-n/low-n thin film stack with quarter-wave thicknesses. By changing the period and fill factor of the gratings, wavelength(s) of interest can be selected effectively [54], [75], [77], [80]. Since the resonance wavelengths are scalable to the grating dimensions, it is advantageous to pattern the arrays using traditional optical lithography for feature size larger than half a micron [40], [54]. The first theoretical contribution about the resonance-type anomaly was by Hassel and Oliner, in which the grating was viewed as a purely reflective reactance surface [73]. Bertoni *et al* theoretically studied the frequency-selection characteristics of a periodic dielectric layer with a square-wave profile [81]. Experimental result reported by Sharon *et al* has shown 90% efficiencies by using embedded transmission gratings [73]. Wang and Magnusson have shown that nearly ideal reflection filters can be realized by combining traditional thin-film optics with diffractive and waveguide optics [76]. Experimental results obtained by Gale *et al*. and Peng and Morris in the visible region, by Meriakri *et al*. in the millimeter-wave region, and by Magnusson *et al*. in the microwave region have confirmed the theoretical model used to design resonance grating filters [74], [76]. Kuo-Wei Lai *et al*. have incorporated DBRs with the two dimensional gratings as a resonant cavity to select wavelengths simultaneously [40]. Compared to FP filters, resonance gratings can have fewer stack layers, but the fabrication of sub-micron diffraction feature with precision and uniformity using traditional photolithography is the primary challenge. In addition, one-dimensional (1D) gratings are polarization sensitive which may not be ideal for some applications.

In this work, a transmission filter is designed by taking advantage of the resonance minimum in the reflection curve and the HR characteristics of the multi-layer high-n/low-n

grating structures. The basic concept for analyzing the diffraction properties of a general planar structure with interleaved, arbitrarily ordered, modulated and un-modulated multi-layers is by uses the classic rigorous coupled-wave theory [73], [74]. In the traditional thin-film design for transmission filters, HR quarter-wave pairs in the absence of resonance are the basic elements [76]. Homogeneous dielectric layers with high-n/low-n are stacked in an alternating manner to provide desired reflectivity. As for guided-mode resonance-based design, either layer of the pair, or both, is/are modulated spatially [82]. The modulated region (grating) might be placed on top, embedded, or at the bottom of the waveguide region, which consists of several quarter-wave pairs (Fig. 2.6). Λ and FF represent the period and the fill factor [79]. The number of layers needs not to be even [82].

(a)   (b)
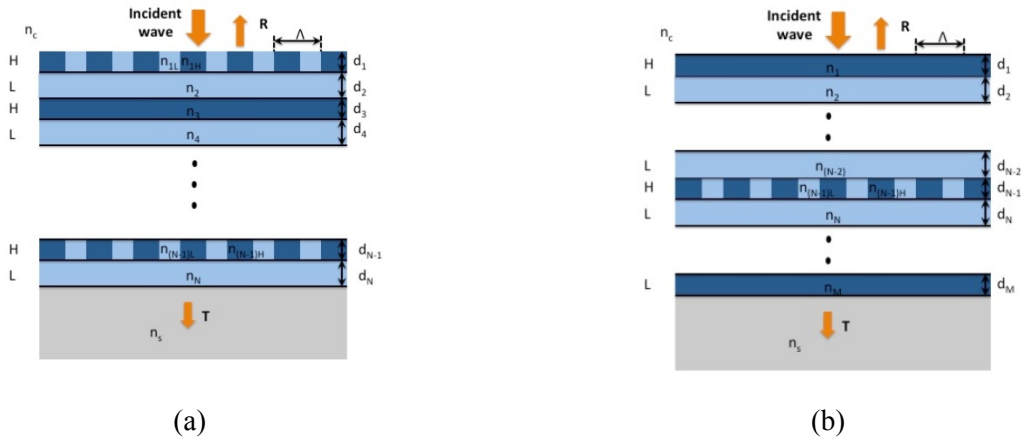
Fig. 2. 6 Schematic of the multi-layer, square-wave profile waveguide grating models with (a) grating on top/bottom (b) grating embedded. The zero-order reflected wave (R) and the corresponding transmitted wave (T) are propagating waves with all higher-order diffracted waves being cut off at normal incidence [82].

A fundamental two-layer transmission filter is used as an example to illustrate the concept [76]. The first layer is square-wave modulated, and the second layer is homogeneous. The complete transmission occurs at the wavelength that corresponds to the resonance minimum

in the reflection curve. The asymmetrical resonance minimum takes place when the layer thicknesses deviate from half wavelength at resonance. Particularly, an asymmetrical line can be produced using quarter-wave stacks with thicknesses of d_i in this case. At the non-resonance spectral region, the waveguide grating resembles a thin film with the effective refractive index $n_{i,eff}$.

$$d_i = \lambda/(4 * n_{i,eff}) \tag{2.3.1}$$

$$n_{i,eff} = \begin{cases} n_{i,H} * ff + n_{i,L} * (1 - ff) & for\ square-wave\ grating\ layers \\ n & for\ homogeneous\ layers \end{cases} \tag{2.3.2}$$

The reflectivity of the HR stacks can be approximated as [83]

$$R = \left(\frac{1 - \frac{n_s}{n_c} (\frac{n_{1,eff}}{n_{2,eff}})^{2N}}{1 + \frac{n_s}{n_c} (\frac{n_{1,eff}}{n_{2,eff}})^{2N}} \right)^2 \tag{2.3.3}$$

where in this study, $n_{1,eff} = (n_{1H} * ff + n_{1L} * (1 - ff))$, $n_{2,eff} = n_2$.

As an example, Fig. 2.7 shows the asymmetrical transmission peak of the double-layer waveguide grating from model (a) with relative high reflectivity in the sideband (TE mode).
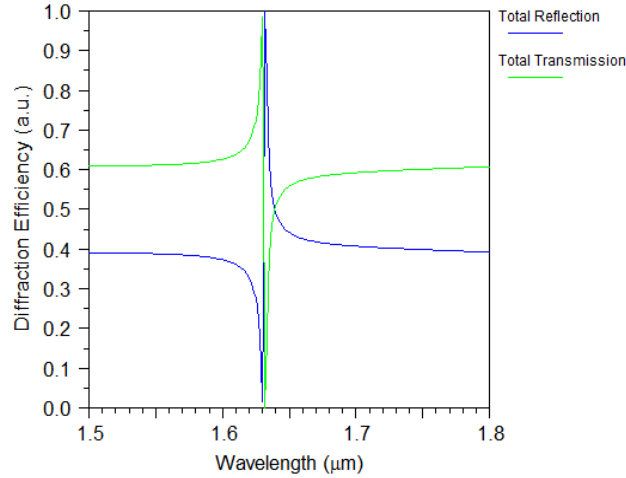
Fig. 2. 7 Transmission/reflection spectra of a double-layer waveguide grating filter at normal incidence (TE mode). Parameters: n_c=1.0, n_{1H}=2.42, n_{1L}=2.28, n_2=1.38, n_s=1.52, Λ=1.0μm, θ'=0°, d_1=0.17μm, and d_2=0.29μm (quarter-wave thickness), FF=0.5 [76].

In order to reduce the sideband transmittance to arbitrarily low levels, multiple pairs of high-n/low-n quarter-wave layers can be added into the structure. Meanwhile, the effective index of the grating layer must yield an effective index that preserves the high-n/low-n profile of the original homogeneous pairs to maintain the HR property of the stack [82]. It should also be noted that, extra transmission modes will be generated if the number of quarter-wave pairs is increased, which limits the spectral range of the filter in a way that more resonances will appear in the HR regime, and thus has a negative effect on the filter performance.

2.4 Material Characteristics of InP-based Type-II InGaAs/GaAsSb Photodetectors

Besides the filter, the other key element of the integrated filter device is the broadband photodetector. For a wide wavelength tuning range, the photodetector should have high photoresponse in the wavelength regime of interest so as to possess distinguishable wavelength peaks when coupled with filters. The photoresponse is essentially determined by the absorption

22

(active) region of the photodetector. For our InP-based PIN photodetector, the absorption region consists of multiple pairs of $In_{0.53}Ga_{0.47}As/Ga_{0.5}As_{0.5}Sb$ quantum wells (MQW). The external quantum efficiency of a photodetector is used as the criteria for comparison with a more commonly used InP photodetector that has an InGaAs absorption layer with a similar thickness. The result shows that at room temperature, the MQW photodetector has acceptable dark current and comparable high quantum efficiency in the NIR region, making it a good candidate for the multispectral application in this regime.

2.4.1   Active Layer

As mentioned before, the absorption efficiency is critical for the ultimate detection efficiency [13]. To confirm the high NIR photo-response of the $In_{0.53}Ga_{0.47}As/Ga_{0.5}As_{0.5}Sb$ MQW photodetectors lattice-matched (LM) to InP used in this study, I measured the quantum efficiency of these photodetectors from 0.85 to 1.8μm. Sample A has a thick absorption region composed of 100 pair $In_{0.53}Ga_{0.47}As$ /$Ga_{0.5}As_{0.5}Sb$, grown by using Molecular Beam Epitaxy (MBE). For comparison, the quantum efficiency of Sample B - a bulk InP photodetector with an absorption region of 1μm InGaAs was also measured. Top-illuminated mesas for both structures were fabricated using the same process flow: photolithography, mesa-etch, passivation, metal deposition and lift-off. Acids of 3%-Br:CH_3OH and H_3PO_4:H_2O_2:H_2O(1:1:10) were used to etch the mesas. Approximately 210 nm of SiO_2 was deposited as a passivation layer by using plasma-enhanced chemical vapor deposition (PECVD). Cr (40nm)/Au (100nm) was deposited as the n- and p-contacts. The structures are shown in Fig. 2.8 [13].

<table>
<tr><td colspan="2" align="center">500 nm p+ InP</td></tr>
<tr><td colspan="2" align="center">25 nm InP (uid)</td></tr>
<tr><td colspan="2" align="center">18 nm InGaAs (uid)</td></tr>
</table>

| (a) | (b) |
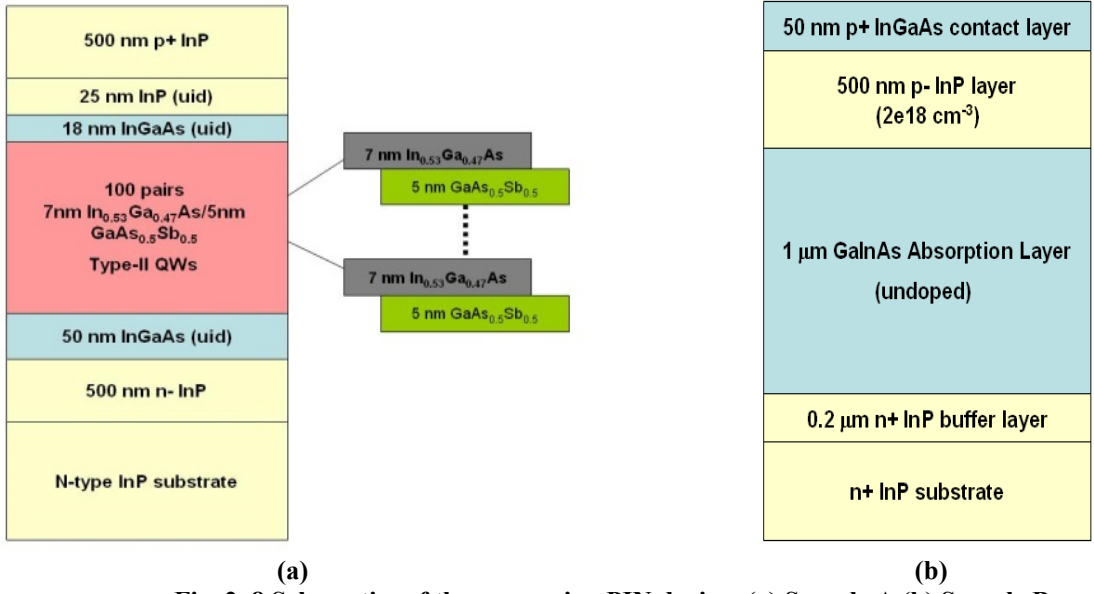
Fig. 2. 8 Schematics of the comparing PIN devices (a) Sample A (b) Sample B

2.4.2   I-V and Quantum Efficiency Characteristics

The dark current-voltage (I-V) characteristics were measured using an HP 4156B semiconductor parameter analyzer. Figure 2.9 shows the average dark current versus voltage for five devices from structures A and B. The average dark current for structure A is consistent with other published results for type-II InGaAs/GaAsSb quantum well absorption regions [56], [84]. The reason for the higher dark current in structure A is more thermal carriers due to the smaller effective bandgap, and interfacial defects formed during growth of the quantum well absorption region.

Since the dark current characteristics of the devices were similar, one device for each structure was used for QE measurements. The room-temperature quantum efficiencies of the devices were measured using a tungsten-halogen light source, a spectrometer, a long pass optical filter with a cut-off wavelength of 0.8 µm, and a lock-in amplifier. The reference was a

calibrated InGaAs detector with photo-response from 0.8 μm to 1.8 μm, from Thorlabs. Quantum efficiencies were calculated by equation (2.4.1):

$$\eta_{QE} = \frac{I_{sample} \times R_{reference}}{I_{reference}} \times \frac{1240}{\lambda(nm)} \tag{2.4.1}$$

where I_{sample} and $I_{reference}$ are the measured photocurrent of the samples and the reference. $R_{reference}$ is the responsivity of the reference. λ is the according wavelength, and η_{QE} is the calculated quantum efficiency. Figure 2.10 shows the quantum efficiency of each structure at reverse biases of 1 V and 2 V. Reverse biases above 2 V for structure B did not lead to a higher quantum efficiency due to 100% carrier collection efficiency. The quantum efficiency for structure A does not vary significantly for reverse biases larger than 1 V. As can be seen, the quantum efficiency of structure A is higher than structure B over the entire range.
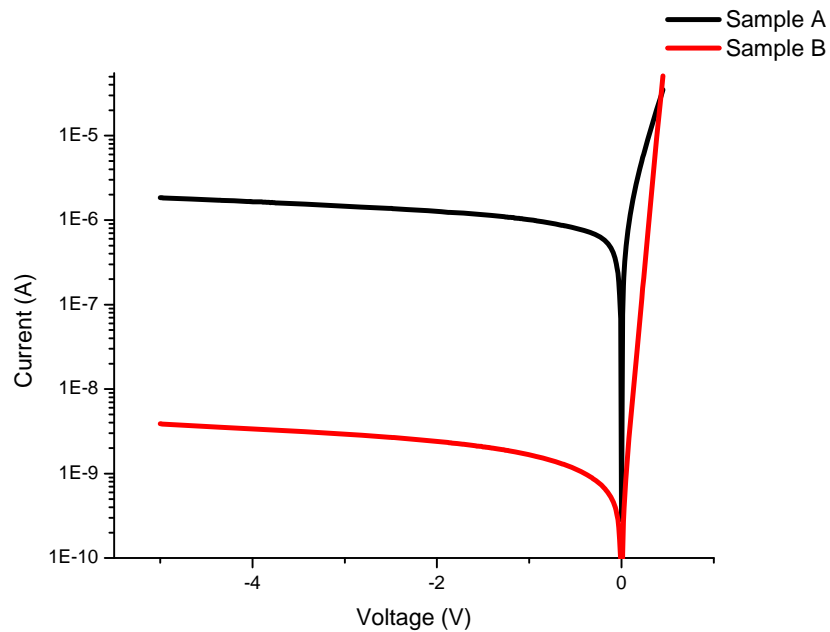
Fig. 2. 9 Dark current characteristics of structure A and B at room temperature. Mesa diameter = 180 μm

Since structure A has a thicker absorption region than structure B, calculations of the quantum efficiency for the 1.2 μm bulk InGaAs/InP absorption region device was performed using Crosslight - APSYS. To be consistent with the experimental results, a SiO$_2$ layer of approximately 213 nm was used as the anti-reflection coating (ARC) and the passivation layer. The absorption coefficient (α) of the InGaAs bulk was extracted from the experimental data using equation (2.4.2):

$$(1-R)(1-e^{-\alpha L})\eta_{carriercollected} = \eta_{QE} \tag{2.4.2}$$

where R denotes the measured reflectivity of the AR layer. L is the thickness of the absorption layer. This expression assumes that all carriers created in the absorption region are collected. The simulation results (also included in Figure 2.10) show that the 1.2 μm InGaAs bulk will have a lower quantum efficiency than structure A in the spectrum range 0.85 μm to 1.8 μm. While the reason for this is not known at this time, we believe that type-II transitions from other bound states may be contributing to the responsivity.
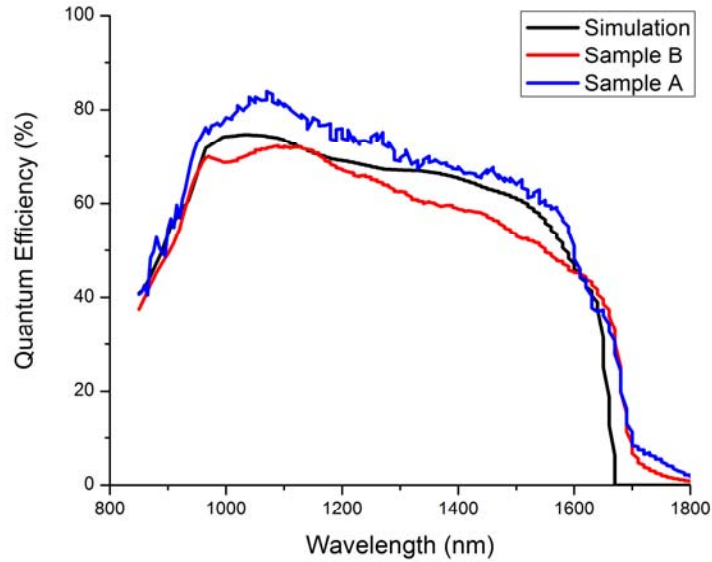
Fig. 2. 10 The measured quantum efficiencies for structure A and B at a reverse bias of 1V and 2 V, respectively. The expected quantum efficiency of a 1200 nm bulk InGaAs photodiode is also included.

The QE beyond λ=1.8μm of Sample A was measured in an FTIR, and photo-response up to 2.8μm was observed by Baile Chen *et al.* for this MQW structure [14]. The absorption region of 100 pairs of $In_{0.53}Ga_{0.47}As/Ga_{0.5}As_{0.5}Sb$ exhibits high responsivity in the NIR regime and acceptable photoresponse in the SWIR regime. This feature enables high quantum efficiencies at wavelengths of interest as will be shown in the following chapter.

Chapter 3 Absorption Characteristics of InP-based Type-II InGaAs/GaAsSb Multiple Quantum Well Photodetectors

In this chapter, the fabrication process and characterization of the InP-based type-II $In_{0.53}Ga_{0.47}As/Ga_{0.5}As_{0.5}Sb$ multiple quantum well photodetectors are demonstrated in detail. The photodetectors have the same absorption region as the devices discussed in Chapter 2, but with a different n region. These photodetectors will be used in the design and fabrication of the multispectral filters. In this chapter, The external quantum efficiency (EQE) of the photodetectors spanning from 1.1 – 1.8 μm is characterized using the NIR spectroscopy setup as previously introduced, and the photoresponse between 1.8 and 2.8 μm is measured in Fourier Transform Infrared Spectroscopy (FTIR). The results are consistent with Baile, *et al*[14]. The EQE and the surface reflectivity will be combined to obtain the internal quantum efficiency (IQE) of the structure, and the IQE will eventually be used for the calculation of the intensity of the multispectral absorption peaks in Chapter 4.

3.1 Fabrication of Photodetectors

The fabrication of photodetectors follows the standard process as illustrated in 2.4.1, Chapter 2. Top illuminated devices with Au/Ti contacts (p and n) are fabricated for I-V and QE characterizations. The thickness of the device mesas is approximately 2.5 μm, as shown in Figure 3.1. No anti-reflection coating (ARC) or passivation coating was deposited.

500 nm InP (p+)

25 nm InP (i)

25 nm InGaAs (i)

100 pairs
7nm $In_{0.53}Ga_{0.47}As$/5nm
$GaAs_{0.5}Sb_{0.5}$
Type-II QWs

50 nm InP (i)

1000 nm InGaAs (n+)

200 nm InP (n+)

30 nm InGaAs (n+)

N-type InP substrate

2.5µm

5 nm $GaAs_{0.5}Sb_{0.5}$

7 nm $In_{0.53}Ga_{0.47}As$

5 nm $GaAs_{0.5}Sb_{0.5}$

7 nm $In_{0.53}Ga_{0.47}As$
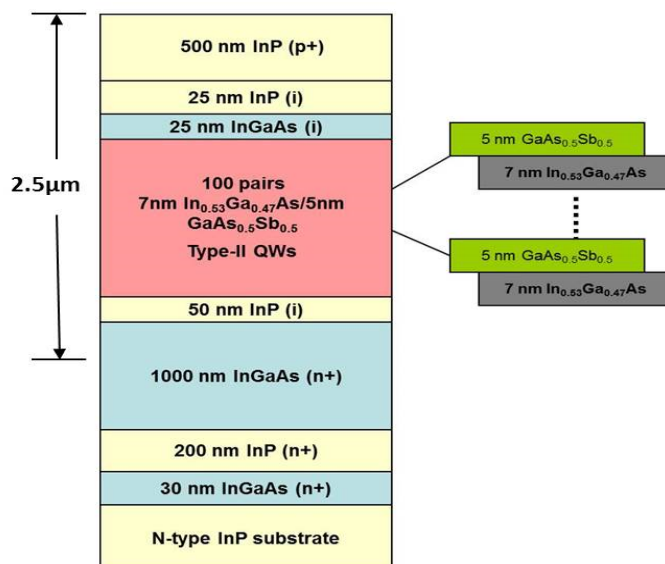
Fig. 3. 1 Schematic of the type-II MQW photodetector discussed in Chapter 3 and 4.

3.2   Characterization of Photodetectros

3.2.1   Current-voltage characteristics

The room-temperature dark current-voltage (I-V) characteristics of the photodetectors were measured using an HP 4156B semiconductor parameter analyzer. Only devices with larger surface areas (diameter $\geq$ 250 µm) are measured for ease of future filter implementation. Five samples of different sizes were measured and the results were averaged. For devices with a diameter of 250 µm, a dark current density of 2×10^{-2} A/cm^2 at -10V was observed. The I-Vs show very little variation, and the averaged result for each size is shown in Figure 3.2. The dark current characteristics are consistent with earlier publications by Baile Chen, *et al* [14], [56], [84].
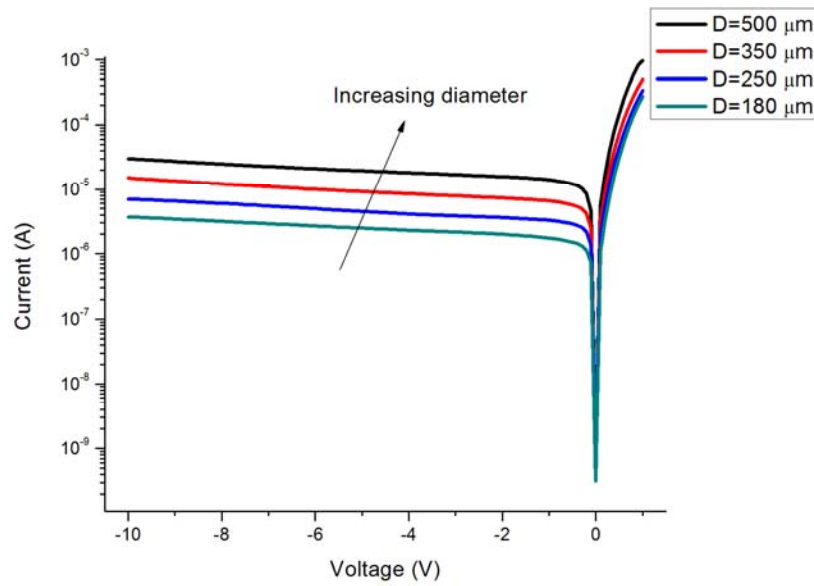
Fig. 3. 2 Average room-temperature dark current characteristics of the InP-based type-II MQW photodetectors

3.2.2 External quantum efficiency characteristics from 1.1μm to 2.8 μm

The spectral response of the photodetectors are measured using a NIR setup and an FTIR for wavelength regimes of 1.1 – 1.8 μm and 1.8 – 2.8 μm, respectively [13], [14]. The NIR setup comprises a spectrometer, a tungsten-halogen light source, a long pass optical filter with a cut-off wavelength of 1 μm, a lock-in amplifier, and a calibrated commercial Ge photodiode, as mentioned in 2.4.2, Chapter 2. The FTIR setup comprises a Nicolet Magna-II Fourier transform infrared spectrometer and a blackbody source at 700 °C. The working principle of the FTIR and the photoresponse deduced from the calculation will be demonstrated in part b) below.

a) 1.1 μm to 1.8 μm

The MBE grown InP-based photodetector has an absorption region of 1.2 μm InGaAs (7nm)/GaAsSb (5nm) lattice-matched to the InP substrate and was reversely biased at 2 V and no ARC was deposited. The room-temperature external quantum efficiency is reasonably lower than our previous publication mostly due to lack of the ARC layer and absorption layer variation [13]. The result is shown in Figure 3.3.
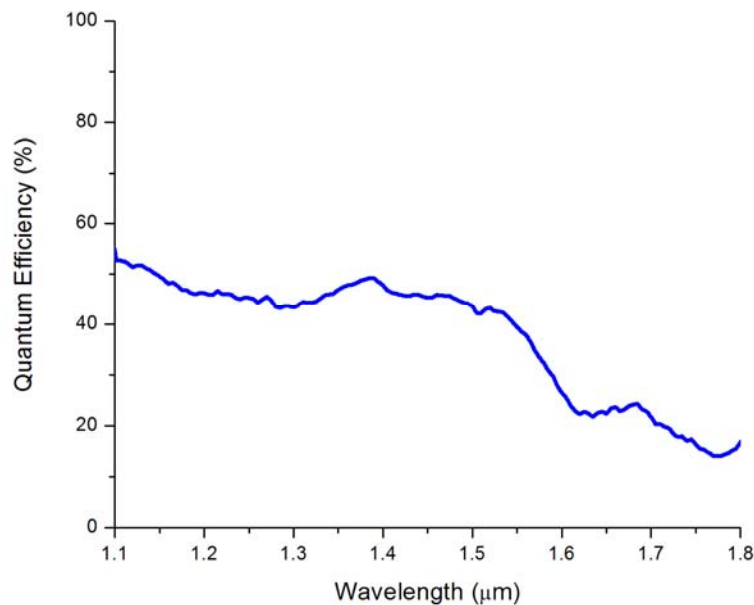
Fig. 3. 3 The room-temperature external quantum efficiency of the InP-based type-II MQW photodetector

b) 1.8 μm to 2.8 μm

The spectral response of the photodetector from 1.8 – 2.8 μm is measured using a Nicolet Magna-II Fourier transform infrared (FTIR) spectrometer and a blackbody at 700 $^{\circ}$C [85], [86]. Figure 3.4 is a schematic of the FTIR spectrometer. The key principle of the FTIR is a Michelson interferometer. As can be seen from the diagram, coherent infrared light is split by a beam

splitter into two arms with 50% of the light transmitted to the fixed mirror, and 50% directed to the moving mirror. The two beams then reflect back to the beam splitter and their amplitudes are combined interferometrically. The resulting interference pattern is typically directed to the detector (built-in or external). The difference in optical path length between the two arms of the interferometer is recorded in accordance with the movement of the moving mirror. Therefore, an interferogram is obtained by recording signal versus different values of the optical path length. The Fourier transform of the interferogram (completed by the computer) can thus convert the raw data (interferogram) into the photoresponse spectrum of the radiation. When a sample is present the background is modulated by the presence of absorption bands in the sample [86].
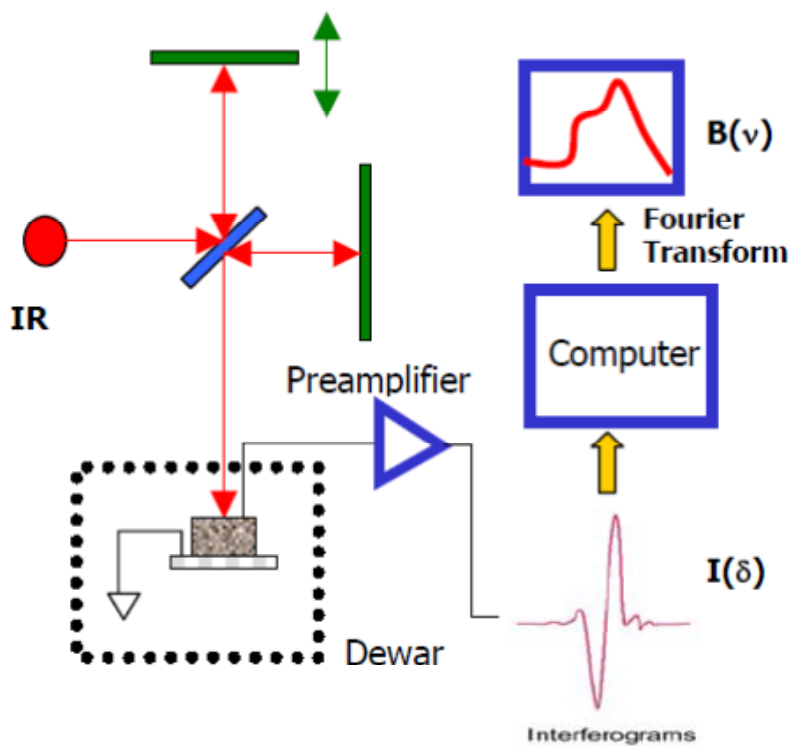
Fig. 3. 4 Schematics of the working principle of FTIR operation

As mentioned above, the FTIR system is capable of collecting raw data from both the built-in detector (a broad band DTGS detector) and an external detector (device to be measured). In fact, dividing the spectrum of the external detector by the spectrum of the built-in detector, a relative responsivity can be obtained. The procedure of deducing the relative responsivity is described as follows.

First of all, the background intensity, also known as the spectrum of the infrared light source, is measured using the built-in standard broad-band DTGS detector, as shown in Figure 3.5.
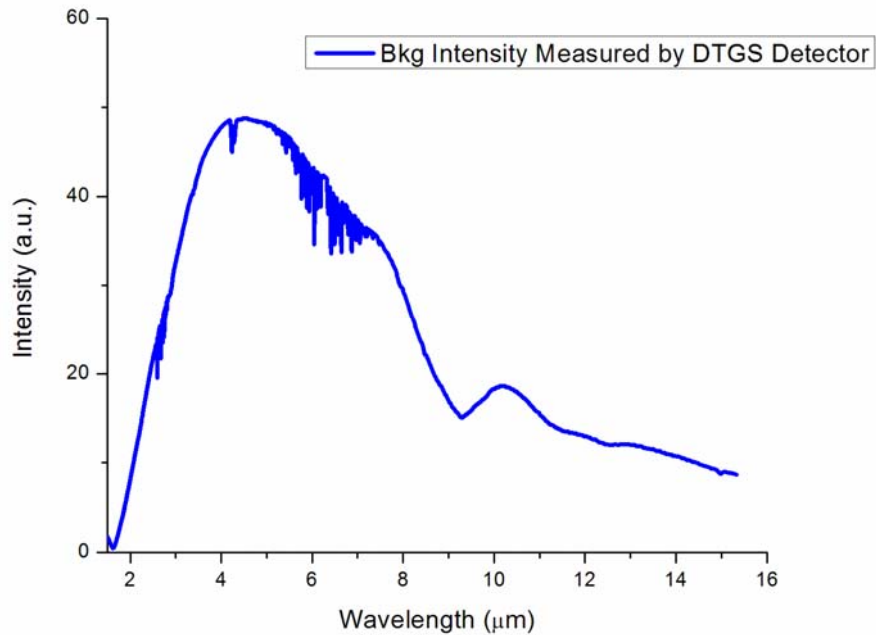
Fig. 3. 5 The background intensity measured using the DTGS detector

Secondly, the external detector (my device) replaces the DTGS detector, and the infrared light spectrum is measured following the same process as in the first step. The measured spectrum is shown in Figure 3.6.
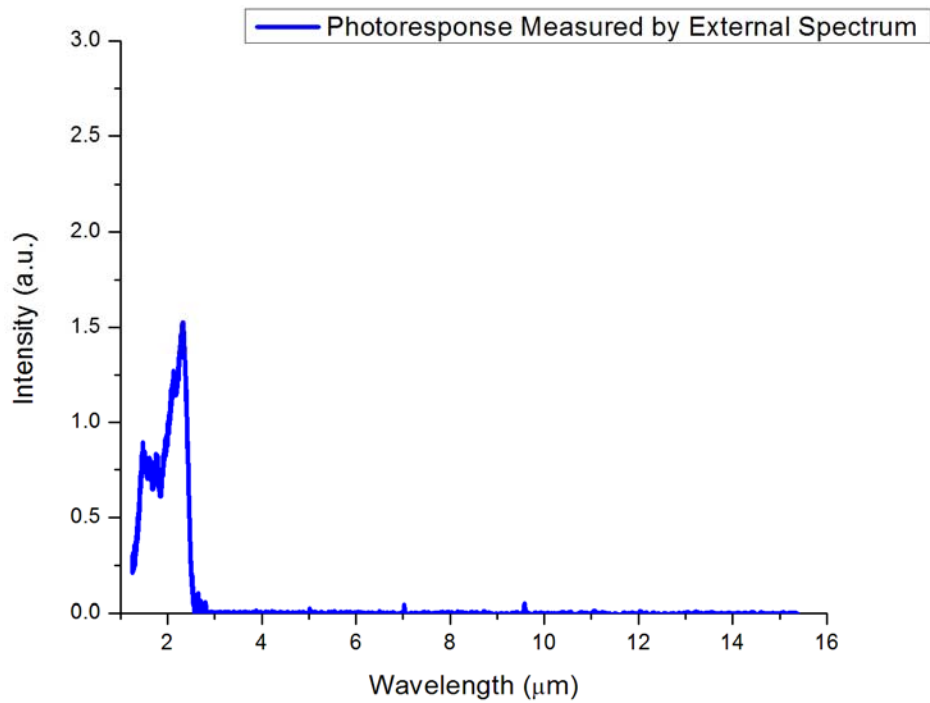
Fig. 3. 6 The infrared light spectrum measured using the external detector

A Stanford Research System (SRS) 570 low-noise current preamplifier is used to amplify the current signal from the external detector during the measurement. Dividing Spectrum 2 by Spectrum 1, we have the relative responsivity, which is shown in Figure 3.7.
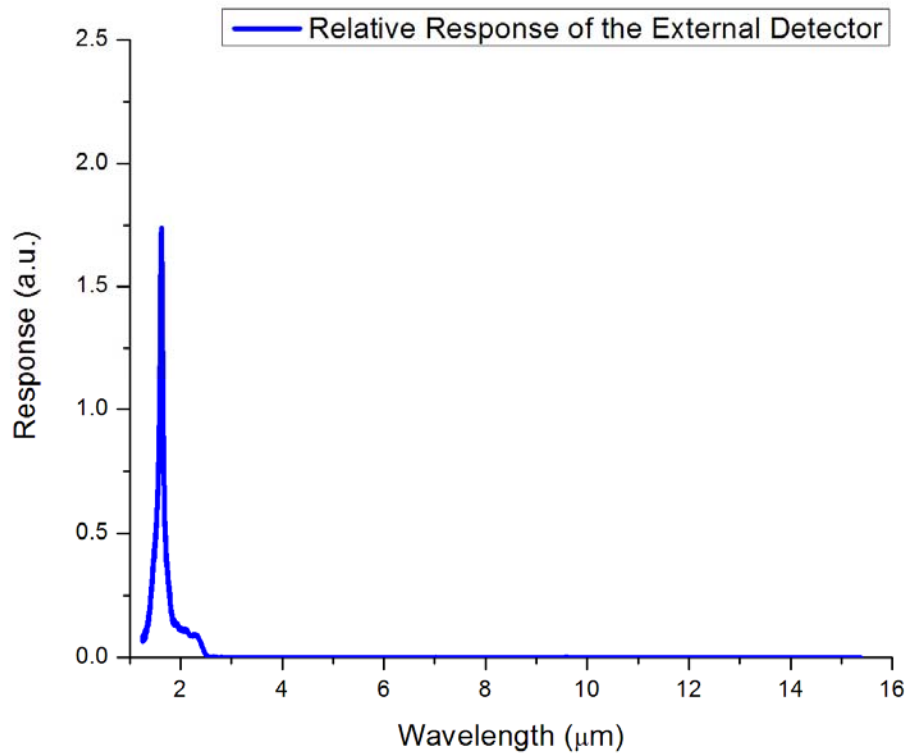
Fig. 3. 7 The relative responsivity of the device measured

Since the DTGS detector is a thermal detector, its responsivity over the whole spectrum can assumed to be flat. However, for wavelength below 1.85 μm, this assumption might not be true due to higher measurement error of the DTGS in this wavelength region. Therefore, the absorption spectrum below 1.8 μm will be measured using the standard QE setup, and the result will be combined with the photoresponse measured in the FTIR.

A blackbody source maintained at 700 °C with a chopper at a modulation frequency of 140 Hz, the SRS 570 current preamplifier, and a Fast Fourier Transform (FFT) spectrum analyzer are used for the calibration of the absolute responsivity of the device. A 1.8 μm long pass filter is placed between the blackbody source and the device chamber to eliminate the

responsivity caused by the type-I (direct) optical transition in the MQW absorption region of the photodetector. The theoretical basis of this technology is explained below.

According to Planck's radiation law, the spectral distribution of energy in the blackbody radiation can be described as [87]:

$$N(\lambda, T) = \frac{2\pi hc^2}{\lambda^5} \frac{1}{e^{\frac{hc}{kT\lambda}} - 1}$$

(3.2.1)

wherein λ is the wavelength, T is the temperature, k is the Boltzmann's constant, c is the speed of light in vacuum, and *N(λ, T)* is the energy per unit time (or the power) radiated per unit area of emitting surface in the normal direction per unit solid angle per unit wavelength by a blackbody at temperature T. The reason why the blackbody radiation at 700 °C is used for illumination is that, according to Wien's displacement law [87], for this temperature the maximum radiation the blackbody produces is at the wavelength of 3 μm, which is suitable for this measurement.

A chopper working at 140 Hz is used to eliminate any background radiation. The power density from the blackbody can be calculated using equation (3.2.2):

$$M(\lambda_1, \lambda_2, T) = \int_{\lambda_1}^{\lambda_2} N(\lambda, T) \, d\lambda$$

(3.2.2)

The power incident on the device (P_{in}) can be obtained by calculating the power transmitted from the filter that is incident on the effective area of the device. The process can be expressed as equation (3.2.3).

$$P_{inc} = [M(\lambda_1, \lambda_2, T)] \times \frac{\frac{\pi}{4} D_{ap}^2}{\pi d^2} \cdot T_{ZnSe} \cdot T_i \cdot A_{det} \cdot MF$$

(3.2.3)

wherein T is the blackbody temperature (700 °C), D_{ap} is the aperture on the blackbody source, d is the distance between the photodiode and the blackbody source, T_{ZnSe} is the transmission of the

window, T_i is the transmission of the 1.8 μm long pass filter, A_{det} is the active area on the device mesa top and *MF* is the modulation factor for the square wave input signal (0.45) for the chopper.

The total current under radiation from the device is measured using the SRS 570 current amplifier and the Fast Fourier Transform (FFT) spectrum analyzer. The ratio (β) can then be calculated using equation (3.2.4) by dividing the absolute responsivity (R_{ab}) by the relative responsivity (R_{re}). The responsivity of the photodetector as a function of wavelength can then be calculated by multiplying R_{re} and β.

$$\beta = \frac{R_{ab}}{R_{re}} = \frac{total\ current\ under\ radiation}{\int_{\lambda_1}^{\lambda_2}[N(\lambda,T)] \times \frac{\frac{\pi}{4}D_{ap}^2}{\pi d^2} \cdot T_{ZnSe} \cdot T_i \cdot A_{det} \cdot MF \cdot R_{re}(\lambda)d\lambda} \tag{3.2.4}$$

Using the method discussed above together with the relative responsivity obtained earlier in this section, the absolute responsivity of the device at room temperature can be determined, as shown in Figure 3.8. The result is consistent with the result published by Baile, *et al* [14], [56], [84].
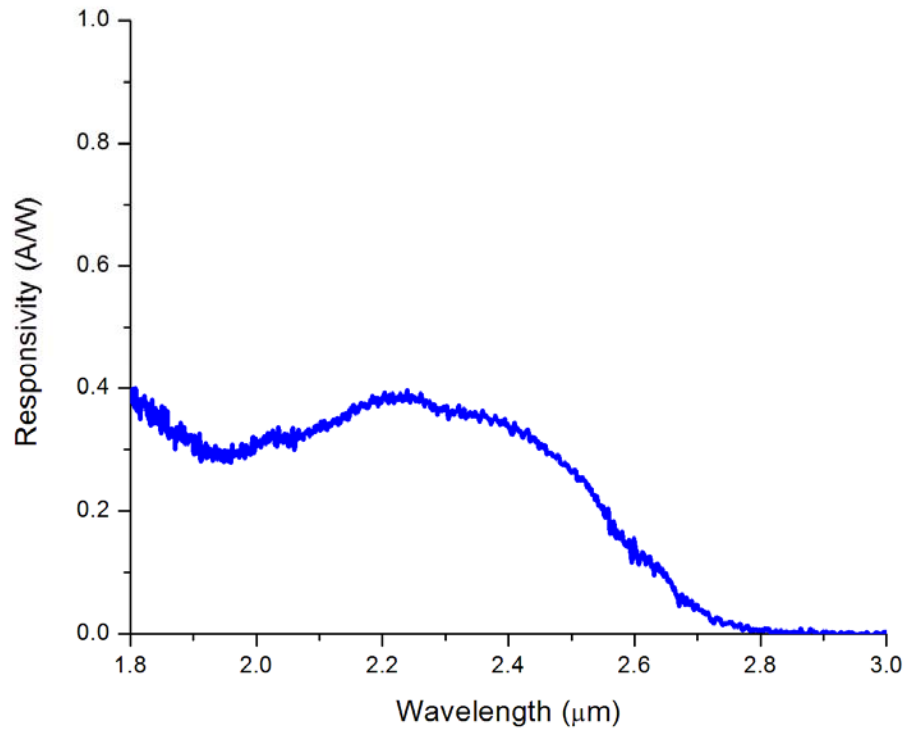
Fig. 3. 8 The absolute responsivity of the device measured

3.2.3   Surface reflectivity characteristics from 1.1μm to 2.5 μm

The surface reflectivity of the photodetector between 1.1 to 1.8 μm is measured in a Perkin Elmer Lamda 950 spectrometer, and the reflectivity between 1.8 to 2.8 μm is calculated using RSoft DiffractMOD 9.0.1 with its built-in database, as shown in Figure 3.9. Material dispersion is taken into account.
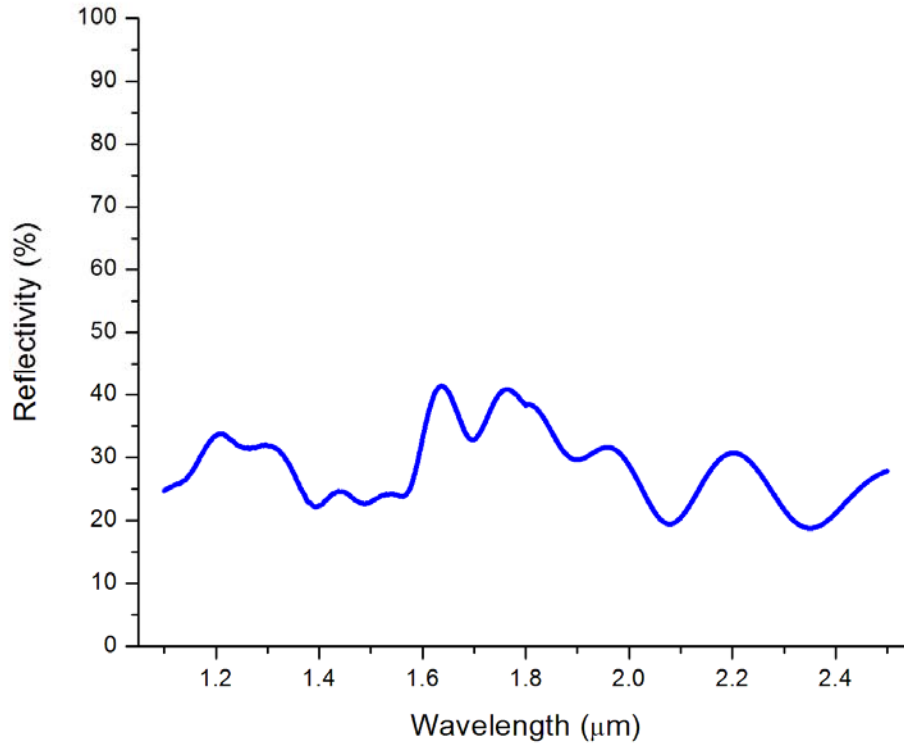
Fig. 3. 9 Surface reflectivity measured using a Lamda 950 spectrometer from 1.1 – 1.8 μm, and simulated using RSoft DiffractMOD from 1.8 – 2.5 μm

The internal quantum efficiency of the photodetectors can be obtained by using equation (3.2.5):

$$\eta_{internal} = \frac{\eta_{external}}{(1 - R_S)\eta_{collection}} \qquad (3.2.5)$$

wherein $\eta_{internal}$ is the internal quantum efficiency, $\eta_{external}$ is the external quantum efficiency, R_S is the surface reflectivity, and $\eta_{collection}$ is the carrier collection efficiency (assumed to be 1). The reverse bias for each measurement is 2 V. Using eq. (3.2.5), the internal quantum efficiency spanning from 1.1 – 2.5 μm can be obtained. The results are shown in Figure 3.10. In this case, the internal quantum efficiency is not close to 100% as is frequently the case for well designed

39

structures and good material quality. There are two reasons for this: 1) a lower external quantum efficiency caused by material non-uniformity, and more importantly, 2) equipment error in reflectivity measurement in the 1.1-1.8 µm regime.
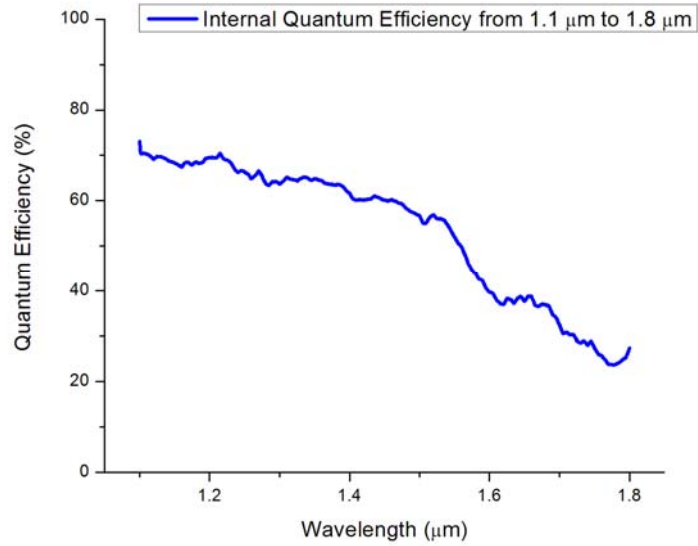
(a)
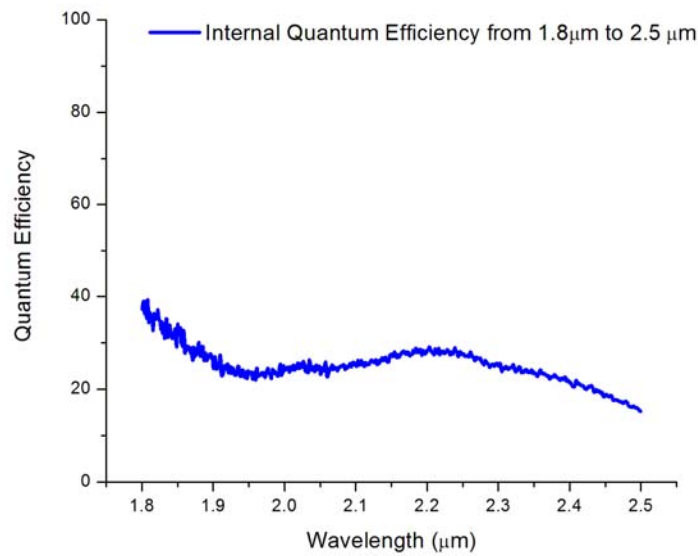
(b)

Fig. 3. 10 Room temperature internal quantum efficiency of the InP InGaAs/GaAsSb MQW photodetector

(a) from 1.1-1.8 µm, and (b) from 1.8 – 2.5 µm

Chapter 4 Software Based Simulations on Wavelength Selection Methods

In this chapter, the transmission and absorption characteristics of the Fabry-Perot filters and guided-mode resonance grating filters are simulated in DiffractMOD 9.0.1 by RSoft. The transmission characteristics are simulated by using InP substrates integrated with the filters, while the external quantum efficiency characteristics are calculated by coupling the internal quantum efficiency with the transmission spectra, assuming all carriers generated are collected. Both techniques have shown significantly high transmissions at wavelengths of interest in the NIR and SWIR regimes, but have considerably different sideband reflectivities and peak widths. A sensitivity analysis is applied to investigate the key parameters that can potentially affect the transmission/absorption peak locations in both filtering techniques. Based on the simulation results and the sensitivity analysis, I will summarize the advantages and disadvantages of both filtering techniques and select Fabry-Perot optical filters for further implementation and study.

4.1   Fabry-Perot Optical Filter

The optical transmission/absorption characteristics of the 8-layer Fabry-Perot filters [66], [67] were simulated using DiffractMOD 9.0.1 by RSoft, as shown in Figure 4.1. The absorption characteristics of the integrated filter devices are calculated by coupling the transmission characteristics of the filters with the internal quantum efficiency of the photodetectors. InP substrates are integrated with the filters and modeled as the reference to verify the transmission characteristics and material properties of the filters. Refractive indices of a-Si and SiO_2 were assumed to be 3.4 and 1.43 over the entire wavelength range of study [88], [89], and no light absorption was assumed for both materials in this regime. The refractive index value for InP is

taken from the RSoft built-in database, and material dispersion is considered only for InP.

Multispectral wavelength detection in the regimes of 1.1 - 1.8 μm and 1.8 – 2.5 μm are investigated to compare with the theoretical predictions in Chapter 2. Two different center wavelengths are used to calculate the thicknesses of the quarter-wave layers for both wavelength regimes. The multispectral transmission/absorption characteristics in the two ranges are presented separately due to the difference in quarter-wave layer thicknesses. In this study, only peaks of the lowest orders are simulated for minimum FWHMs and thinnest cavity lengths.
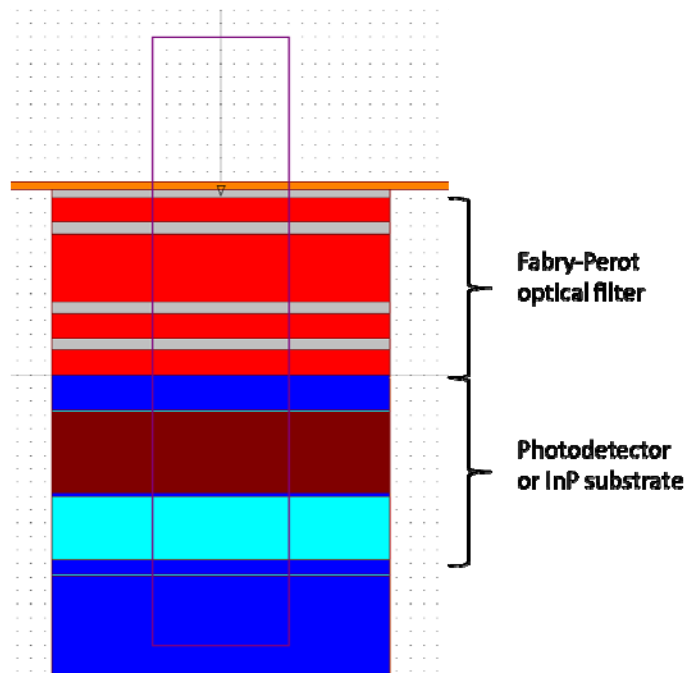
Fig. 4. 1 An illustration of the integrated Fabry-Perot filter in RSoft environment

4.1.1   Simulation for multispectral detection between 1.1 – 1.8 μm

To start, a stop-band center wavelength of 1.6 μm (λ_0) was used to design the DBR pairs for the high reflectivity in the 1.1 – 1.8 μm wavelength regime. Thicknesses of the DBR quarter-wave layers were calculated to be d_1(SiO$_2$)=260 nm, and d_2(a-Si)=110 nm using the equation

QWOT=$\frac{\lambda_0}{4n}$ as discussed in Chapter 2, with λ_0=1.6 μm, and n(SiO$_2$)=1.43, and n(a-Si)=3.4. Filters with different SiO$_2$ cavity lengths (d$_5$=435, 490, 525, 630 nm) were integrated with photodetectors to detect wavelengths at 1.35 μm (λ_1), 1.45 μm (λ_2), 1.5 μm (λ_3), and 1.69 μm (λ_4). Schematics of the filter structure with different cavity lengths and the corresponding simulated transmission/absorption spectrum are shown in Figure 4.2.

As shown in Figure 4.2, in the RSoft environment, a beam of light (intensity equals 1) is incident on the dielectric stack from air (n(air)=1). Owing to the destructive interference of light in the quarter-wave layers, only the portion of light of resonant wavelengths is able to penetrate the stack structure and transmit through to the InP/photodetector. The fraction of light that does not include the resonant wavelengths will be reflected. Therefore, the surfaces to collect the total transmitted light and the total reflected light are set to be in the InP/photodetector and in the air, respectively, to include all the diffracted light. Since no absorption occurs in this process, the fraction of transmission (T) and reflection (R) add up to 1. By varying the cavity length, light of different wavelengths can be filtered and thus detected by the integrated photodetector. The working principle can be shown in Figure 4.2 (a), where the reflection and transmission collection surfaces indicate the defined horizontal domains for RSoft to collect the reflected and transmitted light. Simulation of all four wavelengths all show close to 100% transmission, as shown in 4.2 (b), and the absorption spectrum of each device is obtained by coupling its transmission spectrum with the internal quantum efficiency.
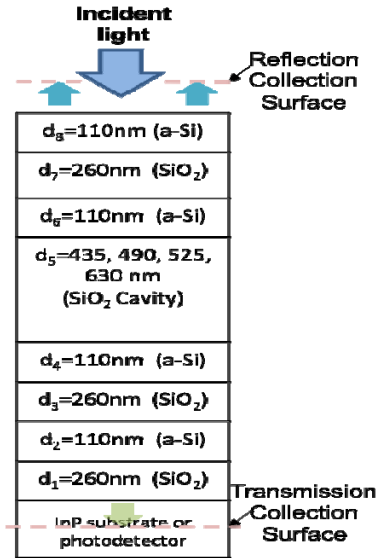
(a)
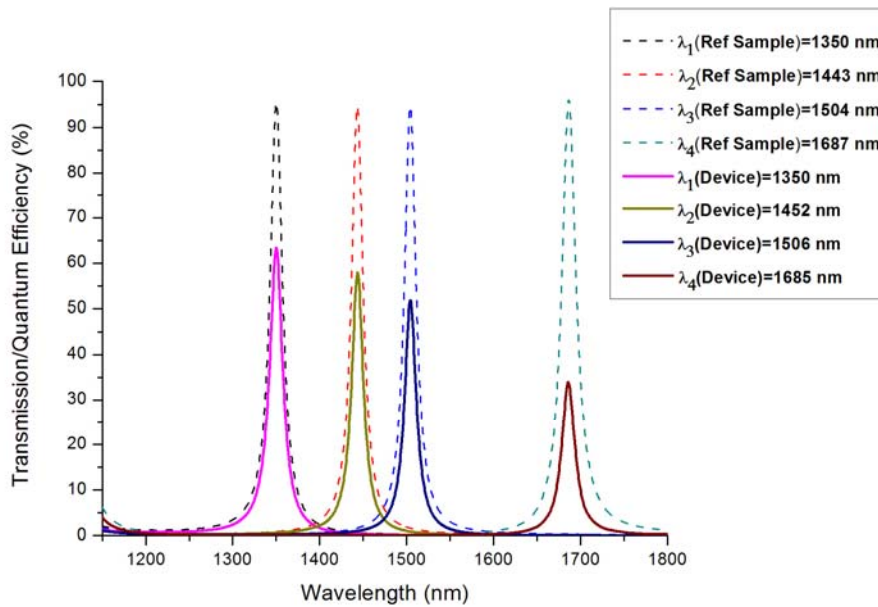
(b)

Fig. 4. 2 (a) Schematic of the 8-layer FP resonant cavity filter structure with cavity length of 435, 490, 525, and 630 nm (b) The simulated quantum efficiencies of the FP filters on photodetectors (solid) and corresponding transmission efficiencies of reference samples (dash) at 1.35 μm, 1.44 μm, 1.50 μm, and 1.69 μm.

4.1.2   Simulation for multispectral detection between 1.8 – 2.5 µm

A stop-band center wavelength of 2.1 µm (λ_0) is used to determine the thicknesses of the quarter-wave layers for the 1.8 – 2.5 µm wavelength regime. The thicknesses of the DBR quarter-wave layers were calculated to be $d_1(SiO_2)$=360 nm, and d_2(a-Si)=150 nm. Filters with different SiO_2 cavity lengths (d_5=1350, 1450, 1550, 1650 nm) were integrated with photodetecotrs to detect wavelengths at 2 µm (λ_1), 2.1 µm (λ_2), 2.2 µm (λ_3), and 2.31 µm (λ_4). Due to the relatively low internal quantum efficiency in this regime, the calculated external quantum efficiencies at four wavelengths of interest are below 25%. Schematics of the filter structure with different cavity lengths and the corresponding simulated transmission/absorption spectrum for each cavity length are shown in Figure 4.3.

(a)
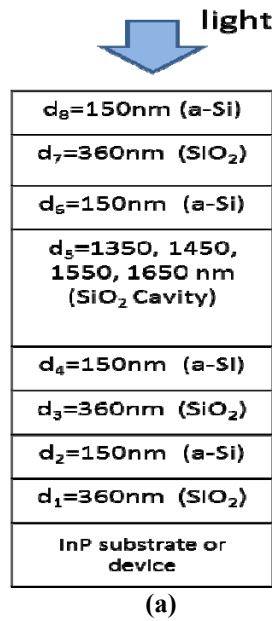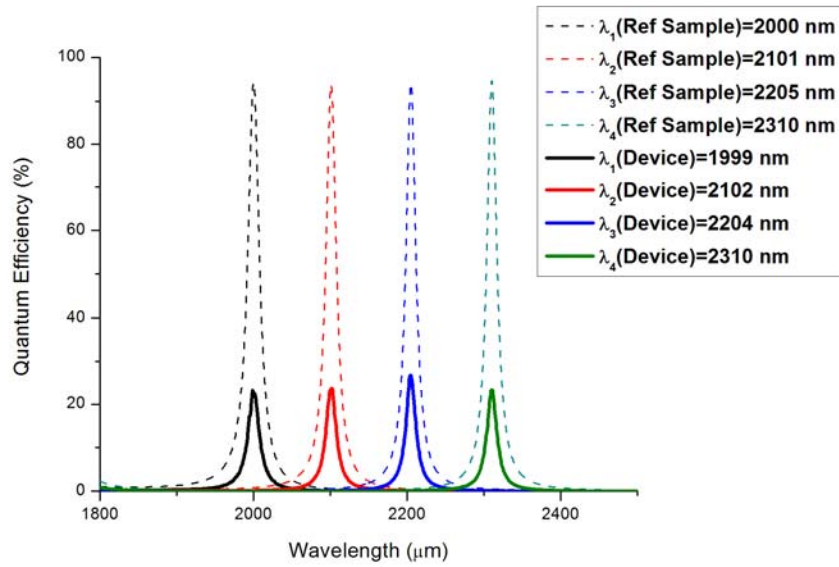
(b)

Fig. 4. 3 (a) Schematic of the 8-layer FP resonant cavity filter structure (b) The simulated quantum efficiencies of the FP filters with cavity length of 1350, 1450, 1550, and 1650 nm on photodetectors (solid) and corresponding transmission efficiencies of reference samples (dash) 2.0 μm, 2.1 μm, 2.2 μm, and 2.3 μm

It can be seen from the our previous discussion in Chapter 2 and the simulation results in this Chapter that, for Fabry-Perot resonant cavity structures, the stopband moves to longer wavelength as the value of the stopband center wavelength (λ_0) increases. This gives rise to thicker quarter-wave layers (d_1 and d_2). However, the key factor that determines the wavelength of transmission is the length of the resonant cavity (d_5), which also increases for longer transmission wavelength (λ_{1-4}). The sideband transmission in the stopband range is effectively eliminated by using a DBR mirror composed of 3 pairs of dielectric layers, which enables highly distinguishable absorption peaks. However, the performance of the integrated device will degrade by low internal quantum efficiency of the photodetectors (Figure 4.3), even if the transmission is high.

To conclude the initial simulation results, wavelength peaks for detection can be effectively tuned by varying the length of the resonance cavity of the Fabry-Perot filter, while the material refractive indices and layer thicknesses of the DBRs define the width and reflection of the stopband. Therefore, by properly adjusting the parameters, multiple wavelength detection can be achieved simultaneously by varying cavity lengths in different integrated filters to detect wavelengths of interest, while multiple pairs of DBRs are used to ensure minimum sideband transmission. The detailed information of the layer thicknesses for the spectral regimes discussed are summarized in Table 4.1.

Table 4. 1 Layer thicknesses of the SiO_2/a-Si Fabry-Perot filters

Set #	SiO_2/a-Si (nm)	SiO_2 cavity (nm)	Wavelength of Selection (μm)
Set 1 (below 1.8 μm) λ_{1-4}	260/110	1) 430 2) 490 3) 525 4) 630	1) 1.35 2) 1.45 3) 1.5 4) 1.69
Set 2 (beyond 1.8 μm) λ_{1-4}	360/150	1) 1350 2) 1450 3) 1550 4) 1650	1) 2 2) 2.1 3) 2.2 4) 2.31

The fabrication process and its challenges will be discussed in detail in the following chapters.

4.2   Guided-Mode Resonance Filter

The two-layer dielectric guided-mode resonance transmission filters (as in Fig. 4.4) for wavelengths at 1.85μm, 1.9μm, 2μm, and 2.2μm were modeled and simulated in DiffractMOD

9.0.1, RSoft. The modulated (first) layer was design to have an a-Si(high-n)/air square-wave profile, the low-n homogeneous layer was design to be SiO$_2$, and the substrate was InP. The length of the a-Si stripes was assumed to be infinite. The numerical calculation of the diffraction is based on Rigorous Coupled-Wave Theory.
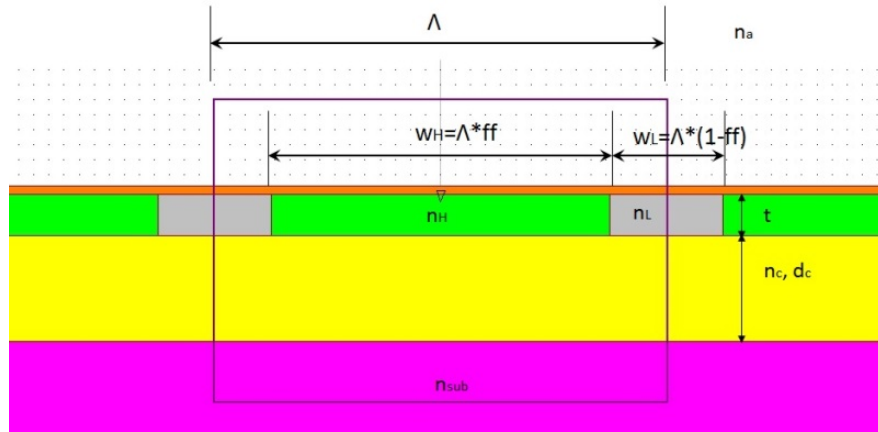
Fig. 4. 4 Schematic of the 1D guided-mode resonance filter in DiffractMOD environment

4.2.1   Effect of parameters

To understand the effect of parameters on the resonance peak, comparisons on the grating period (Λ), the fill factor (FF), the modulation amplitude ($\Delta n=n_H-n_L$), and the layer thicknesses (t, d$_c$) are analyzed in the following.

It is known from previous studies that the diffraction peaks are scalable with the size of the grating features (Λ, FF) [40], [90]. To start, $\Lambda=1.2$ μm and FFs of varying values were used to calculate n$_{eff}$ and thus quarter-wave thicknesses d$_1$ and d$_2$. The resonance wavelength λ was set to be 2 μm. The refractive index for a-Si(n$_H$), SiO$_2$(n$_c$), and air (n$_a$, and n$_L$= n$_a$ in this study) each was set to be 3.4, 1.43, and 1 over the entire wavelengths discussed here, and the refractive index for InP was taken from the RSoft database. Material dispersion was considered only for InP. Zero absorption was assumed. The transmission peaks (resonance minimums) are shown in Fig

4.5 (a), where when FF=1, the modulated grating layer becomes a homogeneous layer, with a reflectivity of roughly 0.78 at λ=2 μm, which is consistent with eq. (2.3.2) and eq. (2.3.3). However, for device fabrication on a single chip, the process will be greatly simplified if d_1 is constant for different wavelength detection. Therefore, investigation of the transmission peaks as a function of different Λ, FF, and d_1 becomes essential for the design. The corresponding simulation results are shown in Figure 4.5.
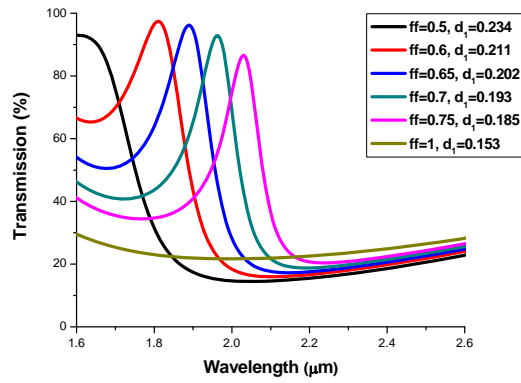
(a)
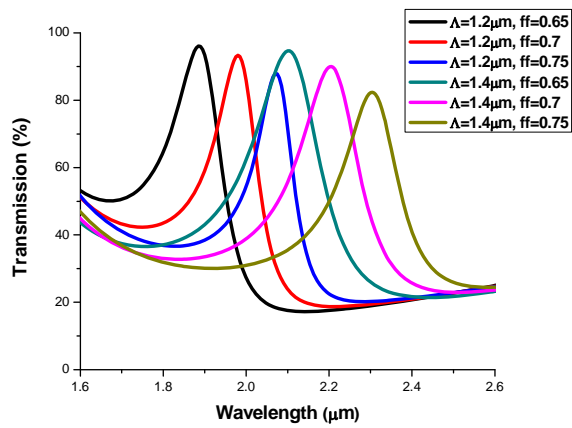
(b)
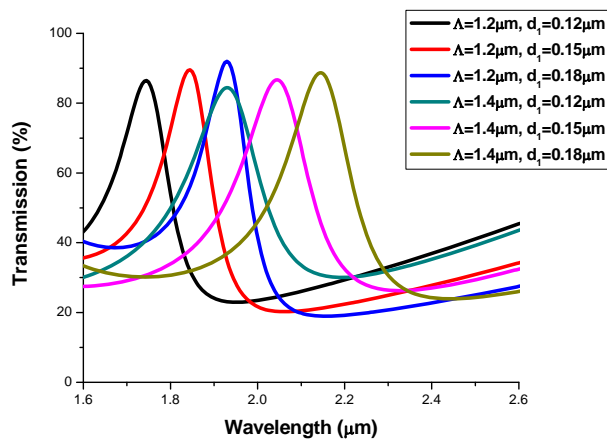
(c)

Fig. 4. 5 Transmission characteristics of resonance grating filters with (a) Λ=1.2μm, d₂=0.35μm   (b) d₁=0.2μm, d₂=0.35μm (c) FF=0.7, d₂=0.35μm

Wavelength tuning trend when SiO$_2$ layer thickness is fixed. At a fixed SiO$_2$ thickness

(d$_2$=0.35 μm), we can see the trends from the graphs: (a) Period fixed (Λ=1.2 μm), changing the

FF from 0.5 ~ 0.75 shifts the transmission peak from 1.8 μm to 2.05 μm; (b) Thickness of a-Si

fixed (d$_1$=0.2 μm), increasing the period and FF can both extend the tuning range. However, the

scalable effect on tuning wavelength is more prominent with period variations. In this example,

the wavelength shifts from 1.85 μm to 2.25 μm as parameters change from Λ=1.2 μm, FF=0.65

to Λ=1.4 μm, FF=0.75. (c) FF fixed, increasing the a-Si thickness (d$_1$) extends the tuning

wavelength from 1.75 μm to 2.15 μm as parameters change from Λ=1.2 μm, d$_1$=0.12 μm to

Λ=1.4 μm, d$_1$=0.18 μm. Also, it can be seen in all three groups that there is also a noticeable

increase in the FWHM as feature size increases. It's worth mentioning that the transmission

efficiency tends to increase with bigger d$_1$, which is different from the trends in (a) and (b) as

feature size increases.

The discussion above and the simulation results suggest that compared to the wavelength

shift by changing FF, varying the grating period Λ can tune the target wavelength more

effectively. However, the FWHMs of the asymmetric peaks tend to increase with larger Λ's,

which has been observed as a trade-off between longer detectable wavelength and detection

precision. Transmission efficiency undergoes a decrease with larger FF, as well as smaller d$_1$. It

should also be noted that the sideband transmission increases with larger grating period Λ, which

also undermines the sensing precision when extending to longer wavelengths.

Optimized parameters of the wavelength tuning design. Since d$_1$ and d$_2$ are flexible post-

growth parameters, it is important to consider all factors (Λ, FF, d$_1$, d$_2$) to determine an

optimized range for sensing from 1.85 μm to 2.2 μm in the design. Having considered different

combinations and trade-offs, adjustment to d$_1$ has been made to optimize the transmission

efficiency and bandwidth for all wavelength simulations. The value of d_1 and d_2 were finalized at 0.15 μm and 0.4 μm, respectively. By changing Λ and FF, transmission peaks of wavelengths from 1.7 μm to 2.7 μm were simulated. The simulated transmission characteristics of our target wavelengths at 1.85 μm, 1.9 μm, 2 μm, and 2.2 μm are shown in Figure. 4.6 (a), and the corresponding simulated quantum efficiencies at the four wavelengths are shown in 4.6 (b). The varying parameters are listed in Table 4.2.

Table 4. 2 Structural parameters of guided-mode resonance grating filters

Sample #	Wavelength of Selection (μm)	Λ (μm)	Fill Factor
1. λ_1	1.85	1.28	0.64
2. λ_2	1.9	1.33	0.64
3. λ_3	2.0	1.35	0.69
4. λ_4	2.2	1.61	0.67
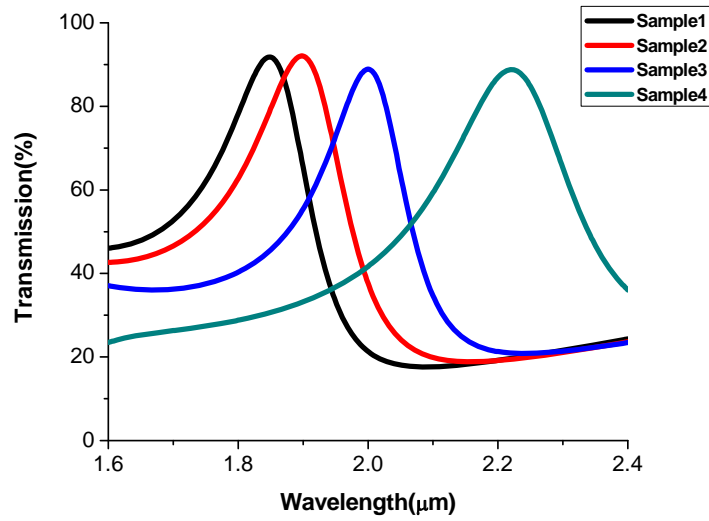
(a)
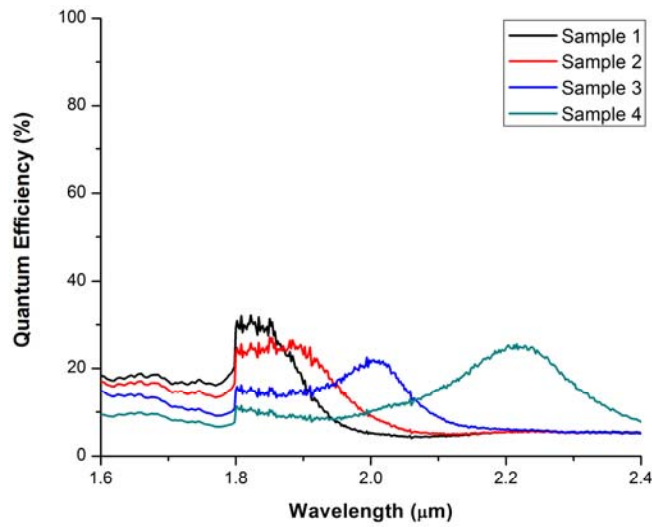
(b)

Fig. 4. 6 The simulated (a) transmission and corresponding (b) quantum efficiency characteristics of Sample 1

to Sample 4 at wavelength 1.85 μm, 1.9 μm, 2.0 μm, and 2.2 μm

It can be seen from Figure 4.6 (b) that the detection peaks are broad with non-zero

sideband photoresponse. This is a direct result of the transmission characteristics. This can affect

the detection precision. The wider quantum efficiency peaks of Sample 1 and 2 are caused by the

inaccurate FTIR photoresponse measurement below 1.9 μm, which was discussed in 3.2.2 as the

high error of the thermal response of the DTGS at shorter wavelength regime for this particular setup.

4.2.2 Practical considerations

There are a few practical aspects that need to be considered based on the simulation results and prior experimental experience. Although there have yet to be any grating fabrications, based on the initial processing trials of the a-Si/SiO$_2$ film deposition/processing, it is reasonable to summarize the considerations as follows:

- The photolithography resolution. The grating feature dimensions have been intentionally designed to meet the resolution limit of the Suss MJB4 mask aligner (400 nm). A thin layer of negative photoresist has been considered to pattern the gratings, while the exposure and developing processes are essential to the ultimate grating patterning/etching, which significantly determines the detection precision.

- Film quality. Since there are only two layers in this grating design, film deposition is comparatively easy to control.

- Selective dry etch of a-Si from SiO$_2$. The etch selectivity has not been calibrated, and it is already known that the selectivity of c-Si is much better and more reliable. Therefore, a time-controlled selective etch is critical to the grating depth, which is one of the key parameters that can affect the transmission.

4.2.3 Sensitivity analysis

From the initial simulation results and the practical considerations discussed above, it is obvious that many variables can potentially cause a discrepancy between simulation prediction and experimental measurement. It is crucial to take the experimental error and potential working

54

condition into account and evaluate the sensitivity of the design given variations on each parameter before implementation to ensure controllable wavelength selections. Therefore, a reasonable range of parameter variations, assumed to be caused primarily by equipment error or working condition variations, are added to the original designed value to estimate the peak shift as a function of parameter variations, and thus the most important parameters can be identified and prioritized for monitoring in the actual experiment.

There are several parameters that might potentially be responsible for a shift of the transmission peaks. Specifically, peak shifting and intensity change due to key parameters regarding the material properties, working temperature, and light incident angle are analyzed below to investigate the sensitivity of the Fabry-Perot filter and the guided-mode resonance grating filter. The wavelength to be filtered is assumed to be 2 μm for both cases.

a.) Fabry-Perot optical filter

The structure is illustrated in Fig. 4.3 (a). The transmission peak shifts due to material properties are displayed in the following graphs. To see the trend without disruption from other inputs, it is assumed that when one parameter changes, all other parameters remain their original values.
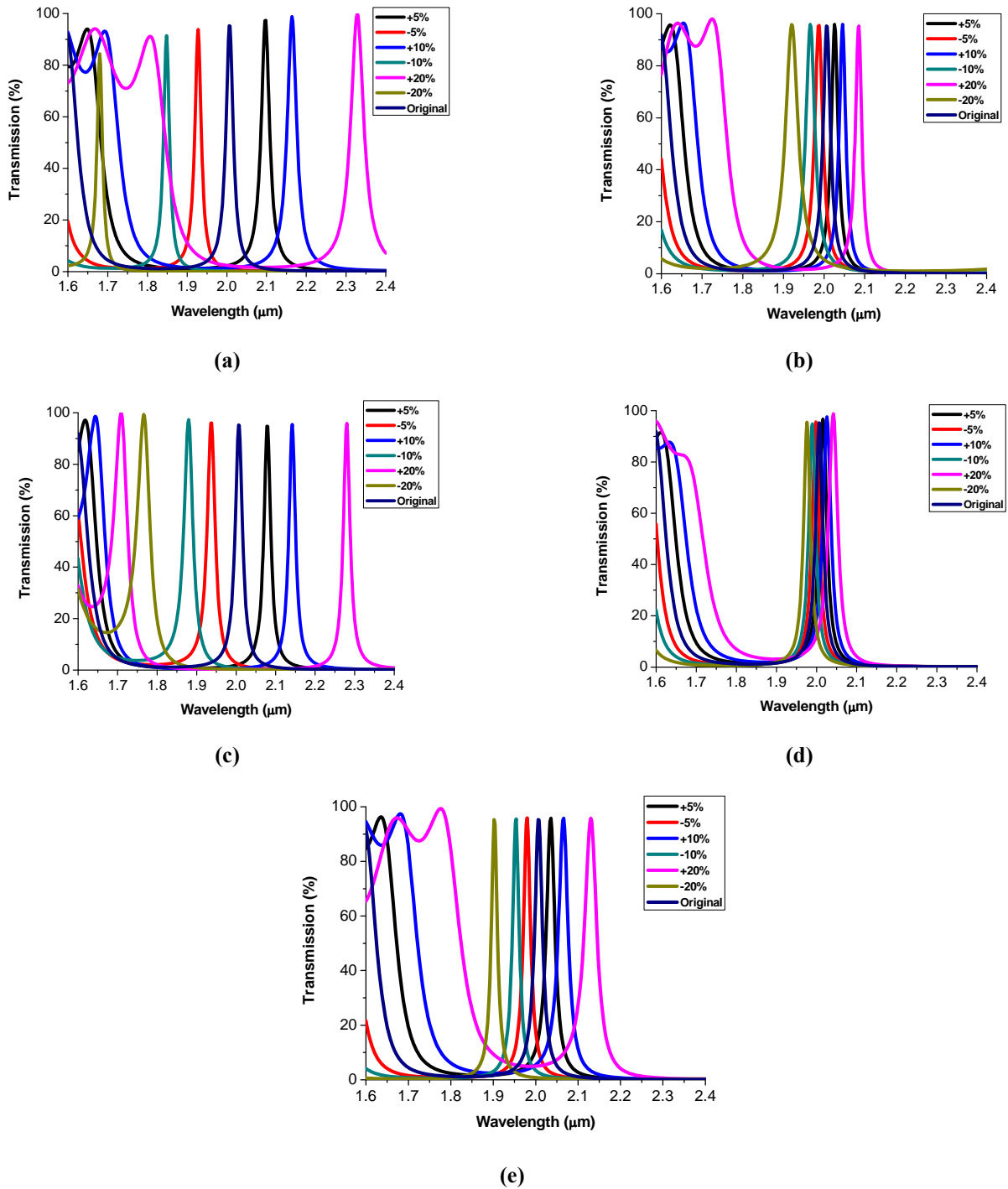
Fig. 4. 7 Simulated transmission peaks with parameter changes of (a) n(SiO₂) (b) n(a-Si) (c) d₅ (d) d₁ (e) d₂ and the corresponding peak shift

The effect of the parameter variations to the peak shift is summarized in Table 4.3.

Table 4. 3 Relative transmission peak shifting caused by parameter variations of the Fabry-Perot filter

Peak Shifting (%) Parameters	Parameter Variation (%)					
	-20%	-10%	-5%	+5%	+10%	+20%
$n(SiO_2)$	**-5%**	**-2.5%**	**-1%**	**1.5%**	**3%**	**6.5%**
$n(a\text{-}Si)$	-4%	-1.5%	-0.5%	1.5%	2.5%	4%
d_5	**-12%**	**-6%**	**-3%**	**4%**	**7%**	**14%**
d_1	-1%	-0.3%	-0.1%	1%	1.5%	2.4%
d_2	-5%	-2.5%	-1%	1.5%	3%	6.5%

* The relative shift is calculated as $(\lambda-\lambda_0)/\lambda_0 \times 100\%$, in which $\lambda_0 = 2$ μm.

*The column on the left includes the important parameters (in blue) that can potentially affect the peak locations. On the right side of the table, the relative peak shifts (in black) caused by the corresponding parameter variations (-20% - +20%, in blue) are calculated.

* The (-) and (+) signs in blue stand for decreasing and increasing the parameter a certain amount from its designed value. The (-) and (+) signs in black indicate the peak moving to a shorter wavelength and a longer wavelength. For example, if d_5 decreases by 5%, its corresponding peak moves to a shorter wavelength by 3% compared to its original peak location.

It can be seen that for a Fabry-Perot filter, the peak location is more susceptible to variations of the cavity length (d_5) and the refractive index of SiO_2. The reason arises from the very fundamental physical basis of the transmittance in the Fabry-Perot cavity, where $\lambda=2nl/N$, with n (the refractive index of the cavity medium) and l (cavity length) directly determining λ (the transmission peak) and N (the operating order) remaining constant. Therefore, it is significant to monitor the cavity length and the SiO_2 quality during the film deposition and the

etch process of the Fabry-Perot filter. In this study, the film quality of SiO_2 is characterized through measuring the material refractive index on a non-absorptive substrate (Si or InP) and monitoring the interface roughness between SiO_2 and a-Si in the SEM. The cavity length is monitored by time-controlled sputtering deposition. Although a commonly acknowledged SiO_2 refractive index in this wavelength regime is approximately 1.5 [88], it is reasonable to have an SiO_2 film with slightly lower refractive index due to deposition condition variations.

In addition, during some applications, light can be incident on the photodetector from various directions, and thus it is important to know how a photodetector's angular dependence of the transmission/absorption peak when the incident direction of light deviates from normal direction. To investigate the variation trend of the transmission/absorption peak as a function of the light's incident angle, an incident angle varying from 0° to 10° and the corresponding transmission peaks are plotted in Fig. 4.8.
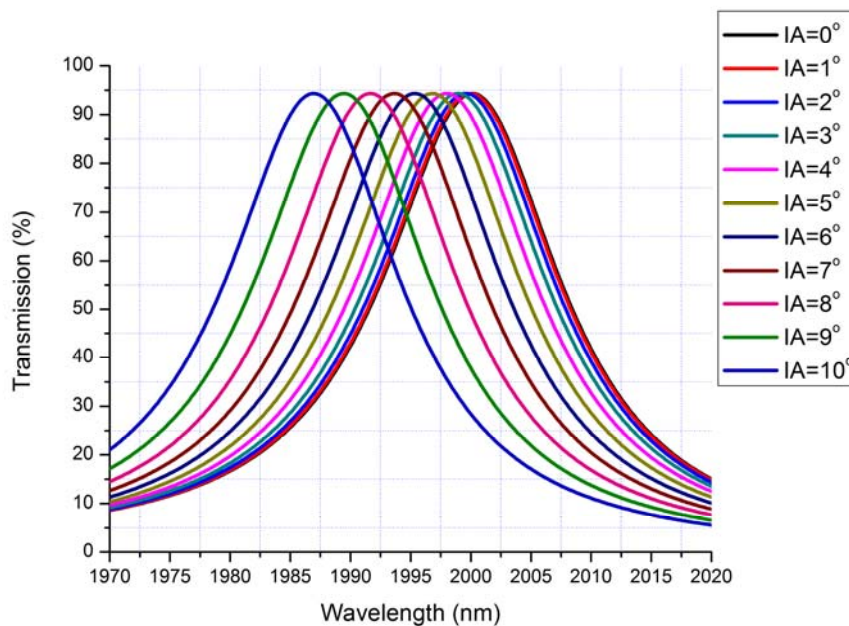
Fig. 4. 8 Transmission through the Fabry-Perot filter at incident angles (IAs) from 1 degree to 10 degrees

In the plot, the transmission peak (at 2 μm when incident angle θ=0°) shifts to shorter wavelengths as the incident angle (θ) increases. The reason for the shift can be explained from equation (2.2.9), where the resonant wavelength λ decreases as cos(θ) decreases to maintain the phase match δ. The DBR stack is not sensitive to incident angle variation [91]. As can be seen that when the incident angle is approximately 2°, there is a 1 nm peak shift in the transmission spectrum. When the incident angle is 4°, the peak shift has increased to approximately 2.5 nm. From the trend of the peak shift simulated above, it can be seen that as the incident angle increases, the peak shifts more significantly towards shorter wavelengths. This suggests the wavelength detecting operation is preferably operated when the incident angle is close to normal. Therefore, for applications that require high detection accuracy, for example, for spectral accuracy better than 2 nm, an incident angle between 3° – 4° is an acceptable choice. Accordingly, to ensure high spectral accuracy and at least close to normal incident angle, the detector should be placed at a distance far away (for example, on a satellite or an aircraft for sensing the object's properties on the earth) from the target to allow light to be incident on the photodetector's surface at an angle close to 90°.

It should be noted that no noticeable change in peak intensity has been observed in the simulated results. From eq. (2.2.13), it can be seen that the transmission intensity is determined by the phase match δ and the mirror reflectivity. Since δ has been met to generate a peak, the intensity is solely dependent on the reflectivity, which does not change significantly at such a small incident angle change.

Moreover, the photodetector's operating temperature can vary according to different operating conditions, and it is necessary to ensure the measurement error caused by temperature

change can be tolerated by the measuring accuracy. To investigate the temperature dependence of the transmission/absorption peak, the refractive indices of SiO_2 and a-Si are calculated at different temperatures by using their temperature gradients, respectively, and the transmission peaks corresponding to temperatures ranging from 100K – 500K are simulated and shown in Fig. 4.9. Normal light incidence is assumed. The temperature gradients for SiO_2 is dn/dT=1.06×10^{-5} /K, and for a-Si is dn/dT=0.00038 /K, respectively [92]–[94].

Table 4. 4 Refractive indices as a function of temperature

Material/Temperature(K)	100	200	300	400	500
a-Si	3.324	3.362	3.4	3.438	3.476
SiO_2	1.4279	1.4289	1.43	1.4311	1.4321
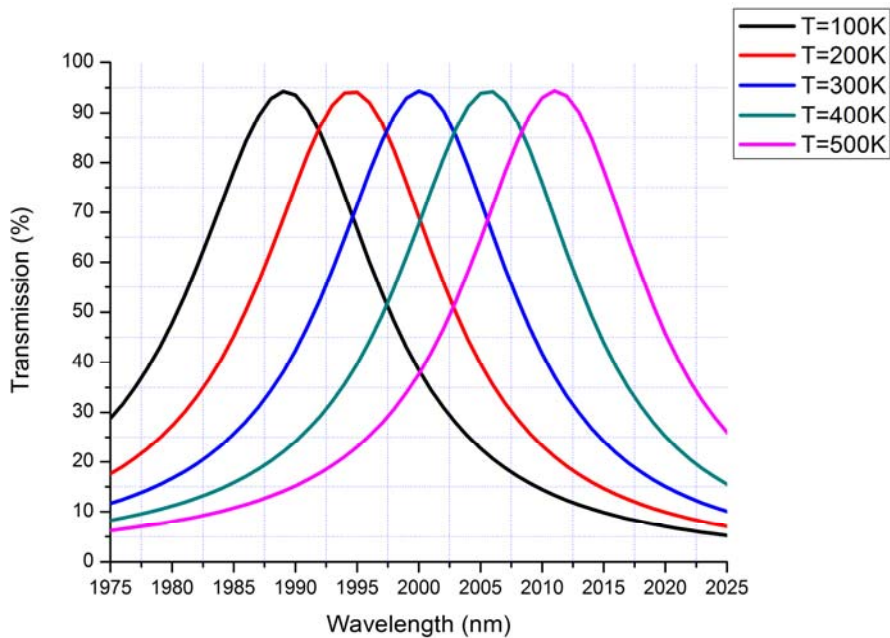
Fig. 4. 9 Transmission through the Fabry-Perot filter at different temperatures from 100K to 500K

In the plot, the transmission peak shifts from shorter wavelengths to longer wavelengths as the operating temperature increases. The reason for the shift can be explained by equation

60

(2.2.15), where the free spectral range varies as the refractive index of the cavity medium varies. It can be seen that in this temperature range, the transmission peak shifts approximately 5 nm for every 100 K change in temperature. It is thus reasonable to conclude that for spectral accuracy better than 2 nm, a temperature variation range within 50 K is an acceptable choice.

b.) Guided-mode resonance filter

The structure is shown in Fig. 4.10. The transmission trends with parameters changes are shown in Fig. 4.11. Still, to see the trend without disruption from other inputs, it is assumed that when one parameter changes, all others remain their original values.
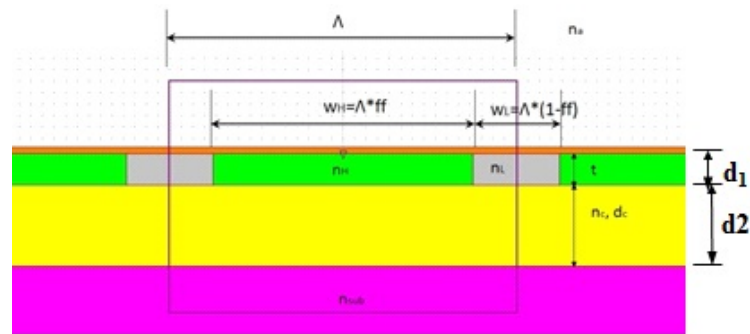

Fig. 4. 10 Schematic of the Guided-Mode Resonance Grating filter on InP structure

(a)

(b)

(c)

(d)

(e)

(f)
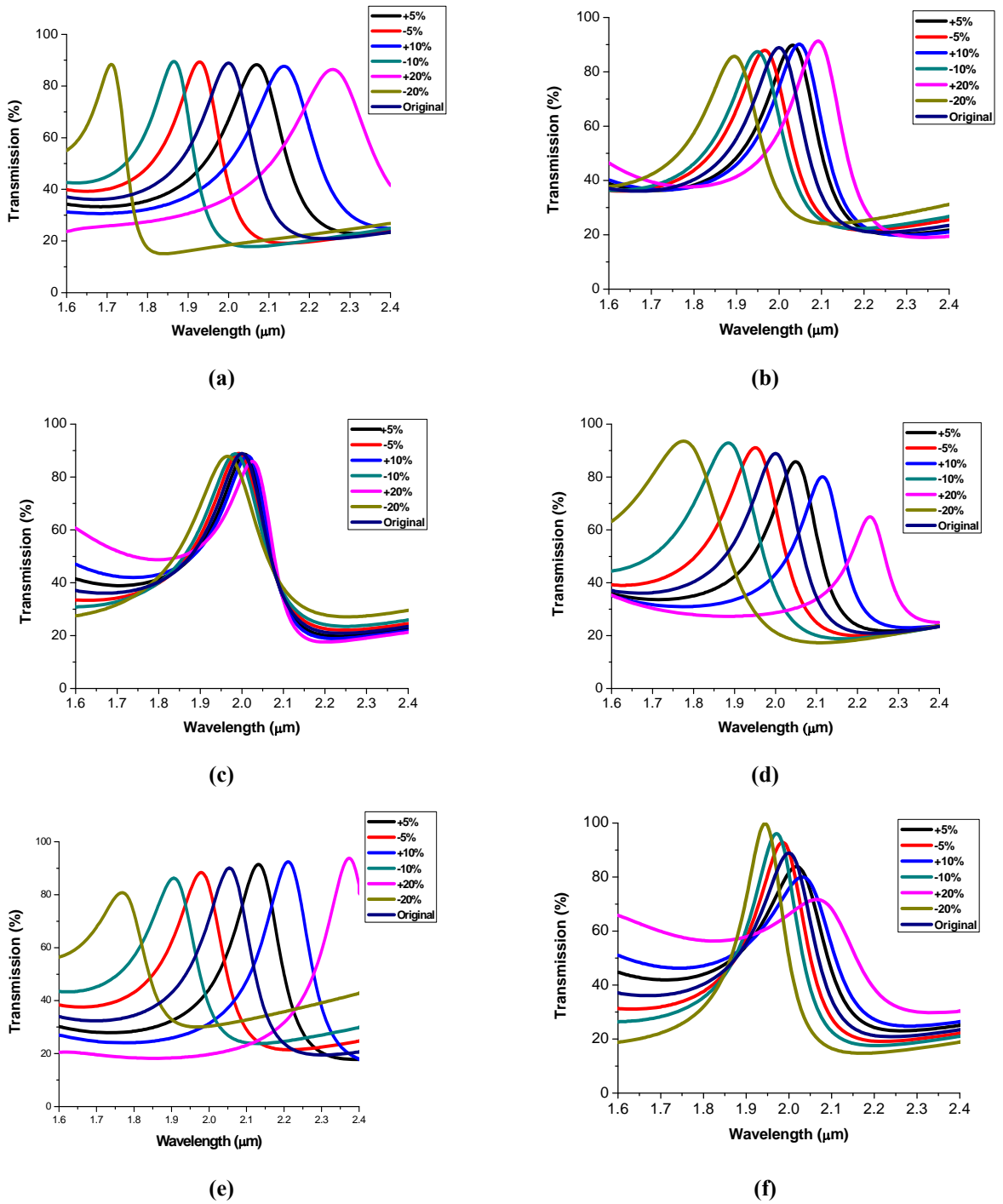
Fig. 4. 11 Simulated transmission peaks with parameters change of (a) Λ (b) d_1 (c) d_2 (d) FF (e) n(a-Si) (f) n(SiO₂)

The effect of the parameter variations to the peak positions shift is summarized in Table 4.5.

Table 4. 5 Relative transmission peak shifting caused by parameter variations of guided-mode resonance grating filter

Peak Shifting (%)	Parameter Variation (%)					
Parameters	-20%	-10%	-5%	+5%	+10%	+20%
Λ	-15%	-7.5%	-4.5%	3%	6%	12%
d_1	-6%	-2.5%	-1.5%	1.5%	2.5%	4%
d_2	-1.5%	-0.6%	-0.5%	0.6%	0.9%	1.4%
FF	-12%	-6.5%	-3.5%	2%	5.5%	11%
n(a-Si)	-13%	-6%	-2%	6%	10%	18%
n(SiO$_2$)	-2.6%	-1.2%	-0.6%	1.2%	1.8%	3.4%

* The relative shift is calculated as $(\lambda-\lambda_0)/\lambda_0*100\%$, in which $\lambda_0=2\mu m$.

* The column on the left includes all the important parameters (in blue) that can potentially affect the peak locations. On the right side of the table, the relative peak shifts (in black) caused by the corresponding parameter variations (-20% - 20%, in blue) are calculated.

* The (-) and (+) signs in blue stand for decreasing and increasing the parameter a certain amount from its designed value. The (-) and (+) signs in black indicate the peak moving to a shorter wavelength and a longer wavelength. For example, if d_1 decreases by 5%, its corresponding peak moves to a shorter wavelength by 1.5% compared to its original peak location.

For the guided-mode resonance grating filter, it is obvious that the feature size (Λ, FF) primarily determines the positions of the transmission peaks, and the effect of the period (Λ) is greater than the fill factor (FF). This is consistent with the scalability of transmission peaks with the grating feature. In addition, the quality of a-Si is also very important, because the refractive

63

index of a-Si together with FF affects the effective refractive index of the grating layer, which directly relates to the grating reflectivity and resonance minimum (see eq. (2.3.1) – eq. (2.3.3)) Therefore it is important to have a high-quality a-Si top modulated layer. From a fabrication point of view, the photolithography resolution and the grating etch are the key factors to precise wavelength detection in this technology.

Similar to the Fabry-Perot filter, for a guide-mode resonance grating filter, the angular dependence of the transmission peak is also investigated. An incident angle variation from 0° to 10° and the corresponding transmission peaks are plotted in Fig. 4.12.
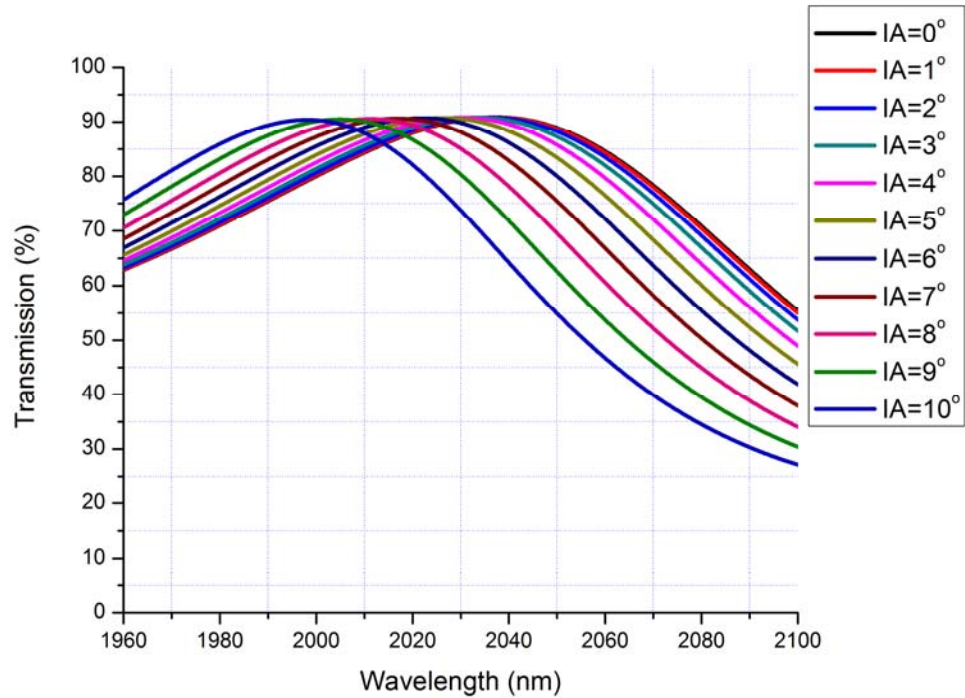
Fig. 4. 12 Transmission through the Guided-Mode Resonance Cavity filter at different incident angles (IAs) from 1 degree to 10 degrees

As can be seen from Fig. 4.12 that the transmission peak shifts to shorter wavelength as the angle of incidence increases. This can be explained by a change in the effective propagation constant when θ changes, which also causes the corresponding change of effective refractive

index [74]. When the incident angle is 4°, the peak shifts from 2040 nm to 2030 nm, indicating a 10 nm shift. However, due to the width and overlap showing between the lines, it is difficult to determine a finer accuracy level for the guided-mode resonance grating filter.

The temperature dependence of the transmission peak of a guided-mode resonance grating filter is simulated assuming a normal light incidence. The transmission spectrum for temperature varying from 100K to 500K is shown in Fig. 4.13.
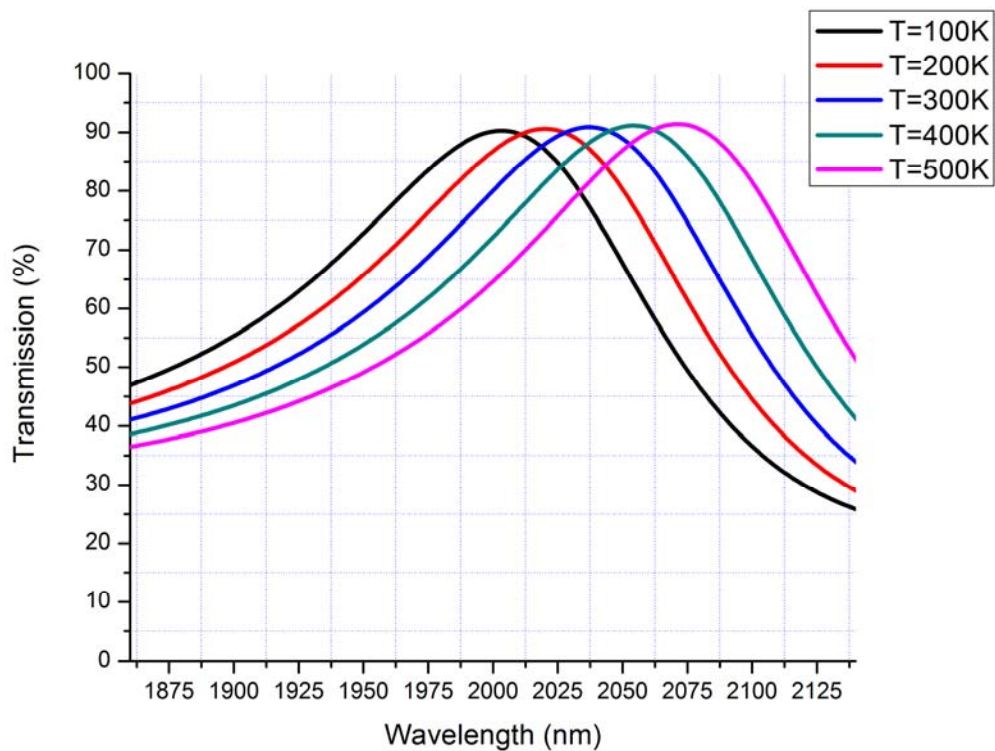
Fig. 4. 13 Transmission through the Guided-Mode Resonance Cavity filter at different temperatures from 100K to 500K

The transmission peak shifts to longer wavelengths as the operating temperature increases. This can be explained by a change in propagation constant of the waveguide grating and corresponding effective refractive index, caused by a change in permittivity as the refractive

index increases with temperature. It can be seen that when there is an increase of 100K of operating temperature, the wavelength shift is approximately 25 nm to a longer wavelength, much greater than the peak shift of the Fabry-Perot filter.

4.3   Summary and Comparison

Given the simulations and discussion above, a brief summary of the two approaches can be obtained, as shown in Table 4.6.

Table 4. 6 Summary of a comprehensive comparison between Fabry-Perot filters and guided-mode resonance grating filters

	Fabry-Perot Filter	Guided-Mode Resonance Grating Filter
Growth/ Fabrication	• Easy patterning • Lengthy film deposition and etch, especially for longer wavelengths detection	• Shorter film growth period • Patterning susceptible to photolithography resolution and etch, especially for shorter wavelengths detection
Transmission	• Sharper transmission lines, low sideband transmission • Transmission might be affected by the film quality • Less sensitive to changes in light incident angle and operating temperature	• Broader, asymmetric transmission lines, higher sideband transmission • Polarization • More sensitive to changes in light incident angle and operating temperature
Absorption	• Symmetric, sharper absorption peaks	• Asymmetric broader absorption peaks

From the comparison it can be seen that the multi-stack structure of the Fabry-Perot filter is able to provide much higher sideband reflectivity, thus sharp and high transmissions on the wavelengths of interest. It requires repetitive deposition of dielectrics, which sometimes can be hindered by the non-ideal deposition condition. The guided-mode resonance grating filter needs much less dielectric layers, so it is less susceptible to the adverse factors introduced during alternating layer growth, and the material deposition period is significantly shortened. However, from a fabrication perspective, the precision of grating feature patterning and the etch-depth of its surface a-Si layer are of the essence, which might also be challenging at shorter wavelengths due to small feature sizes and high patterning precision. From an operation point of view, the 1D grating filter is not able to provide sharp and symmetric transmission peaks in the wavelength regime in this study, and unlike the FP filter, its transmission is polarization sensitive.

The comparison of the ultimate absorption characteristics of the two multispectral wavelength detection suggests that besides the sharp transmission peaks of the filters, an active region with decent light absorption in the wavelength regimes of interest is also desired for the optimized detection performance. The Fabry-Perot resonant cavity filter has complicated film deposition and fabrication processes, but it's able to provide sharper peaks, lower sideband absorption, and lower temperature/incident angle dependence. The guided-mode resonance grating filter is polarization sensitive, requires less film growth and fabrication steps but it has high sideband transition which is prone to affect the peak signal, and the detection accuracy is more susceptible to changes in the operating temperature and incident angle dependence.

It should also be noted that, from a design/application point of view, it is flexible to change the detection wavelength to almost any value by simply varying the thicknesses or

materials of the dielectric layers in the FP filter using the same photolithography mask, which is advantageous to bring down the fabrication cost. For the grating case, this flexibility is limited.

Due to the performance limitations of the guided-mode resonance grating filter as discussed above, my study of the filtering technique will be focusing on the Fabry-Perot optical filters for wavelength detections in the NIR/SWIR regimes.

Chapter 5 Fabrication and Characterization of Fabry-Perot Multispectral Photodetectors

In this chapter, the fundamental working principles of the two major sputtering techniques – DC sputtering and RF sputtering are introduced for filter implementation. By using sputtering deposition, the SiO_2 and a-Si films are grown and they are characterized by using ellipsometry to identify the refractive indices and film thickness. Later on, the 8-layer Fabry-Perot filter structure is deposited and fabricated on photodetectors to form multiple filters with varying cavity lengths in order to detect different wavelengths. To take advantage of the photodetectors' high quantum efficiency in the NIR region, the main effort of this study is devoted into the fabrication and characterization of the Fabry-Perot filters capable of detecting four wavelengths between 1.1 to 1.8 μm. The experimental results show high transmission (from the reference samples), and external quantum efficiencies (from the integrated devices) that are comparable to theoretical predictions at the four wavelengths of interest.

Compared to many of the existing multispectral detection techniques in the NIR regime, my initial results have shown that by using Fabry-Perot optical filters for simultaneous multispectral wavelength detection, the absorption peaks have high intensities, and the FWHM (full width half maximum) of the detection peaks are much narrower than many of the current filtering technologies in the same wavelength regime [33], [95]. This offers the opportunity for more precise sensing/detection. Meanwhile, the filter materials, deposition method, and fabrication process used in this study have proven that by using low-cost amorphous materials and a common deposition and fabrication, post-growth multispectral wavelength detection with high precision can be achieved. Compared to prior art by Emadi, *etc.*, who proposed the

theoretical basis of the Fabry-Perot filters design and fabrication for imaging applications [65], [66], my study has realized not only the physical implementation of the filters and extended the application to the NIR regime, but also successfully integrated the filters with high-performance photodetectors to realize simultaneous multispectral wavelength detection.

5.1 Sputtering Deposition

5.1.1 Mechanism and deposition condition characterization

Sputtering [96]–[99] is a process whereby atoms are ejected from a sold target material by bombardment of the target with energetic particles. This requires that the kinetic energy of the incoming particles be much higher than the thermal energies. Therefore, sputtering deposition is a physical vapor deposition (PVD) method of thin film deposition technique. As mentioned in the definition of "sputtering", a sputtering deposition involves:

- Creating an ionic plasma by applying a high voltage to a glow tube

- Ions bombarding the target materials at the cathode

- Ejection of target atoms from the cathode by energy and momentum transfer

- Deposition of the sputtered atoms onto the substrates

To deposit different materials, both inert and reactive gas can be used as the sputtering gas, and the gas atomic weight should be close to the weight of the target atom for sufficient momentum transfer. For inert gases, the atoms are ionized and accelerated under high voltage before bombarding the target with high energy. Unlike reactive gases, inert gases do not react with the target or its ejected atoms. Ar is a widely used inert sputtering gas. Reactive gases such as O_2 and N_2 can be used to deposit oxide and nitride compounds. The principle is shown in Figure 5.1.
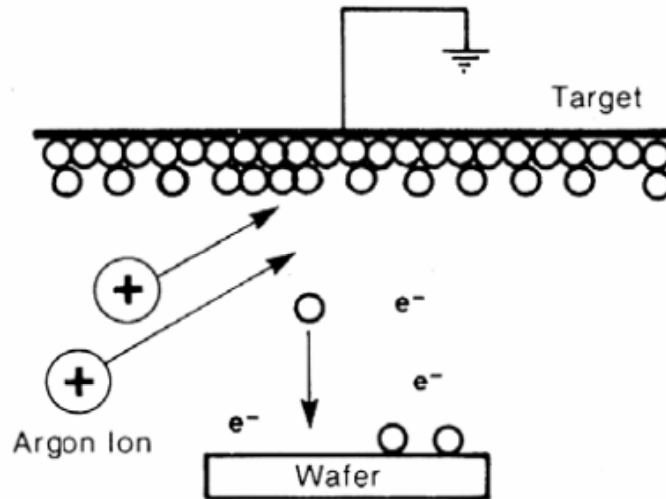
Fig. 5. 1 The principle of sputtering. This schematic is taken from Reference [99]**.**

The key sputtering parameters and their correlations include [97], [98]:

o *Sputtering gas pressure*. The deposition rate reaches its maximum as the gas pressure increases, and then decreases. This is caused by the compromise between the increasing number of gas ions and increased scattering of gas ions with neutral gas atoms/molecules.

o *Sputter voltage*. It can maximize the sputter yield due to its direct relationship to particle kinetic energy.

o *Deposition rate*. It mainly changes with gas pressure and increases with sputter yield (voltage). It has also been discovered that, the deposition rate increases with increasing temperature of the target. Therefore, thick targets are advisable for the long deposition times used in this study.

o Substrate bias. Putting negative bias on the substrate can significantly increase the bombardment energy of ions and thus increase the density of the film accordingly.

o *Substrate temperature*. Changes in the substrate temperature can be caused by the bombardment and controlled by heater. Normally, increasing the substrate temperature

71

can help the kinetic movement of the atoms on the surface and form more uniformed films.

o *Ejected particle energy*. The ejected particle energy increases with increasing sputter voltage, and decreases with increasing substrate bias and increasing gas pressure.

o *Mean free path*. The mean free path of atoms can be reduced by either increasing the chamber pressure or decreasing the chamber temperature. Normally, a mean free path greater than the chamber length is desired because it allows the beam to reach the target before getting scattered, which can provide good control over the energy and directionality of the incoming ions.

There are many types of sputtering procedures. Here we only introduce DC sputtering and RF sputtering, which are both used in the deposition of the Fabry-Perot filters studied in this work. Schematics of these procedures are shown in Figure 5.2.

(a)

(b)
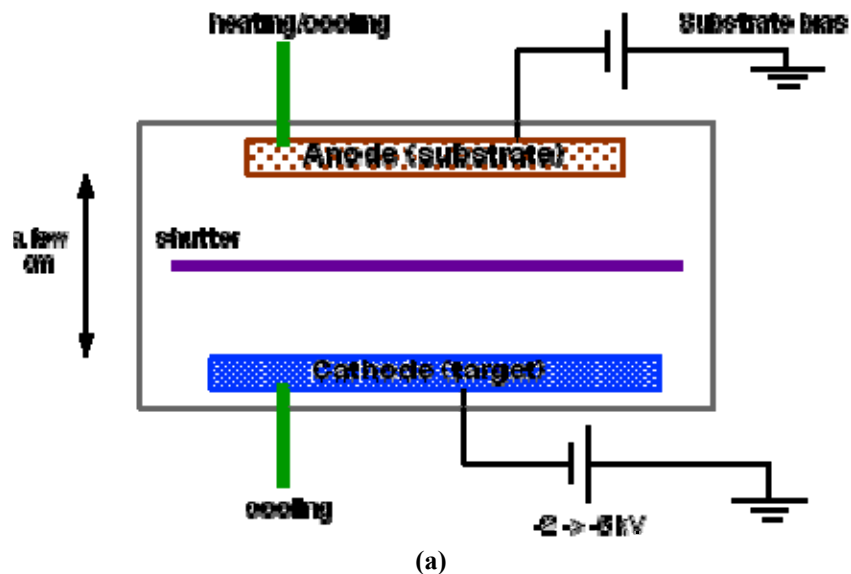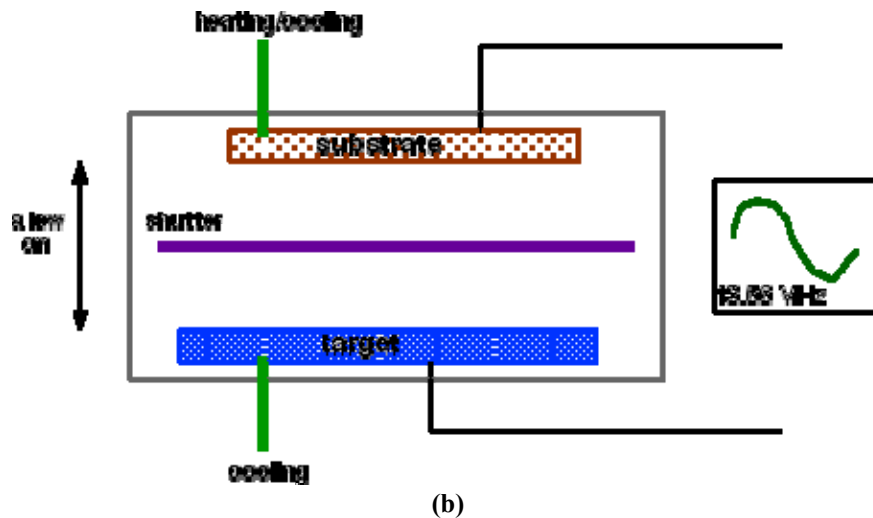
Fig. 5. 2 Schematics of (a) DC sputtering and (b) RF sputtering, taken from Reference [97]**.**

DC sputtering is the most commonly used sputtering technique. The mechanism is very simple. The sputtering utilizes an ionic plasma that is created by the high DC voltage to the glow tube. The energy of the ions is primarily controlled by the sputter voltage. However, DC sputtering can only work well on conductive targets/materials. The reason is that for targets with poor conductivity, positive charges build up on the cathode (target) and, as a result, an ion cloud caused by the accumulation of positive ions near the target forms between the plasma and the target during the sputtering process. This will adversely affect the bombardment of ions as well as neutral atoms. Therefore, high voltage up to 10^{12} volts is needed for sputtering insulators using DC sputtering, and high gas pressure is needed to sustain the plasma, which can be impractical for many sputtering systems [98].

For materials of low conductivity/insulators, RF (radio frequency) sputtering can be used for much better deposition. In a typical RF sputtering process, a frequency above 50 kHz is applied between the cathode (target) and substrate. Ions that are heavy are not able to follow the switching and only electrons can neutralize the positive charges that build up on the target. By

doing this, it is much easier to sustain the plasma under these conditions, and the sputtering process can be operated at lower gas pressure [97].

For this study, a DC source is used for sputtering deposition of a-Si using a silicon target, and a RF source is used for sputtering deposition of SiO_2 using a quartz target. Argon gas is used as the sputtering gas. Single layers of SiO_2 and a-Si are deposited and characterized to investigate the films quality.

5.1.2   Film quality of SiO_2 and a-Si

Different power and Ar pressure combinations are investigated to optimize the sputtering conditions for SiO_2 and a-Si deposition. A Kurt J Lesker CMS-18 four-target sputter is used for the DC sputtering of a-Si and RF sputtering of SiO_2 on c-Si substrates. The optimized deposition parameters for both materials are optimized and listed in Table 5.1:

Table 5. 1 Sputtering parameters for SiO_2 and a-Si depositions in Kurt J Lesker CMS-18   (No substrate heating, substrate voltage = 0 V)

Materials/Parameters	Deposition Type	Power (Watts)	Pressure (mTorr)
SiO_2	RF	350	10
a-Si	DC	350	2

A Horiba UVISEL Spectroscopic Ellipsometer is used to characterize the single film thickness and refractive index of both materials. For SiO_2, since there is no light absorption over the entire wavelength span of the ellipsometry measurement (400 nm – 850 nm), its film thickness and refractive index can be obtained directly by fitting the experimental results [88]. However, for a-Si, since there is a significant amount of light absorption below 850 nm [89], the film thickness is measured using a SEM (scanning electron microscope) and the refractive index is fitted based on the fixed layer thickness. For the films deposited in this study, the refractive

index for SiO_2 and a-Si beyond 850 nm are assumed to be 1.405 and 3.6, respectively. The values are slightly different from the typical values in this wavelength regime ($n(SiO_2) \approx 1.53$, $n(a-Si) \approx 3.4$) [88], [89]. Since the material properties are primarily determined by the deposition conditions [100], this deviation is not surprising. Based on a comparison between the typical values and the experimental results, it is reasonable to have a SiO_2 film with a refractive index that is 10% lower than the ideal value [92]. Similarly, the a-Si has an approximately 6% variation compared to the standard value. The possible reason for the deviations can be a combination of various factors such as pressure, substrate temperature, and target material [97]. It should be noted that the fitting results only represent the average value of the refractive index of the two materials, meaning that in reality the refractive indices might not be constant along the material deposition direction, which can be a contribution to the deviation of transmission peaks from their designed positions. The characterized refractive index of SiO_2 and a-Si are shown in Figure 5.3.

(a)   (b)
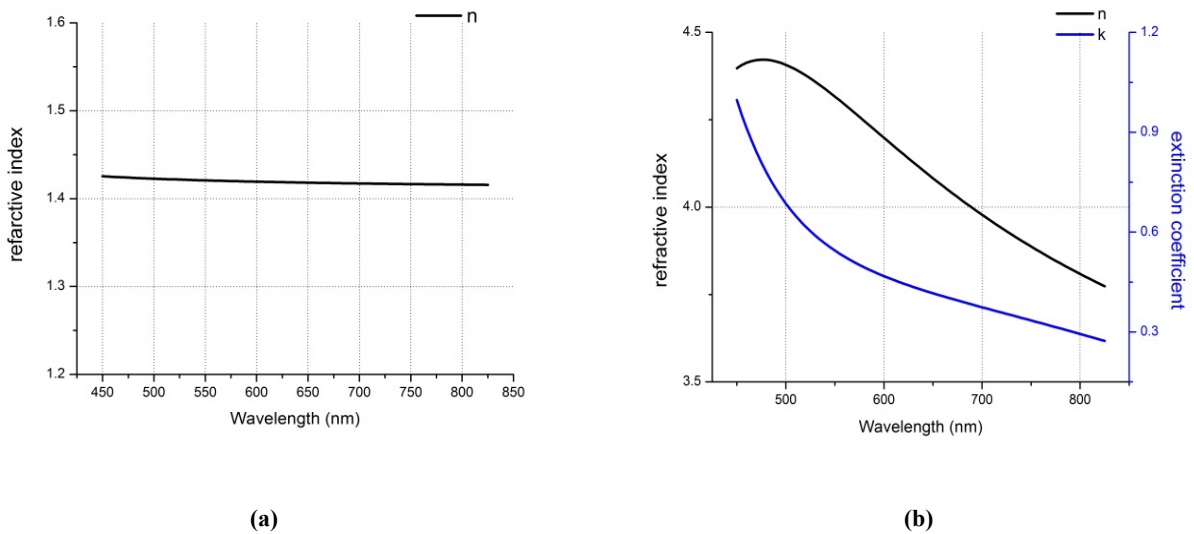
Fig. 5. 3 Graphs of (a) The refractive index of SiO_2 and, (b) The refractive index and extinction coefficient of a-Si

5.2 Multispectral Photodetectors for Wavelengths Detection Below 1.8 μm

5.2.1   Device fabrication

The SiO_2/a-Si filter layers (d_1- d_5), as shown in Figure 4.3 (a), were deposited on a photodetector chip and four InP substrates using a Kurt J Lesker CMS-18 sputter tool after detector fabrication. The SiO_2 and Si targets are purchased from the same vendor and have a thickness of ¼ inch each. The base pressure of the deposition was approximately 10^{-3} mTorr. SiO_2 was deposited using a RF source at 350 W and Ar pressure at 10 mTorr, and a-Si was deposited using a DC power of 350 W and Ar pressure of 2 mTorr, respectively. A Trion dry etch process (RIE/ICP=70/25 W, CF_4/O_2=50/5 Torr) was used consecutively to remove excess SiO_2 for resonant cavities of λ_1, λ_2, and λ_3 after photolithography. Samples were cleaned using O_2 plasma (200 W, 5 minutes) in a March PX-250 to eliminate photoresist residue on the etch surface. An Ar etch in the sputter reactor was also used to remove the contamination from the cavity top surface before the rest of the DBR layers ($d_6 - d_8$) were deposited. Figure 5.4 uses the thickest cavity (d_4) and a thinner cavity (d_3) as an example to illustrate the implementation process flow of the Fabry-Perot filters integrated with photodetectors: (a) photodetector fabrication, (b) bottom DBRs and thickest resonant cavity deposition, (c) cavity etch, (d) top DBRs deposition, and (e) removal of excessive filter layers. The final integrated devices capable of detecting four wavelengths below 1.8 μm simultaneously are shown in (f). Filters with other cavity lengths can be fabricated in the same way but with different etch times.
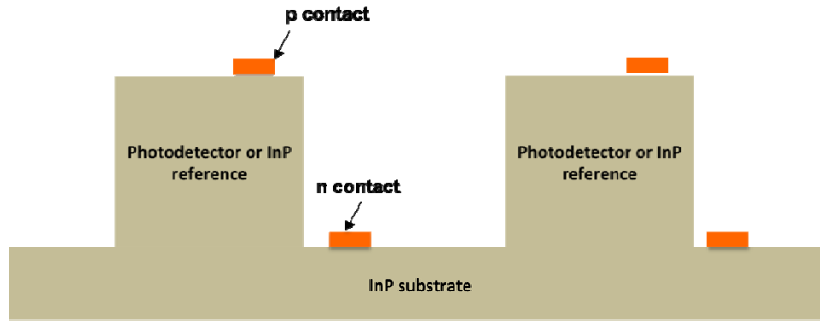
(a) Photodetector fabrication
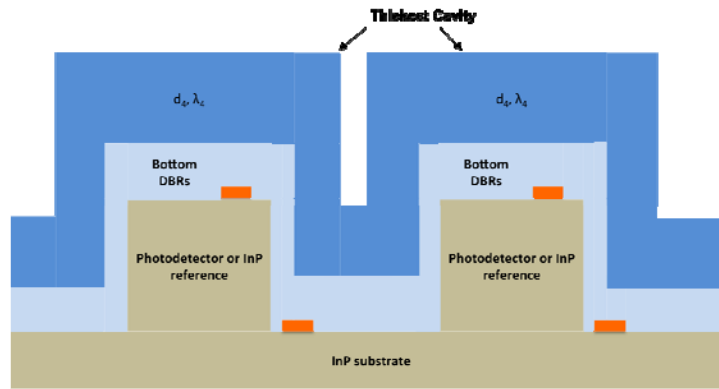
(b) Bottom DBRs and thickest resonant cavity deposition
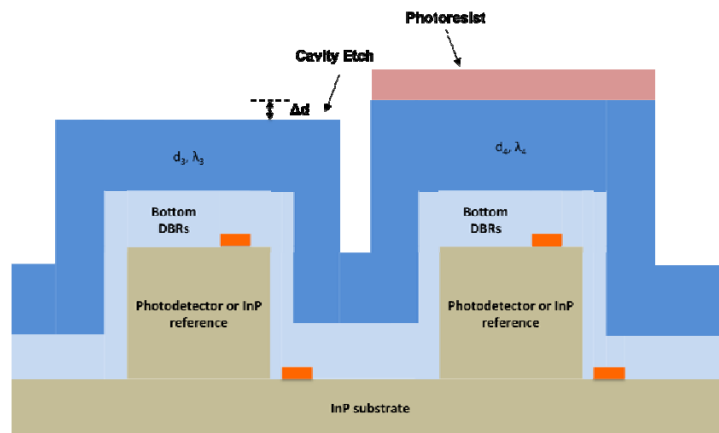
(c) Cavity/cavities etch
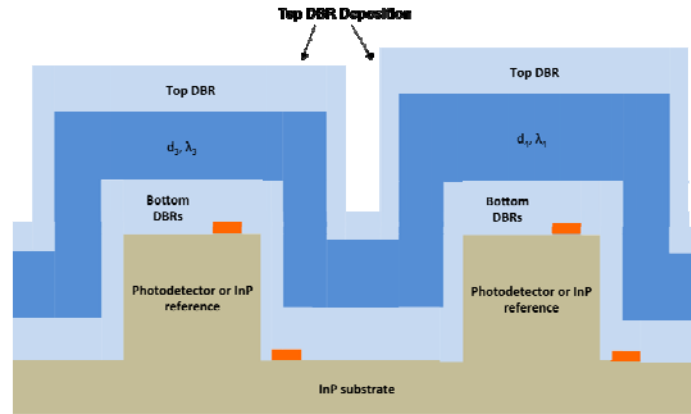
(d) Top DBRs deposition
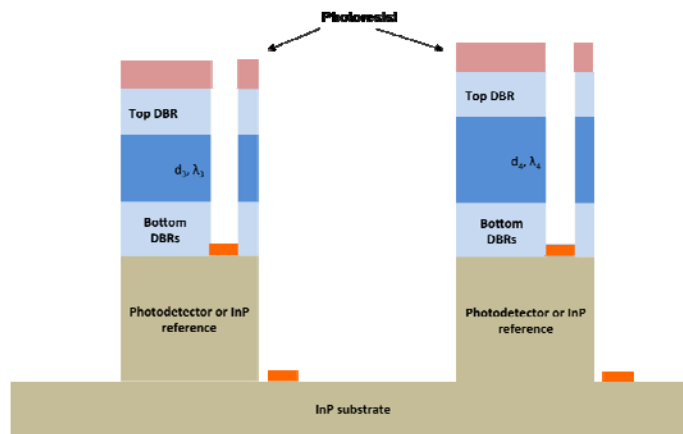
(e) Removal of excessive filter layers
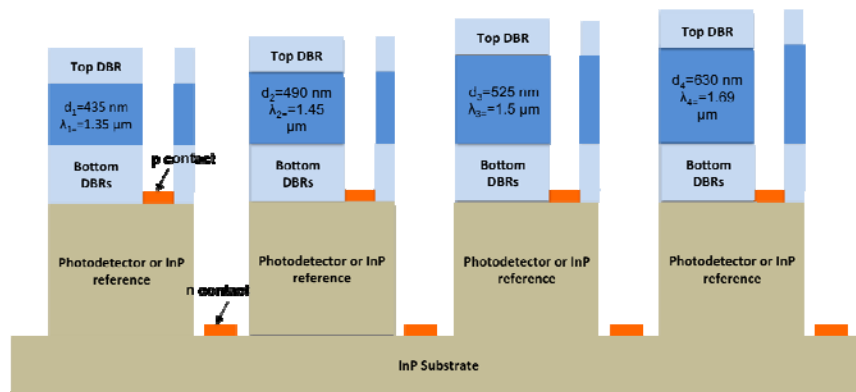
(f) Final integrated devices capable of simultaneous detection of four wavelengths below 1.8 µm

Fig. 5. 4 Schematic of process flow ((a)-(e)) and the final integrated devices (f) for simultaneously multispectral wavelength detection in the NIR regime

5.2.2 Characterization

a) Layer cross-section characteristics

A scanning electron microscope (SEM) was used to monitor layer thicknesses and interface quality, as shown in Figure 5.5. A silicon etch recipe of (RIE/ICP=300/150 W, SF_6=50 Torr) was sequentially combined with the SiO_2 etch (RIE/ICP=70/25 W, CF_4/O_2=50/5 Torr) to fully remove the excessive dielectric layers in the contact regions, and integrated devices with diameters of 500 μm, 350 μm, 250 μm, and 180 μm were fabricated. As can be seen, the actual thicknesses show good agreement with the design, except for the first SiO_2 layer (d_1); the image also exhibits smooth interfaces between adjacent layers. The reason for a thinner d_1 can be a lower target temperature at the beginning of deposition process, meaning a higher target resistance and smaller deposition current. An adjusted model (details shown in Table 5.2) is given for the further fitting of the optical and electrical characteristics of the devices to determine a more accurate set of parameters, i.e. refractive indices of SiO_2 and a-Si, and a more precise set of layer thicknesses.
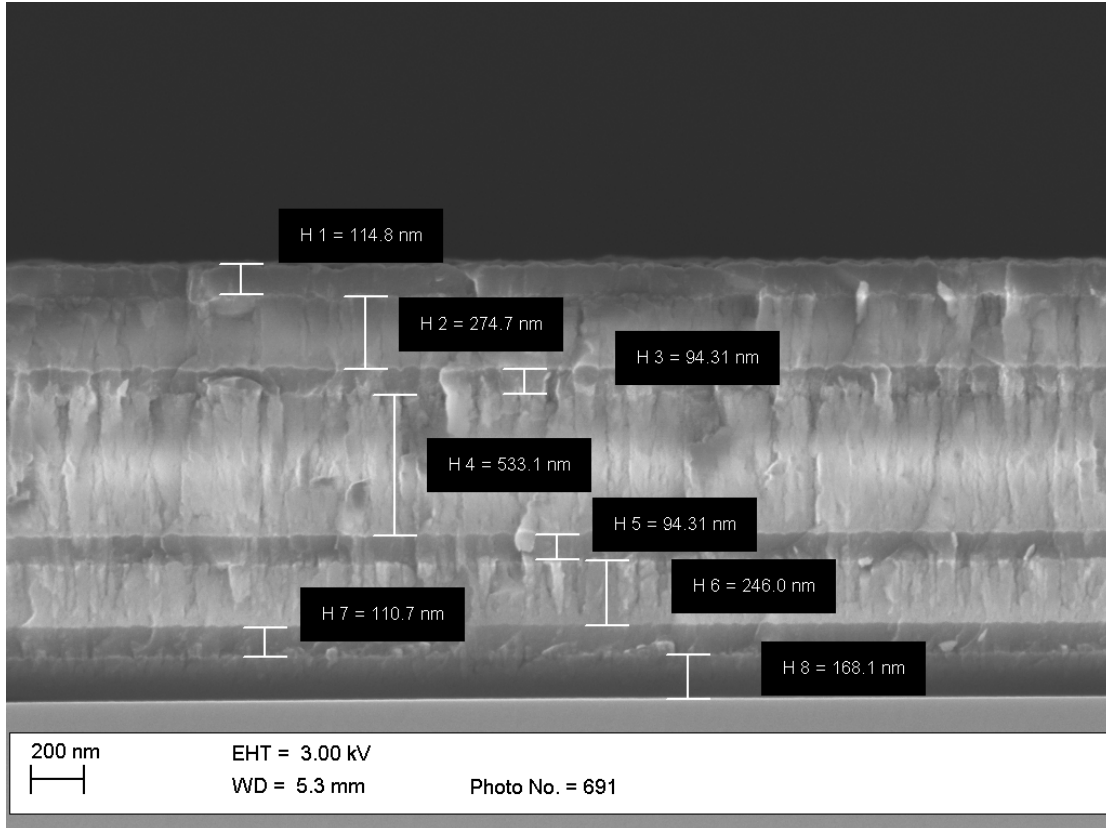
Fig. 5. 5 SEM cross-section image of the filter layers after deposition

Table 5. 2 Designed, experimental, and adjusted structure parameters of the FP optical filters for wavelength detection below 1.8 μm

Parameters	Design	Experimental (Approx.)	Adjusted
d_1	260 nm	165-180 nm	170 nm
d_2	110 nm	110 nm	110 nm
d_3	260 nm	255-260 nm	260 nm
d_4	110 nm	110 nm	110 nm
d_5	435 nm (λ_1)	430 nm (λ_1)	432 nm (λ_1)
	490 nm (λ_2)	500 nm (λ_2)	486 nm (λ_2)
	525 nm (λ_3)	540 nm (λ_3)	532 nm (λ_3)
	630 nm (λ_4)	630 nm (λ_4)	633 nm (λ_4)
d_6	110 nm	103-110 nm	110 nm
d_7	260 nm	250-255 nm	250 nm
d_8	110 nm	115-125 nm	116 nm
n(a-Si)	3.6	~3.6	3.58
n(SiO_2)	1.405	<1.405	1.38

b) Current-voltage characteristics

The average dark current-voltage (I-V) characteristics of five photodetectors with and without filters are shown in Figure 5.6. The dark current is approximately ~2 x10^{-2} A/cm^2 at

80

reverse bias of 10 V, which is consistent with our previous publications on photodiodes with 100 pairs of type-II 7 nm InGaAs/ 5 nm GaAsSb quantum wells as absorption regions [14], [56], [84]. The dark current after the filter deposition exhibit little change compared to before the filter deposition, indicating little damage has been introduced to the detectors during the deposition and etch process.
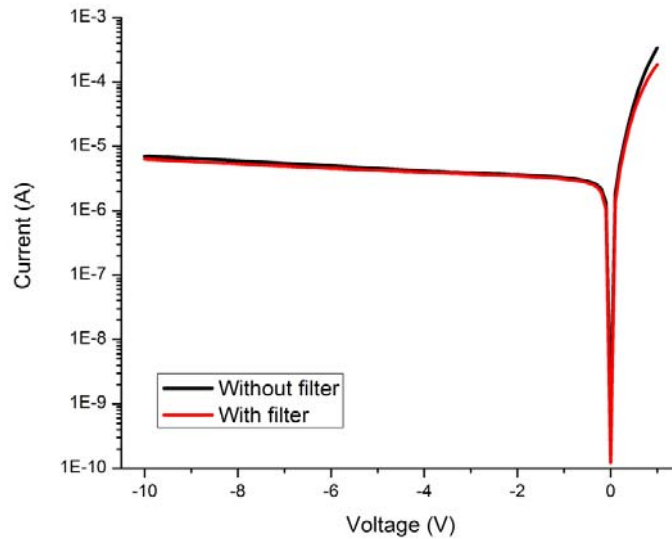
Fig. 5. 6 The average I-V characteristics of five photodetectors before/after filters were implemented

c) Transmission characteristics

The transmission peaks on the InP reference samples are at 1.25 μm, 1.35 μm, 1.46 μm, and 1.59 μm, which differ from the design (1.35 μm, 1.45 μm, 1.50 μm, 1.69 μm). The main reason is the non-uniformity of the sputtering deposition process, especially the thinner cavity thicknesses of 3% to 7%, leading to peak shifts to shorter wavelengths. The peak shifts match the predictions in Chapter 4 (Table 4.3) very well. A discrepancy in peak intensities from design,

which was due to normal experimental variations such as surface/interface roughness and measurement error, was also observed.

To adjust these differences and thus optimize the fitting for the experimental results, RSoft simulation was used to best fit the peak properties by using an average experimental layer thickness for each layer is based on the SEM images along with the following refractive indices: (SiO$_2$)=1.38 and n(a-Si)=3.58. The fitting parameters are shown in Table 5.2. By applying the adjusted fitting parameters, the best fit for the peak positions was obtained and the results are shown in Figure 5.7. A more in-depth analysis will be discussed together in conjunction with the external quantum efficiency characteristics in the next section.
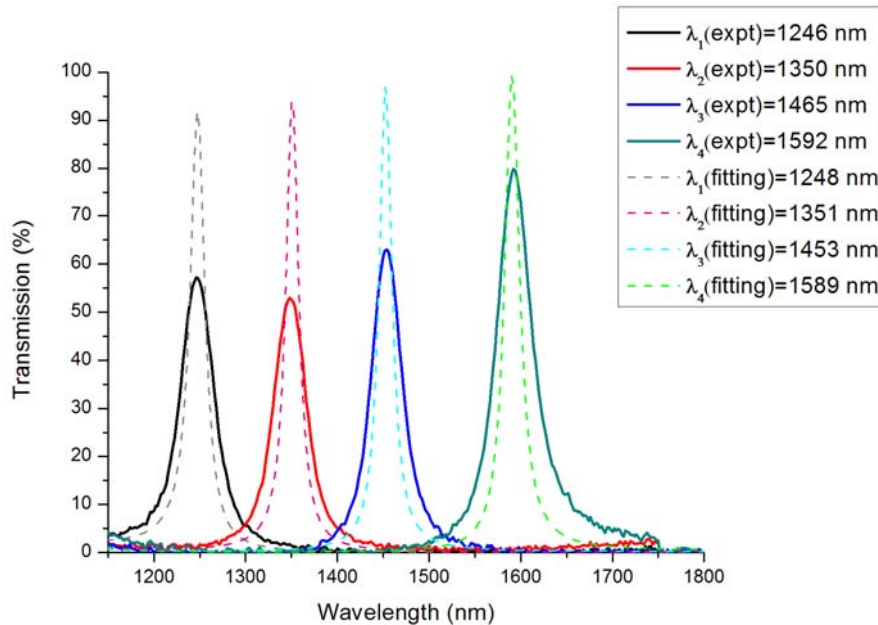
Fig. 5. 7 The transmission characteristics of FP filters integrated on InP substrates with experimental measured peaks ($\lambda_1 - \lambda_4$) at 1246 nm, 1350 nm, 1465 nm, and 1592, and the corresponding fitted peaks at 1248 nm, 1351 nm, 1453 nm, and 1589 nm)

d) External quantum efficiency characteristics

The external quantum efficiency peaks are at 1.32 μm, 1.41 μm, 1.49 μm, and 1.66 μm, which agree well with the design (1.35 μm, 1.45 μm, 1.50 μm, 1.69 μm), as shown in Figure 5.8. Compared to the transmission characteristics, the external quantum efficiency characteristics not only reflect the filter material properties such as the surface roughness and the cavity thickness, but also the electrical properties of the photodetector. Therefore, a more thorough analysis of the experimental results is needed to better understand the factors that can affect the external quantum efficiency at the wavelengths of interest.
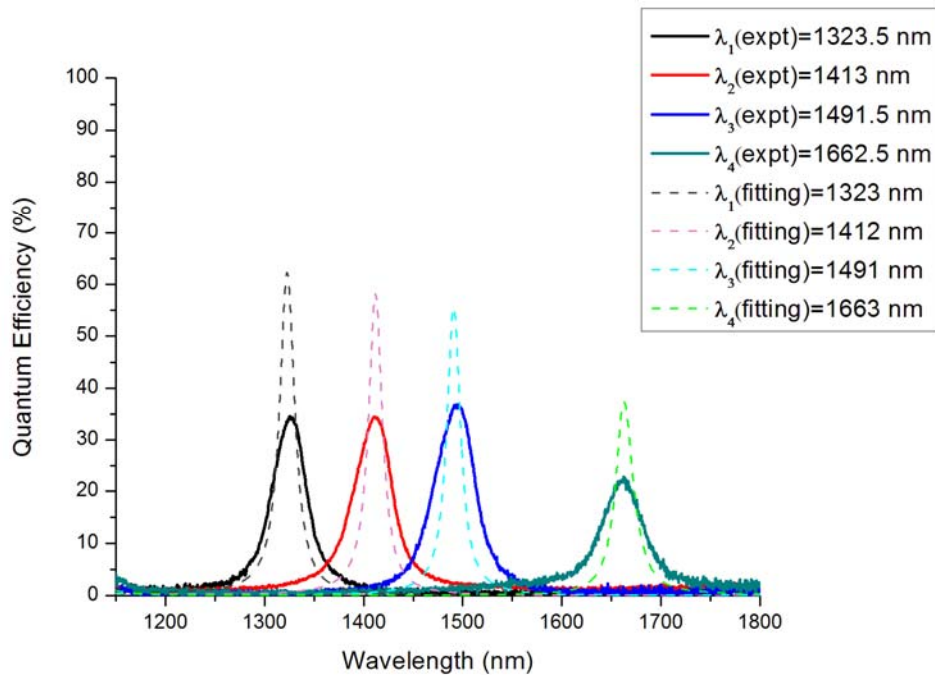
Fig. 5. 8 The external quantum efficiency characteristics of FP filters integrated on photodetectors with experimental measured peaks (λ1 – λ4) at 1323.5 nm, 1413 nm, 1491.5 nm, and 1662.5 nm, and the corresponding fitted peaks 1323 nm, 1412 nm, 1491 nm, and 1663 nm)

Two relative criteria are defined and analyzed to understand the correlation between the fabrication process and experimental results. A comparison of the absorption/transmission characteristics between the integrated filter devices and the reference samples is summarized in Table 5.3.

$$r(T) = \frac{\text{Intensity (experimental QE or transmission)}}{\text{Intensity (adjusted absorption or transmission)}}$$

$$r(F) = \frac{\text{Experimental FWHM}}{\text{Adjusted FWHM}}$$

Table 5. 3 Comparison of experimental v.s. adjusted results

Parameters	Trans. or QE (%) (expt./adj.)	FWHM (nm) (expt./adj.)	r(T)	r(F)
λ_1 (Ref Sample)	57.2/91.8	43/19.5	0.62	2.26
λ_2 (Ref Sample)	54.3/94.9	41.5/17	0.57	2.44
λ_3 (Ref Sample)	63/97.5	40/18	0.65	2.35
λ_4 (Ref Sample)	79/99.3	46/20	0.80	2.19
λ_1 (Detector)	33.6/65	41.5/17.5	0.52	2.37
λ_2 (Detector)	34.3/58.3	45.5/16.5	0.59	2.75
λ_3 (Detector)	36.7/55.6	48/16.5	0.66	2.90
λ_4 (Detector)	22.8/37.4	47/21.5	0.61	2.18

The actual transmission intensity at λ_4 (InP) reaches 79%, highest among all wavelengths, which indicates possible intensity loss caused by rough interface during dry etch. The r(T) values of all three wavelengths show comparable transmission intensities from the etched resonant cavities. The r(T) for detectors exhibit a similar trend except for λ_4. Possible explanations for a lower r(T) for λ_4 (detector) are (1) a MWQ carrier collection efficiency ≤ 1 at longer wavelengths

affected by non-uniform mesa depths and the n-InGaAs layers, (2) light scattering at rough air/a-Si incident surface, caused by the fabrication/cleaning process, (3) reflectivity measurement error at longer NIR wavelengths, (4) non-uniform light absorption across the wafer due to variations in the material growth.

Smaller r(F)s at λ_4 for both integrated devices and the InP references indicate less roughness at the un-etched cavity/a-Si interfaces. Larger r(F)s from the devices are assumed to be due to light scattering on the rough incident surfaces caused possibly by damage during plasma cleaning. The trend of increasing r(F)s as peak wavelength decreases in each data set might be a direct correlation between etch depth and cavity surface roughness.

5.2.3   Summary

From the above observations and comparison of the post-growth multispectral Fabry-Perot integrated filter devices, it can be seen that the experimental results match the theoretical predictions fairly well, giving us guidelines on wavelength tuning to shorter or longer wavelengths of interest. To summarize, the process of making a Fabry-Perot integrated filter device chip includes the following three aspects.

- Design. This part comprises the light diffraction calculation of the independent Fabry-Perot filters and combining the diffraction properties with the light absorption property of the photodetectors to generate the final light absorption spectrum of each integrated device. The key parameters that determine the transmission/absorption peak position of an integrated device are:
    o The thicknesses of the DBR quarter-wave layers
    o The length of the resonant cavity

o The refractive indices of the materials that compose the DBRs and the resonant cavity, particularly SiO_2 and a-Si in this case

The above three factors can determine the wavelength detected by one integrated device. However, the refractive index of the top layer of the photodetector should also be taken into account as a factor that determines the DBR layer thicknesses. The light absorption characteristics of the photodetector only determine the absorption intensity at this wavelength.

- Fabrication. The process of making an integrated device chip includes the fabrication of the photodetector chip, deposition of the bottom DBRs and the Fabry-Perot cavity layer, cavity etch, deposition of the top the DBRs, and removal of the excess dielectric portion for electrical measurements. Since the photodetector fabrication process has been well established, the effort mainly focuses on the deposition and fabrication of the filter coating. A multiple target sputter system is used for the dielectric deposition under high vacuum. Argon is used as the sputtering gas and no extra heating or voltage is imposed on the substrate. The deposited materials exhibit good mechanical and optical properties, and no significant stress on the adjacent interfaces is observed for the thickest cavity layer (up to 630 nm). An ICP/RIE dry etch is used to remove excess cavity thicknesses and DBR layers to expose the contact regions, and the etching process is monitored in an SEM to ensure the correct etching depths. To protect the filter regions from being damaged by etching, a thick photoresist layer (AZ4620) has been used as the etch mask. The remaining photoresist can be removed by cleaning in the oxygen plasma. It is worth noting that due to the reaction between the photoresist and the fluorine (CF_4/SF_6) gas, a hard layer of substance will be formed on the photoresist surface during the etching process [101], [102], and it is proved to be very difficult to completely remove by using

oxygen plasma and Aceton rinse. However, in this case the small amount of residue does not affect the QE characterization.

- Characterization. In this step, the current-voltage characteristics, the cross-sections, and the external quantum efficiency characteristics are studied to understand the integrated device properties.

  o The room-temperature dark current-voltage characteristics after filter integration show little difference from the I-V results before filter integration, indicating negligible damage has been introduced to the integrated devices during the sputtering/filter fabrication process.

  o The filter layer thicknesses, cross-sections, and interface qualities are monitored in an SEM. The images show smooth SiO_2/a-Si interfaces in regions without dry etch, and less smooth SiO_2/a-Si interfaces in regions with a cavity dry etch. This may be the source of peak broadening and diffractive loss in the quantum efficiency measurements.

  o The experimental external quantum efficiencies show successful detection of four wavelengths as designed and good agreement in peak positions and intensities from the design, an indication of experimental parameter variations. RSoft DiffractMOD is used to fit the experimental external quantum efficiencies using the layer thickness information gathered from SEM imaging. By adjusting the thicknesses and refractive indices in the simulator, a set of optimized key parameters (e.g. filter material refractive indices and layer thicknesses) is obtained. Further analysis of the quantum efficiency characteristics of the integrated devices and the transmission characteristics of the reference (InP) samples indicate the

surface/interface roughness, reflectivity measurement error, and carrier collection efficiency can also be responsible for the deviation in the external quantum efficiency peak positions and intensities. It is worth mentioning that the etch product from the photoresist-fluorine reaction does not seem to affect the characterization process significantly. The reason is that the light spot is collimated and focused on the device with a diameter of ~20 μm, making it easier to adjust and move to a clear surface for photoresponse measurement.

5.3   Conclusion

In this chapter, a complete fabrication and characterization process for the integrated photodetectors for multispectral light detection has been presented and discussed. The Fabry-Perot integrated optical filter has proved to be able to simultaneously sense four different wavelength peaks in the 1.1-1.8 μm regime (1.32 μm, 1.41 μm, 1.49 μm, and 1.66 μm) with acceptable dark current, sharp peaks, and reasonably high external quantum efficiencies at room temperature, making it a promising candidate for post-growth multispectral wavelength detection.

Chapter 6 Extensive Work, Conclusion, and Future Work

In this chapter, a conclusion of the current work is summarized. Later, multispectral detection for wavelengths beyond 1.8 μm is designed and implemented to further exploit the application of Fabry-Perot filters with thicker stack thicknesses. The problems and challenges existing in current design/fabrication process are analyzed based on the experimental results. Lastly, potential improvements for the current problems in the simultaneous multispectral wavelength detection at longer wavelengths will be proposed for future work.

6.1 Conclusion

The objective of this dissertation is to exploit the property and the advantages of the post-growth wavelength detection and wavelength tuning method by using Fabry-Perot optical filters integrated with InP-based InGaAs/GaAsSb type-II quantum wells photodetectors in order to achieve simultaneous multispectral wavelength detection in the NIR and SWIR regimes at room temperature. The photodetectors used to integrate with the optical filters are the InP-based InGaAs/GaAsSb type-II MQW photodiodes for the high quantum efficiency in the NIR regime and acceptable quantum efficiency beyond 1.8 μm at room temperature, with moderate dark current [14], [84]. The experimental results for wavelength below 1.8 μm have proved that this method is promising for simultaneous multispectral wavelength detection with sharp absorption peaks, reasonably high quantum efficiencies, low/zero sideband absorption, and acceptable dark current. This design and fabrication of the integrated devices show high flexibility in wavelength tuning and the potential to detect several wavelengths at the same time. No similar results have

been reported so far to our best knowledge. Compared to previous design by Emadi, *etc.*, my study has realized:

- The physical implementation of the filters and extended the application to the NIR regime;

- Integrating the filters with high-performance photodetectors to realize high performance simultaneous multispectral wavelength detection.

Specifically, it has been shown that this method is capable of simultaneous detection of 1.32 μm, 1.41 μm, 1.49 μm, and 1.66 μm with quantum efficiencies up to more than 37.4% and almost zero sideband light absorption. The peaks have approximately 40 nm FWHM, which increases as the etching time increases. The thickness and film quality of each layer can be effectively controlled by the sputtering parameters (e.g. the Ar pressure, the gas flow, and the sputtering power). The adjacent SiO_2 and a-Si layers exhibit smooth interfaces and good quality according to SEM imaging and single layer characterization. The dark current after filter implementation does not change significantly compared to a photodetector without filter, which indicates little damage has been introduced to the photodetector sidewall. A thin film of etch product formed form the reaction between the photoresist (etch mask) and the SF_6/CF_4 is found on the light incident surface, but it does not affect the light filtering process at this point.

It should also be noted that, based on the cavity defining method (dry recess etch) and etch rate, approximately 15-20 wavelengths (peaks) can be detected in the 1.1-1.8 μm range by using time-controlled dry etch on the SiO_2 cavity. Additionally, based on the sensitivity analysis, for higher spectral accuracy, it is ideal to have the incident light with an incident angle of close to 90°, which suggests that, for many remote sensing applications, the photodetector array is

preferred to be installed far away from the object to ensure the deviation from normal incidence is negligible.

.

6.2   Multispectral Photodetectors for Wavelength Detection Beyond 1.8 µm

To further investigate the potential of using Fabry-Perot filters for detection at longer wavelengths, filters with the same structure but of different layer thicknesses were also fabricated and characterized for four wavelengths beyond 1.8 µm. Although the initial external quantum efficiencies measured at the four wavelengths are not prominent due to limitations in the current fabrication and measurement, the transmission characteristics in this regime show promising trend and the existing problems provide helpful feedback for future work.

6.2.1   Device fabrication

The fabrication process for the integrated devices for detection beyond 1.8 µm follows the same process flow described in section 5.2.1, only with different DBR thicknesses (SiO_2/a-Si, 360 nm/150 nm) and cavity lengths (1350 nm, 1450 nm, 1550 nm, and 1650 nm) for SWIR wavelength detection at 2 µm, 2.1 µm, 2.2 µm, and 2.31 µm. It should be noted that for this batch of devices, all four cavities underwent significant amount of dry etching to obtain the desired thickness. Figure 6.1 is a schematic of the final integrated devices capable of simultaneously detecting four wavelengths in the SWIR regime based on the design in Chapter 4.
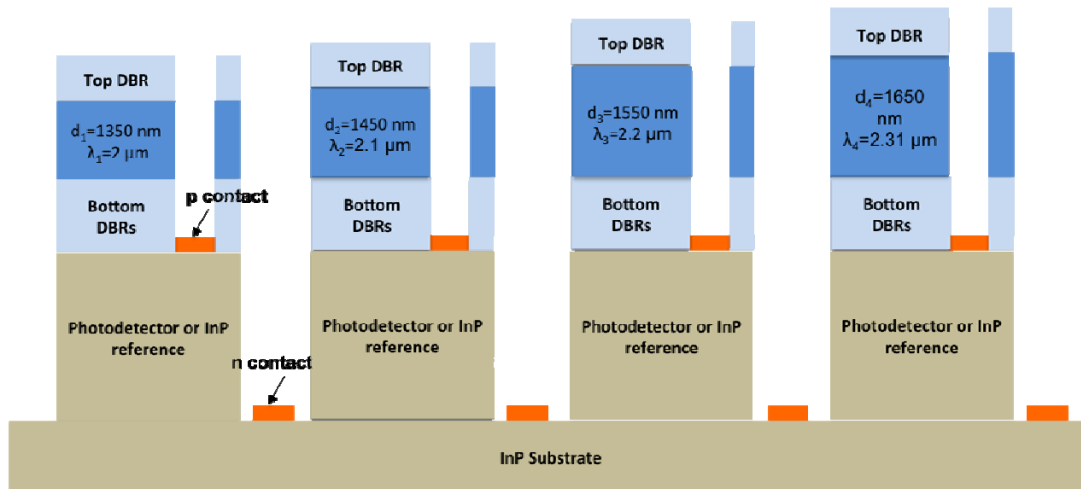
Fig. 6. 1 Schematic of the final integrated devices for simultaneously multiple wavelength detection in SWIR regime

To be measured in the FTIR setup, the integrated devices are mounted on TO headers and wire bonded for testing. Since the resonant cavity lengths and DBR layer thicknesses are considerably thicker than those discussed in the preceding chapters, a few observations are worth mentioning:

- Thick dielectric layers peel off from the n metal surface. The cause is likely to be high stress associated with the thick dielectric layers. This was first observed during the photolithography development process before cavity etch and continued when the photoresist was being rinsed off after the cavity etch. The big dielectric pieces that peeled off the metal also removed the deposited coatings from the small devices in adjacent areas. Only devices with large diameters such as 500 μm, 350 μm, and very few 180 μm devices were able to survive for characterizations. In the subsequent contact window etch step, a significant amount of Au n-type contact was etched away due to the fact that the

dielectric coatings to be etched were already removed, which left no protection for the metal.

- Faster than usual SiO_2 etching rate due to inferior SiO_2 quality. A much faster SiO_2 etch rate (60 -80 nm/minute) was observed during the cavity etch step when using the same dry etch recipe (RIE/ICP=70/25 W, CF_4/O_2=50/5 Torr), and it was almost twice the normal etch rate (30 − 40 nm/minute). The explanation for such phenomenon is the deteriorated SiO_2 cavity layers caused by the long sputtering deposition. The long deposition time is also likely to cause a gradient in the SiO_2 refractive index profile and the average refractive index of be lower than expected.

- Much thicker and uneven photoresist etch residue left on the light incident surface, caused by long dry etching time. To protect the filter layers from the dry etch process while removing the excess dielectric layers on top of the p-contact, a thick photoresist (AZ 4620, thickness = 6-7 μm) was used as the etch mask. The photoresist was post-baked at 130 ^{o}C for 5 minutes until it hardened and was put in Trion for consecutive etch. However, a single layer of AZ 4620 was too thin to withstand the long etch time required for the removal of the thick dielectric layers, and therefore one more layer of AZ 4620 was spun on for the complete removal of dielectric layers from the contact. A rough thickness of 5 μm of photoresist etch residue was left on the light incident surface after the etch process. It is worth noting that a hard layer of reaction product has formed from the chemical reaction between SF_6/CF_4 and AZ 4620 during the dry etch process, and this substance is extremely hard to remove completely. Overnight cleaning (> 24 hours) in oxygen plasma (power=200W, O_2=80 Torr) was able to remove a large portion of the

etch product, but this left a rough surface with roughness and a significant amount of un-

cleaned residue, and possible damage to the DBR layers, as shown in Figure 6.2.

6.2.2 Characterization

Due to damage to the devices with smaller diameters, only devices with Diameter=500

µm are bonded for characterizations.

a) Cross-section characteristics
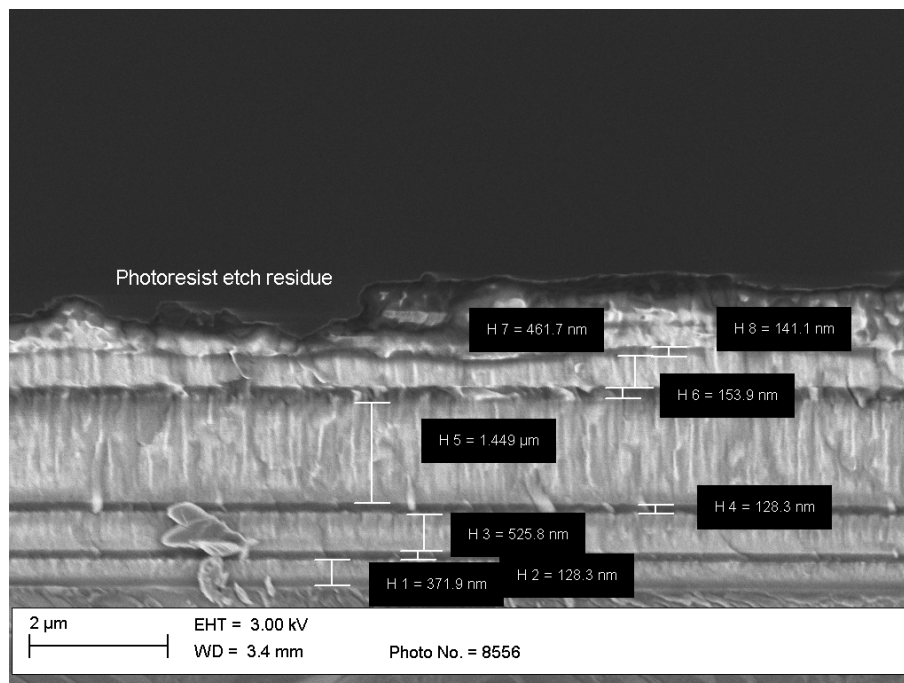
Fig. 6. 2 A cross-section SEM image of the Fabry-Perot filter after fabrication

The layer thicknesses of the integrated photodetectors and integrated InP substrates have

been characterized in the SEM, and a thickness variation of $\sim \pm 10\%$ has been observed in the

lengths of the cavity layers, indicating considerable thickness non-uniformity during longer

sputtering deposition. A layer of photoresist etch product is seen covering most part of the mesa

surface, and the thickness varies from approximately 200 nm to close to 800 nm after overnight cleaning.

Three cross-sections are monitored for the integrated devices at each wavelength, and an average thickness profile is used to represent rough thickness of the integrated photodetectors for four wavelengths, as shown in Table 6.1. This data will be used for the fitting of the experimental transmission characteristics in the next section.

Table 6. 1 Designed, experimental, and adjusted structure parameters of the FP optical filters for wavelength detection beyond 1.8 μm

Parameters	Design	Experimental (Approx.)	Adjusted
d_1	360 nm	350-360 nm	350 nm
d_2	150 nm	130-140 nm	140 nm
d_3	360 nm	490-520 nm	510 nm
d_4	150 nm	150 nm	150 nm
d_5	1350 nm (λ_1)	1340 nm (λ_1)	1340 nm (λ_1)
	1450 nm (λ_2)	1450 nm (λ_2)	1450 nm (λ_2)
	1550 nm (λ_3)	1580 nm (λ_3)	1580 nm (λ_3)
	1650 nm (λ_4)	1640 nm (λ_4)	1640 nm (λ_4)
d_6	150 nm	140-160 nm	160 nm
d_7	360 nm	350 nm	350 nm
d_8	150 nm	135-150 nm	150 nm
n(a-Si)	3.58	~3.58	3.58
n(SiO$_2$)	1.38	<1.38	1.38

b) Current-voltage characteristics

The average dark current-voltage (I-V) characteristics of three types of photodetectors: 1) no filter, not bonded, 2) with filter, not bonded, and 3) with filter, bonded, are shown in Figure 6.3. Three devices of each type were measured. Prior to wire bonding, the dark current density was approximately $\sim 4\times 10^{-2}$ A/cm^2 at reverse bias of 10 V, consistent with previous result of integrated photodetectors at shorter wavelengths. However, the dark current density rose up to $\sim 1.5\times 10^{-1}$ A/cm^2, approximately 2.75 times higher than before wire bonding. This suggests

possible damage in the contact (p) region caused during wire bonding, and it might be a result of thinner contacts (p and n metal contacts) after the dry etch.
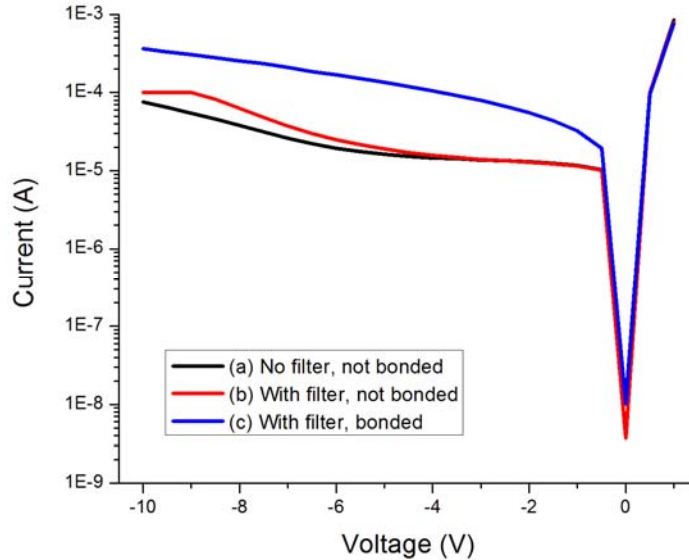
Fig. 6. 3 The I-V characteristics of photodetectors before/after wire bonding to the TO header

c) Transmission characteristics

The transmission peaks on InP reference samples were at 1.94 μm, 2.06 μm, 2.19 μm, and 2.25 μm, showing good agreement with the design (2.0 μm, 2.1 μm, 2.2 μm, 2.31 μm). Similar to the integrated photodetectors for shorter wavelengths, the main reason for the deviation is the non-uniformity of the sputtered cavity layers, leading to shifts in the peaks. A great discrepancy in peak intensities from design, compared to the integrated devices at shorter wavelengths, was observed. Based on our previous analysis on the fabrication process, it is reasonable to believe that light scattering at a much rougher cavity upper interface caused by dry etching is the main reason for the intensity loss.

To adjust for the difference and thus optimize the fitting for the experimental results, RSoft simulation was used to fit the transmission peak properties by using the average experimental layer thickness for each layer obtained from the SEM imaging, along with the following refractive indices: (SiO_2)=1.38 and n(a-Si)=3.58 (Table 6.1). By applying the adjusted fitting parameters, my best fit for the transmission peak positions was obtained and is shown in Figure 6.4. As a result of the interface roughness, the peaks FWHMs are ~ 2.5 times the widths of the fitting results, which are slightly higher than the reference results for shorter wavelengths discussed in previous chapters. A more in-depth analysis will be discussed together with the external quantum efficiency characteristics in the next section.
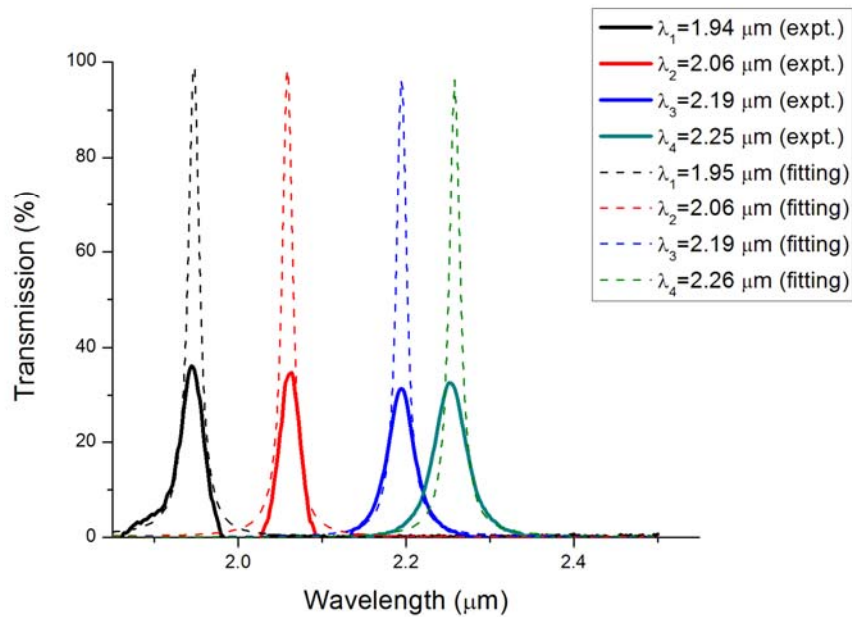
Fig. 6. 4 The experimental and fitted transmission peaks measured on integrated InP substrate at λ_1=1.94 µm, λ_2=2.06 µm, λ_3=2.19 µm, and λ_4=2.26 µm.

d) External quantum efficiency characteristics

The quantum efficiency characteristics beyond 2 µm are measured in the FTIR setup as previously discussed. To minimize the noise during measurement, the devices are biased under a reverse bias of 0.2 V at room temperature. The experimental spectra are shown in Figure 6.5.
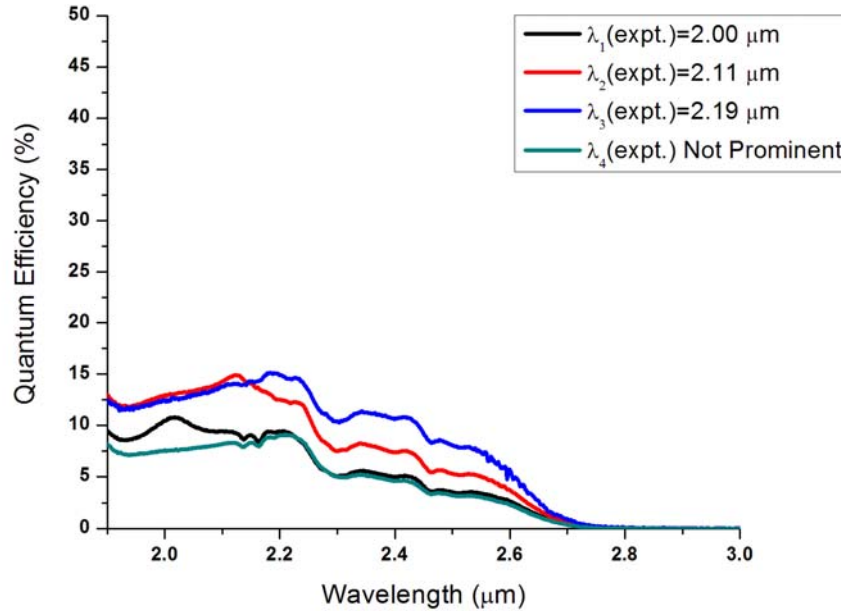
Fig. 6. 5 External quantum efficiency of the integrated photodetectorss at four wavelengths measured from FTIR

It can be seen that peaks of λ_1 (~2 µm), λ_2 (~2.11 µm), and λ_3 (~2.19 µm) are close to the design at 2 µm, 2.1 µm and 2.2 µm, but with low and ambiguous intensity trends. The peak at λ_4 does not show any prominent trend at its design wavelength at 2.31 µm. All the peaks exhibit large width and the sideband absorption intensities do not fall to zero in the range of $2 - 2.8$ µm. Possible explanation for the low quantum efficiency and non-zero sideband quantum efficiency can be the roughness and photoresist etch product on the light incident surface. As shown before,

the surface is significantly covered with etch residue formed in the chemical reaction between the photoresist and SF_6/CF_4, and the complete removal of this layer has not been successful using the existing cleaning methods. The thickness of the etch product varies from approximately 200 nm to 800 nm, with an unknown refractive index (n(AZ 4620)=1.69 at 435 nm [103]), causing possible arbitrary light diffraction. There is also a possibility of surface damage caused during the oxygen plasma cleaning process, leaving damaged DBR structures and unanticipated light diffraction. Since the photoresponse measurement using the FTIR relies on the calculation of light intensity on the device area, it is very difficult to obtain a clear trend of the light absorption profile for a structure that has a top layer with an unknown substance and arbitrary thickness distribution. As a result, since the absorption recorded in the FTIR is based on the calculation of light incident on the device area, the light intensity recorded here can be a combination of arbitrary light diffraction, with a possible weak trend of its designed filtering capability. The combination of arbitrary light diffractions at different wavelengths can also add up to a non-zero sideband absorption intensity. However, for the quantum efficiency measurement below 1.8 μm, the light source is a collimated light beam, which has a light spot with diameter of approximately 20 μm. In addition to a much thinner etch product residue layer and clearer DBR surface, the light spot can be easily moved to a clean area on the top surface of the device for QE measurement. By doing this, the adverse effect of the etch product can be eliminated.

To prove this hypothesis, RSoft simulations were used to calculate the light diffraction under different conditions 1) an etch product of 200 nm (Figure 6.6 (a)), 2) an etch product of 800 nm (Figure 6.6 (a)), 3) a damaged top DBR (Figure 6.6 (b)), and 4) a damaged resonant cavity (Figure 6.6 (b)), shown in Figure 6.6, where PR200 and PR800 represent the light diffraction spectrum of the integrated photodetectors having photoresist AZ 4620 (n=1.61) on

top with thickness of 200 nm and 800 nm, respectively; DBR-D represents the integrated photodetectors with the top DBR pair damaged (removed), and QE-C stands for the integrated photodetectors with the top three quarter-wave layer damaged (removed). The resonant cavity has a length of 1 μm. In both figures, the fitting results, based on the reference transmission, are provided for comparison. The results shown are approximate because the refractive index of the etch product is unknown, and the residue is a mixture of this substance and AZ 4620.

(a)   (b)
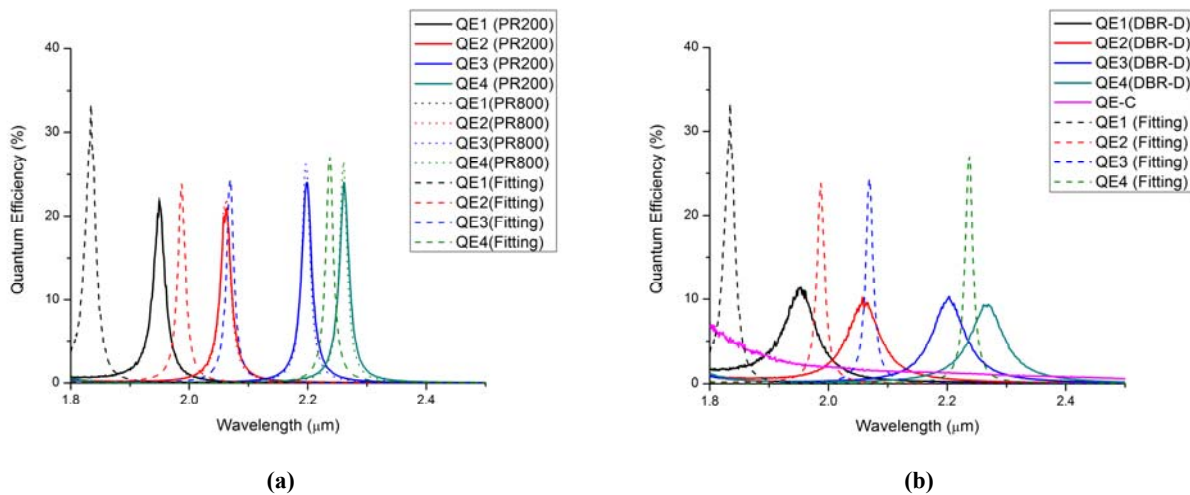
Fig. 6. 6 Light diffraction simulations for (a): 1) an etch product of 200 nm (PR200), 2) an etch product of 800 nm (PR800), and (b): 3) a damaged top DBR (DBR), and 4) a damaged resonant cavity (QE-C) compared with simulated light diffraction without any damage or etch product, parameters taken from Table 5.4.

From the figures shown above, it is reasonable to assume the combination of all the possible diffractions can lead to a random diffraction pattern that is significantly different from the design. The results indicate difficult implementation for longer wavelength detection using Fabry-Perot filters due to the many complications caused by the thick filter stacks. However, this also gives me the motivation to improve the fabrication process or look for better tuning methods for longer wavelengths.

6.2.3 Summary

For wavelength detection beyond 1.8 μm, the DBR coating has three pairs of 360 nm(SiO$_2$)/150 nm(a-Si) and the cavity lengths are 1340 nm, 1450 nm, 1580 nm, and 1640 nm for reference sample transmission at 1.94 μm, 2.06 μm, 2.19 μm, and 2.25 μm. Unlike multispectral wavelength detection below 1.8 μm, the fabrication and photoresponse characterization process of the multispectral wavelength detection beyond 1.8 μm involves complications that are directly associated with much thicker Fabry-Perot filter stacks, and therefore the wavelength peaks obtained in between of 2 μm and 2.5 μm using FTIR show ambiguous trends and non-zero sideband absorption. The explanation for this is most likely to be the arbitrary light diffraction caused by the etch product residue left on the surface that results from the chemical reaction between photoresist and SF$_6$/CF$_4$ gases.

6.3 Future Work

The integrated Fabry-Perot filters discussed in the dissertation show very encouraging results for multispectral wavelength detection at shorter wavelength. In fact, Emadi, *et al*. have suggested using this structure for UV (ultra-violet) and visible light filtering, which requires thinner DBR pairs and thinner resonant cavities than for NIR light filtering. In view of Emadi and the characterization results from this dissertation, it is reasonable to conclude that this method is a promising approach for post-growth wavelength tuning at shorter wavelengths. However, for wavelength tuning at longer wavelengths, filtering methods with simpler fabrication process should be considered for higher yield and more practical characterization.

6.3.1.   Improvements on the current design and fabrication

a) Filter thickness reduction

It has been observed that as the thickness of the filters increase, it becomes much more difficult to remove the etch product. It has also been shown experimentally that a DBR mirror consists of 3 dielectric pairs can provide close to 100% (Figure 2.2) reflection away from the peak. To ensure the performance with minimum required coating layers, the 8-layer structure used in this dissertation will still be used.

One possible way to reduce the total coating thicknesses without changing the filter structure, is to reduce the total DBR quarter-wave layer thicknesses. As mentioned before, the thickness of a quarter-wave layer is calculated as $d = \frac{\lambda_0}{4n}$, where λ_0 is the center wavelength of the stopband, and n is the refractive index of the layer material. In this dissertation, n(a-Si)≈3.58 and n(SiO$_2$)≈1.38, leading to comparatively thin a-Si layers (110 nm and 150 nm for wavelength detection below and beyond 1.8 μm, respectively), and thicker SiO$_2$ layers (260 nm and 360 nm for wavelength detection below and beyond 1.8 μm, respectively). The SiO$_2$ cavity layers are up to around 600 nm and 1600 nm for each case. It should be noticed that the total thickness of the cavity and the low-n DBR layers account for most of the filter thickness: 73.4% - 76.2% and 80.2% - 82.0% according to the design for both cases, respectively, and thickness reduction of the layers will effectively reduce the total thickness of the filters.

Therefore, materials with a slightly higher refractive index can be considered for the low-n material to reduce the cavity thickness and the low-n quarter-wave layer thicknesses. Common amorphous dielectric materials such as TiO$_2$, having a refractive index of approximately 2.38 beyond 1500 nm [104], or Si$_3$N$_4$, having a refractive index of approximately 1.98 beyond 1200 nm [105], can be considered as a substitute for SiO$_2$. The extinction coefficients (k) for bot

materials approach 0 beyond 800 nm, making the film transparent in the regimes of interest. For example, a 209 nm TiO_2 layer can replace a SiO_2 layer of 360 nm, and the cavity length can be reduced to 820 nm to 1030 nm for the four wavelengths beyond 1.8 μm in this dissertation. For the filter with an original cavity thickness of 1450 nm, using TiO_2 layer can reduce the total thickness by 573 nm. This example is illustrated in Table 6.2. Similar principles can be applied to other wavelengths. The high-n quarter-wave layers in the example are still a-Si with a thickness of 150 nm, 4 DBR pairs, and total thickness of 600 nm. In addition, the temperature dependence of the refractive index of TiO_2 and Si_3N_4 are considerably weak from 100K to 500K [106], [107], suggesting the positions of the transmission peaks are relative insensitive to operating temperature change.
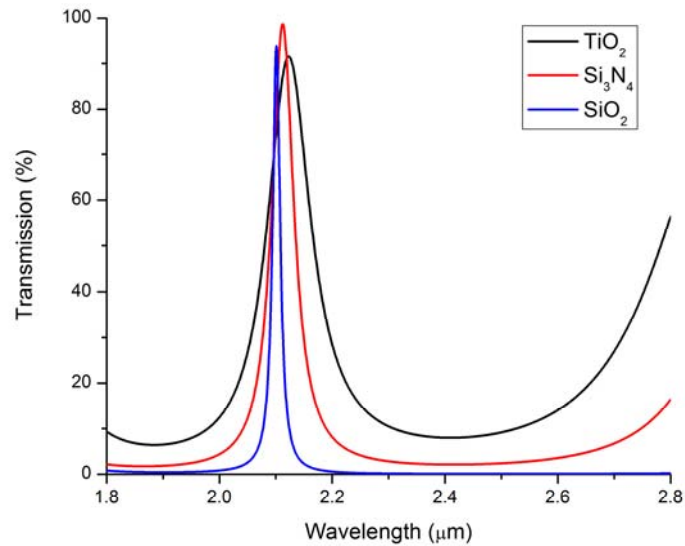
Fig. 6. 7 A comparison of transmission peaks using TiO₂, Si₃N₄, and SiO₂ as the lower-index material in the Fabry-Perot filters

Table 6. 2 A comparison of the thicknesses of the lower-index quarter-wave layer by using different materials and the corresponding total filter thicknesses.

Thicknesses (nm)	TiO$_2$	Si$_3$N$_4$	SiO$_2$
Quarter-wave Layer Thickness (nm) × Repetition Times	209 × 3	252 × 3	360 × 3
Cavity Thickness (nm)	900	1070	1450
Total Filter Thickness (nm)	2127	2426	3130

It can be seen that the total filter thickness can be greatly reduced (32.0% for using TiO$_2$ and 18.6 % for using Si$_3$N$_4$ in the given example) by replacing SiO$_2$ with another amorphous material having a higher refractive index. This provides a promising way to reduce the usage of a thick photoresist etch mask for filter coating etching, and thus provide a clearer surface for the FTIR measurements.

It should also be noted that since Δn=n(high)-n(low) decreases, the bandwidth of stopband and the sideband reflectivity decreases, and the peak gets wider, as illustrated in eq.(2.2.1) and eq.(2.2.2) and shown in Figure 6.2. This means that there is a trade-off between n(low) and the peak width. Also, the refractive index of the dielectric materials mentioned above (TiO$_2$ and Si$_3$N$_4$) varies when different deposition methods are used for the material growth, and a calibration of the material property should be performed prior to the filter integration. Additionally, reactive gases, e.g. O$_2$ or N$_2$ in this case [66], [97], might be used together with the Si or Ti target.

b) Dark current reduction

Since a goal of this dissertation is to detect wavelengths at room temperature, it is very critical to maintain the dark current of the integrated devices low. For the current photodetectors with InGaAs/GaAsSb active region, the typical dark current at 5 V reverse bias is 10^{-5} V for a device with diameter of 500 μm. This results high noise during photocurrent measurement by FTIR, which results operation to low voltage (-0.2 V in this case). This can cause the

photocurrent collection efficiency to be <100%, and thus lower quantum efficiency than expected. In other words, to allow all the carriers generated to be collected, higher operating voltage should be applied on the devices.

From our previous studies, the dark current under low voltage is mainly from sidewall leakage, and therefore a shallow mesa structure is suggested to minimize the sidewall damage caused during the mesa etch, sputtering process, and filter etch processes, as shown in Figure 6.8. It can be seen that only the undoped InP (wider bandgap) undergoes the mesa etch and the narrow bandgap active region is buried intact.
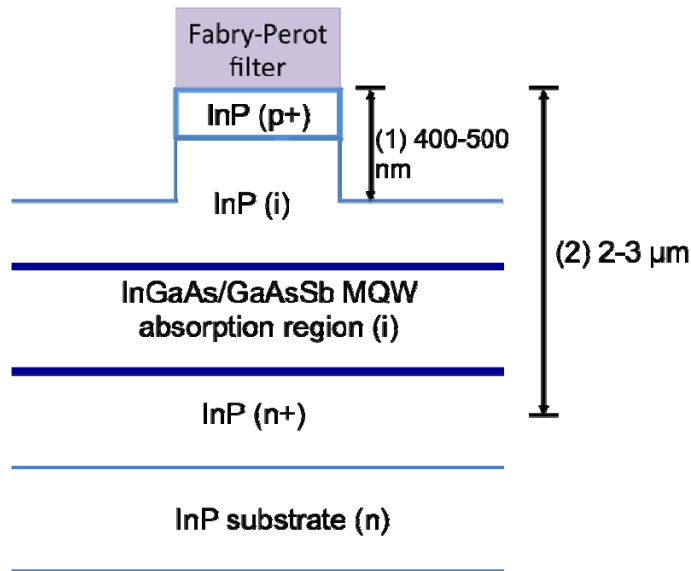
Fig. 6. 8 Schematic of a shallow mesa structure with a mesa height of (1) approximately 400-500 nm, compared with current mesa height of 2-3 μm.

By using the shallow mesa structure , the dark current can be effectively suppressed in order to allow all the carriers generated to be collected at a higher reverse bias [108], [109].

c) Cavity etch and detection of more wavelengths

The ability to fabricate integrated devices that can detect more wavelengths simultaneously can be realized by using the "reflow" feature of photoresist, which has been discussed thoroughly in some publications [65]. In this method, photoresist (cavity etch mask) is patterned as stripes with a pre-determined gap/distance between each stripe, while the dimension of the gap and stripes can vary along the direction perpendicular to the stripes for photoresist on different cavities (step 1)). The pattern is treated to reflow and form a "ball" like shape that eventually fills in the gap and forms a uniform layer of photoresist [66], [110], [111]. By adjusting the dimension of the gap, different thicknesses of photoresist layers can be formed after the reflow process by only one photolithography step. In other words, masks with different thicknesses can be formed on different cavities using one photolithography step (step 2)). This enables different dry etch depth in to the SiO_2 in a single step (step 3)). This can greatly accelerate the fabrication process for making integrated devices capable of detecting many wavelengths simultaneously. However, for this method, the pattern dimensions, treatment recipe, and etching profile need to be carefully calculated and calibrated. A demonstration of the process is shown in Figure 6.9, and a much more thorough study can be found in Emadi *et al.*'s publications [65], [66].

Step 1) Photoresist patterning

Step 2) After photoresist reflow and post bake

Step 3) During/After dry etch
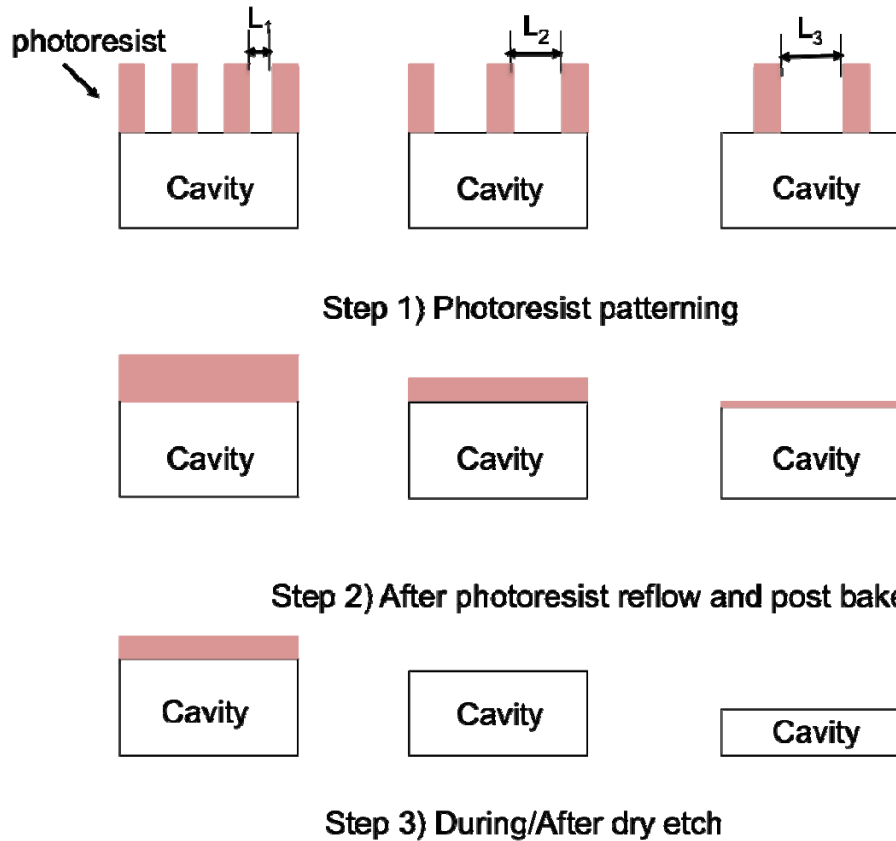
Fig. 6. 9 A demonstration of the reflow process for making photoresist etch mask with different thicknesses in one photolithography step and obtaining different etch depths in one step.

6.3.2. Other filtering approaches

The guided-mode resonance grating filters (Chapter 4) are revisited here for their potential in multispectral wavelength detection in the longer SWIR regime. Compared to Fabry-Perot filters, the grating filters have much simpler structures and fewer layers, and also the feature size increases in accordance with the wavelength to be filtered, which makes it possible to fabricate using standard photolithography for longer wavelength detection. Although this method has higher sideband transmission and wider peaks compared to the Fabry-Perot cavities, it has high transmission and is able to provide a clear surface for photoresponse measurement in

an FTIR. Figure 6.10 is an RSoft simulation example of the transmission characteristics of guided-mode resonance grating filters to realize wavelength detection at 2.35 μm and 2.49 μm, with period Λ=1.62 μm, fill factor FF=0.67, and period Λ=1.63 μm, fill factor FF=0.73, respectively. It can be seen that the transmission characteristics have the ability to distinguish one peak wavelength from another, given adequate photodetector light absorption in this regime. This said, a different absorption region should also be considered for higher light absorption and better filtering. However, it should be noted that the transmission wavelengths are susceptible to light incident angle change and operation temperature variation according to previous sensitivity analysis, limiting this filtering method to applications with constant light incident angle and stable operation temperature.
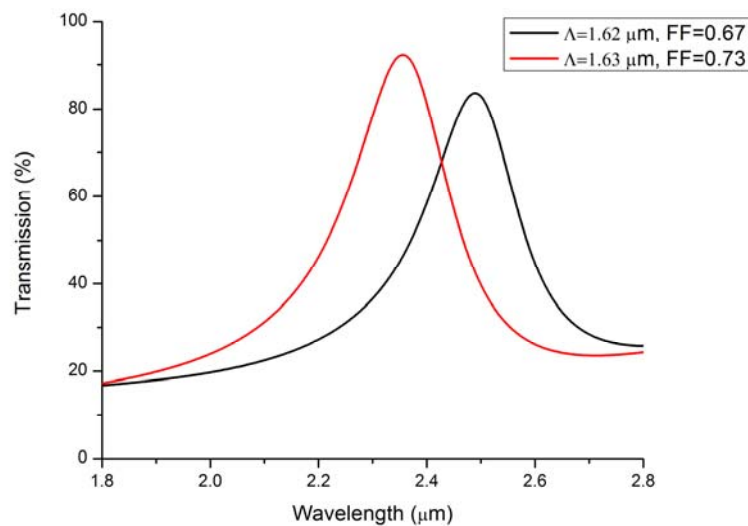
Fig. 6. 10 Simulated transmission of guided-mode resonance grating filtering wavelength at 2.35 μm (Λ=1.62 μm, FF=0.67) and 2.49 μm (Λ=1.63 μm, FF=0.73)

References

[1]   R. Shogenji, Y. Kitamura, K. Yamada, S. Miyatake, and J. Tanida, "Multispectral imaging using compact compound optics.," *Opt. Express*, vol. 12, no. 8, pp. 1643–55, Apr. 2004.

[2]   P. Vines, C. H. Tan, J. P. R. David, R. S. Attaluri, T. E. Vandervelde, S. Krishna, W. Y. Jang, and M. M. Hayat, "Low strain multiple stack quantum dot infrared photodetectors for multispectral and high resolution hyperspectral imaging," *2009 IEEE LEOS Annu. Meet. Conf. Proc.*, pp. 166–167, Oct. 2009.

[3]   M. E. Dickinson, G. Bearman, and S. Tille, "Multi-spectral imaging and linear unmixing add a whole new dimension to laser scanning fluorescence microscopy," *Biotechniques*, vol. 31, no. 6, 2001.

[4]   F. Wikipedia, "Multispectral image Hyperspectral imaging," no. 50 m.

[5]   N. Gat, "Imaging spectroscopy using tunable filters: a review," *AeroSense 2000*, pp. 50–64, 2000.

[6]   P. W. Kruse and D. D. Skatrud, *Uncooled Infrared Imaging Arrays and Systems*. Academic Press (October 22, 1997), 1997, pp. 1–11.

[7]   N. A. Diakides and J. D. Bronzino, *Medical Infrared Imaging*, 1st ed. Boca Raton, FL: CRC Press, 2007, pp. 1–5.

[8]   A. Rogalski, *Infrared Detectors*, 2nd ed. Boca Raton, FL: CRC Press, 2011, pp. 807–808.

[9]   a. Rogalski, "Recent progress in infrared detector technologies," *Infrared Phys. Technol.*, vol. 54, no. 3, pp. 136–154, May 2011.

[10]   R. Bhargava and I. W. Levin, *Spectrochemical Analysis Using Infrared Multichannel Detectors*, 1st ed. Wiley-Blackwell, 2005, pp. 283–297.

[11]   I. Gatley, D. L. DePoy, and A. M. Fowler, "Astronomical Imaging with Infrared Array Detectors," *Science (80-.).*, vol. 242, no. 4883, pp. pp. 1264–1270, 1988.

[12] S. Zhang, D. Dong, W. Zheng, and J. Wang, "Optical methods for monitoring harmful gas in animal facilities," *Opt. Eng.*, vol. 53, no. 6, p. 061602, 2014.

[13] J. Yuan, B. Chen, and A. L. Holmes, "Near-infrared quantum efficiency of uncooled photodetectors based on InGaAs / GaAsSb quantum wells lattice-matched to InP," *Electron. Lett.*, vol. 47, no. 20, pp. 3–4, 2011.

[14] B. Chen, W. Jiang, J. Yuan, A. L. Holmes, and B. M. Onat, "SWIR/MWIR InP-Based p-i-n Photodiodes With InGaAs/GaAsSb Type-II Quantum Wells," *IEEE Journal of Quantum Electronics*, vol. 47, no. 9. pp. 1244–1250, Sep-2011.

[15] Wikipedia, "Infrared spectroscopy --- Wikipedia{,} The Free Encyclopedia." 2014.

[16] F. Wikipedia, "Imaging spectroscopy."

[17] A. Rao and J. P. Buijtenen, "Infrared Signature Modeling of Aircraft Exhaust Plume Faculty of Aerospace Engineering."

[18] S. Baqar, "6 DEVELOPMENT OF AN IR SIGNATURE MODEL," 2008.

[19] L. Zheng, M. Z. Tidrow, A. Novello, H. Weichel, and S. Vohra, "Type II Strained Layer Superlattice : A Potential Infrared Sensor Material for Space," no. 703.

[20] D. Wu, H. Yang, X. Chen, Y. He, and X. Li, "Application of image texture for the sorting of tea categories using multi-spectral imaging technique and support vector machine," *J. Food Eng.*, vol. 88, no. 4, pp. 474–483, Oct. 2008.

[21] H. Teichert, T. Fernholz, and V. Ebert, "Simultaneous in situ measurement of CO, H2O, and gas temperatures in a full-sized coal-fired power plant by near-infrared diode lasers.," *Appl. Opt.*, vol. 42, no. 12, pp. 2043–51, Apr. 2003.

[22] M. Gabrysch, C. Corsi, F. S. Pavone, and M. Inguscio, "Simultaneous detection of CO and CO2 using a semiconductor DFB diode laser at 1.578 µm," *Appl. Phys. B*, vol. 65, no. 1, pp. 75–79, 1997.

[23] T. Cai, G. Gao, W. Chen, G. Liu, and X. Gao, "Simultaneous Measurements of CO2 and CO Using a Single Distributed-Feedback (DFB) Diode Laser Near 1.57 μm at Elevated Temperatures," *Appl. Spectrosc.*, vol. 65, no. 1, pp. 108–112, Jan. 2011.

[24] "Fundamentals of IR and RF Remote Control." [Online]. Available: http://davehouston.org/ir-rf_fundamentals.htm.

[25] "The Power of Hyperspectral Imaging - Resonon's off-the-shelf Pika IIi." [Online]. Available: http://www.ptgrey.com/news/pressreleases/details.asp?articleID=639.

[26] L. Jing, *Spectral Distortion Analysis in Image Fusion Algorithms for Remote Sensing and Development of Fusion Methods*. York University (Canada), 2008.

[27] V. Petrovid, "Objective image fusion performance measure," vol. 36, no. 4, pp. 308–309, 2000.

[28] K. Makoto, M. Koudai, and I. G. A. Mistuhiro, "High-speed in-line use Spectrometer using the highly integrated original array sensor," vol. 47, no. 47, pp. 49–52, 2009.

[29] HAMAMATSU, "Characteristics and use of infrared detectors," 2011.

[30] D. F. J. Vallese, "Cooled IR Detectors For Remote Sensing And Hyperstactral Imaging," *Photonics Spectra*, 2010.

[31] Dalsa Teleyne, "No Title." [Online]. Available: https://www.teledynedalsa.com/imaging/markets/aerospace/multispectral/.

[32] G. Ariyawansa, Y. Aytac, a. G. U. Perera, S. G. Matsik, M. Buchanan, Z. R. Wasilewski, and H. C. Liu, "Five-band bias-selectable integrated quantum well detector in an n-p-n architecture," *Appl. Phys. Lett.*, vol. 97, no. 23, p. 231102, 2010.

[33] A. Perera and Y. Aytac, "Photo detectors for multi-spectral sensing," *... (IEEE-NANO), 2011 ...*, 2011.

[34] "Absorption by atmospheric gases in the IR , visible and UV spectral," pp. 1–10, 2009.

[35] Wikipedia, "Optical filter --- Wikipedia{,} The Free Encyclopedia." 2014.

[36] V. Lehmann, R. Stengl, H. Reisinger, R. Detemple, and W. Theiss, "Optical shortpass filters based on macroporous silicon," *Appl. Phys. Lett.*, vol. 78, no. 5, p. 589, 2001.

[37] K. Kishino, "Resonant cavity-enhanced (RCE) photodetectors," *IEEE Journal of Quantum Electronics*, vol. 27, no. 8. pp. 2025–2034, 1991.

[38] K. Lai and J. C. Campbell, "Design of a tunable GaAs/AlGaAs multiple-quantum-well resonant-cavity photodetector," *IEEE Journal of Quantum Electronics*, vol. 30, no. 1. pp. 108–114, 1994.

[39] R. Sidhu, H. Chen, N. Duan, G. V Karve, J. C. Campbell, and A. L. Holmes, "GaAsSb resonant-cavity enhanced avalanche photodiode operating at 1 . 06 lm," vol. 40, no. 20, pp. 65–66, 2004.

[40] K.-W. Lai, Y.-S. Lee, Y.-J. Fu, and S.-D. Lin, "Selecting detection wavelength of resonant cavity-enhanced photodetectors by guided-mode resonance reflectors.," *Opt. Express*, vol. 20, no. 4, pp. 3572–9, Feb. 2012.

[41] C. C. Chen, H. C. Chen, C. H. Kuan, S. D. Lin, and C. P. Lee, "Multicolor infrared detection realized with two distinct superlattices separated by a blocking barrier Multicolor infrared detection realized with two distinct superlattices separated by a blocking barrier," vol. 80, no. May, pp. 2251–2253, 2002.

[42] N. Gautam, M. Naydenkov, S. Myers, a. V. Barve, E. Plis, T. Rotter, L. R. Dawson, and S. Krishna, "Three color infrared detector using InAs/GaSb superlattices with unipolar barriers," *Appl. Phys. Lett.*, vol. 98, no. 12, p. 121106, 2011.

[43] J. Frigerio, S. Bietti, and G. Isella, "Multispectral imaging sensors integrated on silicon," *SPIE Newsroom*, pp. 2–4, 2013.

[44] H. C. Liu, J. Li, J. R. Thompson, Z. R. Wasilewski, M. Buchanan, and J. G. Simmons, "Multicolor Voltage-Tunable Quantum-Well," vol. 14, no. 12, pp. 566–568, 1993.

[45] M.Z.Tidrow, K. K. Choi, P. W. Cooke, and F. Monmouth, "Multicolor Quantum Well Infrared Photodetectors," pp. 26–27.

[46] J. Vaillancourt, P. Vasinajindakaw, X. Lu, A. Stintz, J. Bundas, R. Cook, D. Burrows, K. Patnaude, R. Dennis, A. Reisinger, and M. Sundaram, "A voltage-tunable multispectral 320 × 256 InAs/GaAs quantum-dot infrared focal plane array," *Semicond. Sci. Technol.*, vol. 24, no. 4, p. 045008, Apr. 2009.

[47] S. S. Murtaza, I.-H. Tan, E. Bowers, E. L. Hu, K. A. Anselm, M. R. Islam, R. V Chelakara, R. D. Dupuis, B. G. Streetman, and J. C. Campbell, "High-Finesse Resonant-Cavity Photodetectors with an Adjustable Resonance Frequency," vol. 14, no. 6, pp. 1081–1089, 1996.

[48] E. Özbay, I. Kimukin, N. Biyikli, O. Aytür, M. Gökkavas, G. Ulu, M. S. Ünlü, R. P. Mirin, K. a. Bertness, and D. H. Christensen, "High-speed >90% quantum-efficiency p–i–n photodiodes with a resonance wavelength adjustable in the 795–835 nm range," *Appl. Phys. Lett.*, vol. 74, no. 8, p. 1072, 1999.

[49] Y. Shi, S. Member, J. H. Zhao, and S. Member, "Tunable Photodetectors Based on Strain Compensated GaInAsSb / AlGaAsSb Multiple Quantum Wells Grown by Molecular Beam Epitaxy," vol. 44, no. 12, pp. 2167–2173, 1997.

[50] R. Mao, Y. Zuo, and C. Li, "Demonstration of low-cost Si-based tunable long-wavelength resonant-cavity-enhanced photodetectors," *Appl. Phys. …*, 2005.

[51] S. Foland, K.-H. Choi, and J.-B. Lee, "Pressure-tunable guided-mode resonance sensor for single-wavelength characterization," *Opt. Lett.*, vol. 35, no. 23, pp. 3871–3873, Dec. 2010.

[52] D. McIntosh, Q. Zhou, F. J. Lara, J. Landers, and J. C. Campbell, "Flip-Chip Bonded GaP Photodiodes for Detection of 400- to 480-nm Fluorescence," *IEEE Photonics Technology Letters*, vol. 23, no. 13. pp. 878–880, Jul-2011.

[53] L. Martín-Moreno, F. J. García-Vidal, H. J. Lezec, K. M. Pellerin, T. Thio, J. B. Pendry, and T. W. Ebbesen, "Theory of extraordinary optical transmission through subwavelength hole arrays.," *Phys. Rev. Lett.*, vol. 86, no. 6, pp. 1114–7, Feb. 2001.

[54] Y.-T. Yoon, H.-S. Lee, S.-S. Lee, S. H. Kim, J.-D. Park, and K.-D. Lee, "Color filter incorporating a subwavelength patterned grating in poly silicon.," *Opt. Express*, vol. 16, no. 4, pp. 2374–80, Feb. 2008.

[55] B. Zandi, D. Vasileska, and P. Wijewarnasuriya, "Modeling Mercury Cadmium Telluride (HgCdTe) Photodiodes," no. November, 2009.

[56] B. Chen, W. Y. Jiang, J. Yuan, A. L. Holmes, and B. M. Onat, "Demonstration of a Room-Temperature InP-Based Photodetector Operating Beyond 3 m," *IEEE Photonics Technol. Lett.*, vol. 23, no. 4, pp. 218–220, 2011.

[57] O. Bubulac, A. M. Andrews, E. R. Gertner, and D. T. Cheung, "Backside-illuminated InAsSb/GaSb broadband detectors," vol. 91360, no. October 1979, pp. 90734–90736, 1980.

[58] J. C. Dries, M. R. Gokhale, K. J. Thomson, S. R. Forrest, and R. Hull, "Strain compensated In 1-x Ga x As, x < 0.47 … quantum well photodiodes for extended wavelength operation," vol. 73, no. 16, pp. 2263–2265, 1998.

[59] J. F. Damlencourt, J. L. Leclercq, M. Gendry, P. Regreny, and G. Hollinger, "High-quality fully relaxed In 0 . 65 Ga 0 . 35 As layers grown on InP using the paramorphic approach," vol. 75, no. 23, pp. 3638–3640, 1999.

[60] R. U. Martinelli, T. J. Zamerowski, and P. a. Longeway, "2.6 µm InGaAs photodiodes," *Appl. Phys. Lett.*, vol. 53, no. 11, p. 989, 1988.

[61] R. W. M. Hoogeveen, R. J. Van Der A, and A. P. H. Goede, "Extended wavelength InGaAs infrared (1.0-2.4 micron) detector arrays on SCIAMACHY for space-based spectrometry of the Earth atmosphere," vol. 42, no. 1350, 2001.

[62] R. Sidhu, J. C. Campbell, and a. L. Holmes, "A long-wavelength photodiode on InP using lattice-matched GaInAs-GaAsSb type-II quantum wells," *IEEE Photonics Technology Letters*, vol. 17, no. 12. pp. 2715–2717, Dec-2005.

[63] D. Fay and A. Waxman, "Fusion of multi-sensor imagery for night vision: color visualization, target learning and search," *… , 2000. FUSION …*, 2000.

[64] "Fabry–Pérot interferometer - Wikipedia, the free encyclopedia." [Online]. Available: http://en.wikipedia.org/wiki/Fabry–Pérot_interferometer. [Accessed: 24-Jan-2013].

[65] A. Emadi, "Linear-Variable Optical Filters for Microspectrometer Application," Delft University of Technology.

[66] A. Emadi, H. Wu, G. de Graaf, and R. Wolffenbuttel, "Design and implementation of a sub-nm resolution microspectrometer based on a Linear-Variable Optical Filter.," *Opt. Express*, vol. 20, no. 1, pp. 489–507, Jan. 2012.

[67] A. Emadi, H. Wu, G. De Graaf, and K. Hedsten, "An UV linear variable optical filter-based micro-spectrometer," *Procedia …*, vol. 5, pp. 416–419, Jan. 2010.

[68] a. Emadi, H. Wu, S. Grabarnik, G. De Graaf, K. Hedsten, P. Enoksson, J. H. Correia, and R. F. Wolffenbuttel, "Fabrication and characterization of IC-Compatible Linear Variable Optical Filters with application in a micro-spectrometer," *Sensors and Actuators A: Physical*, vol. 162, no. 2. pp. 400–405, Aug-2010.

[69] "Distributed Bragg reflector - Wikipedia, the free encyclopedia." [Online]. Available: http://en.wikipedia.org/wiki/Distributed_Bragg_reflector. [Accessed: 24-Jan-2013].

[70] S. Wang, C. Zhou, Y. Zhang, and H. Ru, "gratings with high efficiency at a wavelength of 1550 nm," vol. 45, no. 12, pp. 2567–2571, 2006.

[71] Y. Zhou, M. C. Huang, and C. J. Chang-Hasnain, "Tunable VCSEL with ultra-thin high contrast grating for high-speed tuning.," *Opt. Express*, vol. 16, no. 18, pp. 14221–6, Sep. 2008.

[72] Y. Kanamori, M. Shimono, and K. Hane, "Fabrication of Transmission Color Filters Using Silicon Subwavelength Gratings on Quartz Substrates," *IEEE Photonics Technol. Lett.*, vol. 18, no. 20, pp. 2126–2128, Oct. 2006.

[73] a. Sharon, D. Rosenblatt, and a. a. Friesem, "Resonant grating–waveguide structures for visible and near-infrared radiation," *J. Opt. Soc. Am. A*, vol. 14, no. 11, p. 2985, Nov. 1997.

[74] S. S. Wang and R. Magnusson, "Theory and applications of guided-mode resonance filters.," *Appl. Opt.*, vol. 32, no. 14, pp. 2606–13, May 1993.

[75] S. Tibuleac and R. Magnusson, "Narrow-linewidth bandpass filters with diffractive thin-film layers.," *Opt. Lett.*, vol. 26, no. 9, pp. 584–6, May 2001.

[76] R. Magnusson and S. S. Wang, "Transmission bandpass guided-mode resonance filters," *Appl. Opt.*, vol. 34, no. 35, pp. 8106–8109, Dec. 1995.

[77] S. Peng and G. M. Morris, "Resonant scattering from two-dimensional gratings," *J. Opt. Soc. Am. A*, vol. 13, no. 5, p. 993, May 1996.

[78] S. Peng and G. M. Morris, "Experimental demonstration of resonant anomalies in diffraction from two-dimensional gratings.," *Opt. Lett.*, vol. 21, no. 8, pp. 549–51, Apr. 1996.

[79] H. Kikuta, Y. Ohira, H. Kubo, and K. Iwata, "Effective medium theory of two-dimensional subwavelength gratings in the non-quasi-static limit," *J. Opt. Soc. Am. A*, vol. 15, no. 6, p. 1577, 1998.

[80] E. Popov, M. Nevière, S. Enoch, and R. Reinisch, "Theory of light transmission through subwavelength periodic hole arrays," *Phys. Rev. B*, vol. 62, no. 23, pp. 16100–16108, Dec. 2000.

[81] H. L. Bertoni and L. S. Cheo, "Frequency -Selective Reflection and Transmission by a Periodic Dielectric Layer," vol. 31, no. 1, pp. 78–83, 1989.

[82] S. Tibuleac and R. Magnusson, "Reflection and transmission guided-mode resonance filters," *J. Opt. Soc. Am. A*, vol. 14, no. 7, p. 1617, Jul. 1997.

[83] M. Born, E. Wolf, and A. B. Bhatia, *Principles of Optics: Electromagnetic Theory of Propagation, Interference and Diffraction of Light*, 7th ed. Cambridge: Cambridge University Press, 1999.

[84] B. Chen and A. L. Holmes, "InP-based short-wave infrared and midwave infrared photodiodes using a novel type-II strain-compensated quantum well absorption region.," *Opt. Lett.*, vol. 38, no. 15, pp. 2750–3, Aug. 2013.

[85] *Nicolet FT-IR User's Guide.* .

[86] Wikipedia, "Fourier transform infrared spectroscopy --- Wikipedia{,} The Free Encyclopedia." 2014.

[87] R. K. Pathria and P. D. Beale, *Statistical Mechanics*, 3rd ed. Butterworth-Heinemann, 2011.

[88] "Refractive index of SiO2 (Silicon dioxide, Silica, Quartz) [CRYSTALS etc.] - RefractiveIndex.INFO." [Online]. Available: http://refractiveindex.info/?group=CRYSTALS&material=SiO2. [Accessed: 01-Mar-2013].

[89] "Refractive Index of Si, Silicon for Thin Film Thickness Measurement," *Solid State Division*. [Online]. Available: http://www.filmetrics.com/refractive-index-database/Si/Silicon. [Accessed: 01-Mar-2013].

[90] C. F. R. Mateus, S. Member, M. C. Y. Huang, Y. Deng, A. R. Neureuther, and C. J. Chang-hasnain, "Ultrabroadband Mirror Using Low-Index Cladded Subwavelength Grating," vol. 16, no. 2, pp. 518–520, 2004.

[91] J. W. Leem and J. S. Yu, "Broadband and wide-angle distributed Bragg reflectors based on amorphous germanium films by glancing angle deposition," vol. 20, no. 18, pp. 20576–20581, 2012.

[92] J. Matsuoka, N. Kitamura, S. Fujinaga, T. Kitaoka, and H. Yamashita, "Temperature dependence of refractive index of SiO2 glass," *J. Non. Cryst. Solids*, vol. 135, pp. 86–89, 1991.

[93] D. Leviton and B. Frey, "Temperature-dependent absolute refractive index measurements of synthetic fused silica," *Astron. Telesc. …*, 2006.

[94] J. Bergmann, M. Heusinger, G. Andrä, and F. Falk, "Temperature dependent optical properties of amorphous silicon for diode laser crystallization," vol. 20, no. November, pp. 3570–3572, 2012.

[95] M. R. Kutteruf, M. K. Yetzbacher, M. J. DePrenger, K. M. Novak, C. a Miller, T. V. Downes, and A. V Kanaev, "Video rate nine-band multispectral short-wave infrared sensor.," *Appl. Opt.*, vol. 53, no. 13, pp. C45–53, May 2014.

[96]   Wikipedia, "Sputter deposition --- Wikipedia{,} The Free Encyclopedia."
        2014.

[97]   U. of Colorado, "Physics of Thin Films - Sputter Deposition Techniques."
        [Online]. Available:
        http://www.uccs.edu/~tchriste/courses/PHYS549/549lectures/sputtertech.htm
        l.

[98]   W. F. University, "Sputtering."

[99]   "Thin Films Sputtering Systems."

[100] M. Song, W. Yang, S. Kwon, Y. Song, N. Cho, and D. Y. Lee, "Influence of
        Deposition Method on Refractive Index of SiO 2 and TiO 2 Thin Films for
        Anti-reflective Multilayers," vol. 45, no. 9, pp. 10–13, 2008.

[101] D. Philip, "Plasma Etching Outline."

[102] K. P. Larsen, D. H. Petersen, and O. Hansen, "Study of the Roughness in a
        Photoresist Masked, Isotropic, SF[sub 6]-Based ICP Silicon Etch," *J.
        Electrochem. Soc.*, vol. 153, no. 12, p. G1051, 2006.

[103] Clariant, "AZ P4000 Thick Film Photoresist," 2000.

[104] "Refractive Index of TiO2 - Amorphous, Titanium Dioxide." [Online].
        Available: http://www.filmetrics.com/refractive-index-database/TiO2+-
        +Amorphous/Titanium-Dioxide.

[105] "Refractive Index of Si3N4." [Online]. Available:
        http://refractiveindex.info/?shelf=main&book=Si3N4&page=Philipp.

[106] T. Toyoda and M. Yabe, "The temperature dependence of the refractive
        indices of SrTiO3 and TiO2," *J. Phys. D. Appl. Phys.*, vol. 16, pp. 251–255,
        1983.

[107] N. Ravindra and S. Abedrabbo, "Temperature-dependent emissivity of
        silicon-related materials and structures," *IEEE Trans. Semicond. Manuf.*, vol.
        11, no. 1, pp. 30–39, 1998.

[108] E. H. Aifer, J. H. Warner, C. L. Canedy, I. Vurgaftman, E. M. Jackson, J. G.
        Tischler, J. R. Meyer, S. P. Powell, K. Olver, and W. E. Tennant, "Shallow-

Etch Mesa Isolation of Graded-Bandgap "" W "" -Structured Type II Superlattice Photodiodes," vol. 39, no. 7, pp. 1070–1079, 2010.

[109] R. Q. Yang, Z. Tian, Z. Cai, J. F. Klem, M. B. Johnson, and H. C. Liu, "Interband-cascade infrared photodetectors with superlattice absorbers Interband-cascade infrared photodetectors with superlattice absorbers," vol. 054514, no. 2010, 2014.

[110] F. T. O. Neill and J. T. Sheridan, "Photoresist reflow method of microlens production Part I : Background and experiments," vol. 9, no. 9, pp. 391–404, 2002.

[111] T. Knieling and W. Benecke, "Microlens array production in a microtechnological dry etch and reflow process for display applications," vol. 12007, pp. 1–4, 2012.